



Title	Studies on Functions of Nonmuscle Myosin II Isoforms in Actin--Microtubule Crosstalk
Author(s)	佐藤, 勇太
Citation	北海道大学. 博士(理学) 甲第13673号
Issue Date	2019-03-25
DOI	10.14943/doctoral.k13673
Doc URL	<a href="http://hdl.handle.net/2115/77066">http://hdl.handle.net/2115/77066</a>
Type	theses (doctoral)
File Information	Yuta_Sato.pdf



[Instructions for use](#)

---

**Studies on  
Functions of Nonmuscle Myosin II Isoforms  
in Actin–Microtubule Crosstalk**

---

**By  
Yuta SATO**

Dissertation

Graduate School of Chemical Sciences and Engineering,  
Hokkaido University

2019

# Index

<b>Abbreviation List .....</b>	<b>4</b>
<b>Chapter 1. General introduction .....</b>	<b>5</b>
<b>1.1. Functions of cytoskeletons in diverse cellular functions</b>	
<b>1.2. MT dynamics and its regulators</b>	
1.2.1. Intrinsic MT dynamics	
1.2.2. Regulation of MT dynamics by MT binding proteins	
1.2.3. Post-translational modification of MTs	
<b>1.3. Actin dynamics and its regulators</b>	
1.3.1. Intrinsic actin dynamics	
1.3.2. Regulation of actin dynamics	
1.3.2. Regulation of actin cytoskeletal structures	
1.3.4. Common features of myosin II subclasses	
1.3.5. NMII and its isoforms	
<b>1.4. Cytoskeletal crosstalk</b>	
1.4.1. Physiological significance of cytoskeletal crosstalk	
1.4.2. Direct actin–MT crosstalk via physical interaction	
1.4.3. Indirect actin–MT crosstalk via small GTPase-mediated signal transduction	
1.4.4. Indirect actin–MT crosstalk via multi-cytoskeleton binding proteins	
1.4.5. Myosin II as an influencer of MT stability and dynamics	
<b>1.5. Purpose of this study</b>	
1.5.1. Analysis of cytoskeletal organization: surfactant-based fractionation [Chapter 2]	
1.5.2. NMII isoform-dependent regulation of MT growth dynamics [Chapter 3]	

**Chapter 2. Establishment of “SERCYF (semi-retentive cytoskeletal fractionation)–method”, for simultaneous analysis of microtubules and actin cytoskeletons ..... 21**

**2.1. Abstract**

**2.2. Introduction**

**2.3. Results**

2.3.1. Treatment with buffers for existing fractionation methods induces cytoskeletal disruption

2.3.2. PEM-based fractionation buffer does not disrupt cytoskeletons significantly

2.3.3. Addition of low-dose taxol into PEMT-buffer achieves semi-retentive cytoskeletal fractionation

2.3.4. Verification of the usability of SERCYF-method: analysis of effects of MT depolymerization on actin cytoskeletons

**2.4. Discussion**

2.4.1. Possible reasons of cytoskeletal disruption by the use of the existing fractionation methods

2.4.2. Limits of SERCYF-method and future perspectives

**2.5. Conclusion**

**2.6. Experimental procedures**

2.6.1. Cell culture

2.6.2. Antibodies

2.6.3. Cell fractionation by MTS-method

2.6.4. Cell fractionation by TSA-method

2.6.5. Cell fractionation by SERCYF-method

2.6.6. Immunofluorescence microscopy

2.6.7. SDS-PAGE and Immunoblotting

**Chapter 3. Functional analysis of nonmuscle myosin IIA and IIB in the regulation of microtubule dynamics ..... 40**

**3.1. Abstract**

**3.2. Introduction**

**3.3. Results**

- 3.3.1. NMIIA, but not NMIIB, is critical for exertion of cellular contractility in U-2 OS osteosarcoma cells
- 3.3.2. Both NMIIA and NMIIB contribute to suppression of MT growth
- 3.3.3. Both NMIIA and NMIIB are required for maintenance of actin and MT cytoskeletal organization
- 3.3.4. NMIIA and NMIIB differently regulate actin organization and dynamics
- 3.3.5. Fast actin dissociation is one of the cause of accelerated MT growth in NMIIB-depleted cells
- 3.3.6. NMIIA contributes to expression of mDia proteins

**3.4. Discussion**

- 3.4.1. NMIIB-dependent MT regulation
- 3.4.2. NMIIA-dependent MT regulation
- 3.4.3. Underlying mechanisms and biological significance of NMII-MT axis

**3.5. Conclusion**

**3.6. Experimental procedures**

- 3.6.1. Cell culture
- 3.6.2. Antibodies
- 3.6.3. siRNA transfection
- 3.6.4. Plasmid transfection
- 3.6.5. Collagen gel contraction assay
- 3.6.6. Immunofluorescence microscopy
- 3.6.7. Confocal time-lapse imaging of EB1-EGFP
- 3.6.8. Analysis of MT growth dynamics with plusTip Tracker software
- 3.6.9. FRAP analysis of mCherry-actin
- 3.6.10. SDS-PAGE and Immunoblotting
- 3.6.11. Quantification of cytoskeletal organization by SERCYF-method
- 3.6.12. Statistical analysis

**General discussion ..... 73**  
**References ..... 75**  
**Acknowledgement ..... 86**

## **Abbreviation list**

---

EB1: end-binding protein 1  
EGFP: enhanced-green fluorescent protein  
FA: focal adhesion  
FRAP: fluorescence recovery after photobleaching  
MCAK: mitotic centromere-associated kinesin  
MAP: microtubule-associated protein  
MELC: myosin essential light chain  
MRLC: myosin regulatory light chain  
MT: microtubule  
MTOC: microtubule organizing center  
MTS: microtubule-sedimentation  
NMII: nonmuscle myosin II  
NMHC: nonmuscle myosin heavy chain  
PEM: PIPES-EGTA-Magnesium  
PEMT: PIPES-EGTA-Magnesium -Triton X-100  
PEMTT: PIPES-EGTA-Magnesium -taxol-Triton X-100  
ROCK: Rho-associated coiled-coil kinase  
ROI: region of interest  
SERCYF: semi-retentive cytoskeletal fractionation  
SF: stress fiber  
siRNA: small interfering RNA  
TSA: Triton X-100 solubility assay  
+TIP: microtubule plus-end tracking protein

## **Chapter 1.**

### **General introduction**

---

#### **1.1. Functions of cytoskeletons in diverse cellular activities**

All cells possess abundant filamentous networks in their cytoplasm (Fig. 1). These networks are known as cytoskeletons, which are essential for broad cellular activities. As their name suggested, cytoskeletons function as “skeletons”; they provide cells with solidity to protect cells from external forces. This role is important for especially animal cells because they do not possess cell wall. Meanwhile, importantly, cytoskeletons are more dynamic and flexible rather than rigid. Such dynamic behaviors of cytoskeletons are originated from their polymerization/depolymerization cycles. Among three types of eukaryote cytoskeletons, microtubules (MTs) and actin cytoskeletons are highly dynamic networks and have network-wide turnover rates on the order of minutes (Huber et al., 2015). On the other hand, intermediate filaments (IFs) are relatively non-dynamic and have network-wide remodeling rates on the order of hours. In contrast to the main IF role in generating cellular solidity and elasticity, dynamic MTs and actin cytoskeletons play roles in various cellular motilities, including cell migration, cell division, and neuronal development. In this report, I focus on the dynamics of two cytoskeletons, MTs and actin cytoskeletons.

#### **1.2. MT dynamics and its regulators**

##### **1.2.1. Intrinsic MT dynamics**

MTs act as railways for intracellular long-distance transport. This role of MTs contributes to positioning of organelles, such as mitochondria, vesicles, and focal adhesion (FA) components, thereby controlling broad cellular activities (De Forges et al., 2012; Etienne-Manneville, 2013; Kaverina and Straube, 2011). Focusing on the structure, a single MT exhibits a hollow tube structure with a diameter of 25 nm that is composed of 10-16 protofilaments, and each protofilament is a product of head-to-tail polymerization of  $\alpha$ -tubulin/ $\beta$ -tubulin heterodimers (Fig. 2). Of the two ends, the  $\alpha$ -tubulin exposed-end is called minus-end and is connected to MT organizing center (MTOC), where  $\gamma$ -tubulin, a MT nucleating protein, is located. On the other hand, the  $\beta$ -tubulin exposed-end is called plus-end. The most important characteristic of MTs is repeated growth and shrinkage episodes of plus-end, known as “dynamic instability” (Akhmanova and Steinmetz, 2015; Brouhard, 2015). A transition step from growth to shrinkage is called “catastrophe”, while that from shrinkage to growth transition is called “rescue”. These stochastic transitions are important for efficient interaction of MTs with organelles during

interphase and with chromosomes during mitotic phase. MT growth results from continuous addition of GTP-bound tubulin dimers to pre-existing MTs. Each tubulin subunit has one GTP-binding site, and GTP in  $\beta$ -tubulin, but not that in  $\alpha$ -tubulin, can be hydrolyzed. After being incorporated into MTs, tubulin hydrolyzes GTP into GDP by using its GTPase activity. When the supply of tubulin dimers stop, GDP-bound tubulin subunits are exposed, which consequently leads to MT catastrophe because the protofilament consisting of GDP-bound tubulin prefers an outward bent conformation. GDP in soluble  $\beta$ -tubulin after MT depolymerization is exchanged into GTP in cytoplasm, which enables re-incorporation of the tubulin dimer into MTs. As described below, the intermediate of tubulin GTP hydrolysis, GDP-Pi-bound tubulin, is recognized by end-binding protein 1 (EB1), a central member of MT plus-end tracking proteins (+TIPs), which is critical for the regulation of MT dynamics (Nehlig et al., 2017).

### **1.2.2. Regulation of MT dynamics by MT binding proteins**

In cells, MT dynamics is regulated by several types of MT-associated proteins (MAPs). The most characterized MAPs are classical MAPs, which directly bind to MTs and modulate stability of MT structure (Walczak and Shaw, 2010). For example, MAP2 binds to dendritic MTs of nerve cells and stabilizes them by suppressing catastrophe. Also, MAP2 promotes MT–MT interaction through its dimerizing activity, leading to MT bundling and further stabilization. Some MAPs destabilize or sever MTs to increase MT dynamics. Mitotic centromere-associated kinesin (MCAK) is well characterized in its function during mitosis; MCAK promotes depolymerization of centromere (kinetochore)-associated MTs and generates traction force for chromosome separation (Gorbsky, 2004; Helenius et al., 2006). Currently, there is increasing evidence that MCAK functions during interphase as well as mitosis (Braun et al., 2014; D'Angelo et al., 2017). Among MAPs, +TIPs directly regulate MT dynamic instability (Fig. 3) (Akhmanova and Steinmetz, 2010; Galjart, 2010; Kumar and Wittmann, 2012). As their name suggested, +TIPs localize to the tip of MTs. EB1, a central member of +TIPs, functions as a scaffold of other +TIPs such as cytoplasmic linker proteins (CLIPs), CLIP-associated proteins (CLASPs), and adenomatous polyposis coli (APC) (Bearce et al., 2015; Nehlig et al., 2017). As structural characteristics, EB1 has calponin homology (CH) domains on its N-terminal heads for MT binding, coiled-coil for dimerization, and EB homology (EBH) domains and C-terminal acidic tails for interaction with other +TIPs. Because the CH domains recognize GDP-Pi-bound tubulin, EB1 treadmills on the growing MT plus-end (to be more precise, slightly behind the tip). In addition to EB1 function in MT stabilization, other +TIPs recruited by EB1 through the interaction with EBH domains and acidic tails further modulate MT stability and/or dynamics. For example, CLIP-170 promotes rescue events and accelerates MT growth by recruiting polymerization-competent tubulin dimers onto MT plus-end (Arnal et al., 2004; Folker et al., 2005). Depletion of CLIP-170 results in a slowdown of MT growth (Nishimura et al., 2012). In the context of

experimental techniques, fluorescent-tagged EB1, like EB1-enhanced green fluorescent protein (EGFP), have been used as an indicator of growing MT plus-end, which enables observation of MT growth dynamics more easily than direct observation with fluorescent-tagged tubulin (Mimori-Kiyosue et al., 2000; Skube et al., 2010). Importantly, by the use of EB1-EGFP in live imaging, we can analyze MT growth dynamics in whole region of the cell including around MTOC, where MT are quite condensed which prevents observation with EGFP-tubulin. However, as EB1 potentially stabilizes MTs, expression level of exogenous EB1 must be taken care of; excess EB1 expression induces MT bundling (Skube et al., 2010). In this study, I used EB1-EGFP to analyze MT growth dynamics.

### **1.2.3. Post-translational modification of MTs**

Both  $\alpha$ -tubulin and  $\beta$ -tubulin have many post-translational modification sites (Fig. 4) (Janke and Bulinski, 2011; Song and Brady, 2015). In addition to standard modifications such as phosphorylation and acetylation, there are tubulin-specific modifications; polyglycylation, polyglutamylolation, and C-terminal detyrosination. These specific modification sites are concentrated in tubulin acidic tails. Because tubulin tails are exposed to the outside surface of polymerized MTs, these modifications influence interaction with MAPs or motor proteins, leading to changes in MT stability and/or dynamics. Although most of tubulin modifications have been reported to stabilize MTs, the detailed relationships between these modifications and MT dynamics are still unclear.

## **1.3. Actin dynamics and its regulators**

### **1.3.1. Intrinsic actin dynamics**

In cells, actin filaments (F-actin) act as multifunctional players; as railways for intracellular transport, plasmalemmal undercoats, generators/transducers of mechanical force, and so on. These properties are quite important for various cellular functions such as mRNA localization, cell shape determination, cell migration, and cell division (Addi et al., 2018). A single actin filament exhibits double strand structure with a diameter of 5-9 nm. Actin filaments are products of monomeric/globular actin (G-actin) polymerization and each filament has plus (barbed)-end and minus (pointed)-end. These ends exhibit different dynamics from MT ones; whereas actin polymerization preferentially occurs at the barbed-end, depolymerization preferentially occurs at the pointed-end. This phenomenon is called “actin treadmilling” (Carlier and Shekhar, 2017) (Fig. 5A). Each G-actin has one ADP/ATP-binding site, and ATP-bound G-actin is polymerization-competent. After being incorporated into a barbed end of pre-existing F-actin, ATP in the newly polymerized actin is hydrolyzed into ADP, just like as GTP/GDP conversion in MT

polymerization. An older part of F-actin mostly consists of ADP-bound actin and frequently undergoes depolymerization from the pointed-end because of low affinity between ADP-bound subunits. Depolymerized actin monomers become polymerization-competent state again after the exchange of ADP to ATP in the cytoplasm.

### **1.3.2. Regulation of actin dynamics**

In addition to intrinsic actin dynamics, actin polymerization/depolymerization cycles are regulated by several kinds of actin binding proteins in cells (Carrier and Shekhar, 2017; Plastino and Blanchoin, 2019; Skrubber et al., 2018) (Fig. 5B). Here, I briefly describe some important factors; profilin, formins, and actin depolymerization factor (ADF)/cofilin. Profilin is a G-actin binding protein that catalyzes the exchange of ADP in G-actin to ATP, thereby increasing polymerization-competent actin pool. Importantly, the profilin-actin complex has a potential to accelerate actin polymerization through the interaction with barbed-end-associated formin family proteins. Formin homology 2 (FH2) domains of formins processively and efficiently add the profilin-actin complex to the barbed-end of F-actin. After polymerization, profilin is dissociated from the complex and interacts with another G-actin. Formins are quite important for F-actin formation because they also promote actin nucleation, the rate-limiting step of actin polymerization. ADF/cofilin promotes actin turnover by severing and depolymerizing F-actin. Depolymerized actin monomers are recycled. Moreover, F-actin fragments generated by cofilin can act as a new barbed-end, resulting in an increase in the frequency of actin polymerization. Cofilin thus controls both actin polymerization and depolymerization. In this way, cellular actin dynamics is cooperatively and strictly regulated by these proteins.

### **1.3.3. Regulation of actin cytoskeletal structures**

Keys to achieve the diverse functions of actin cytoskeletons are not only their dynamics but also their structural variation, for example, plasmalemmal (cell cortex) meshwork, parallel bundles (filopodia) and orderly thin networks (lamellipodia) at leading edge of migrating cells, and contractile actomyosin bundles (Fig. 6) (Chugh and Paluch, 2018; Rottner and Schaks, 2018). Extracellular and intracellular cues control the reorganization of these actin cytoskeletal structures, in which many kinds of proteins participate. Filamin bridges actin filaments to generate actin meshwork direct under the cell cortex to provide stiffness to the cell (Nakamura et al., 2011; Yamazaki et al., 2002). Filopodia and lamellipodia play important roles in directed cell migration or pathfinding of neuronal growth cones (Lowery and Vactor, 2009). Filopodia are formed by fascin-mediated crosslinking of parallel actin filaments whose barbed-ends are oriented toward the outside of the cell. Actin polymerization from the tips of filopodia, which is facilitated by formins, are sufficient to push plasma membrane toward the front, which can determine the direction of cell migration or growth cone guidance. Lamellipodia are two-dimensional branched

actin networks. This branching is mediated by actin related proteins 2/3 (Arp2/3) complex, which binds to lateral side of F-actin and acts as a new nucleator of F-actin. Similar to filopodia, the directions of barbed-ends are oriented toward the outside of the cell. Actin polymerization at the tips of lamellipodia is the major source of driving force that pushes plasma membrane. Importantly, cofilin is enriched in the region just behind the lamellipodia. This cofilin contributes to the fast actin recycling that makes membrane protrusion more efficient. Actomyosin bundles are formed in all types of nonmuscle cells as well as muscle cells. Central players of actomyosin cytoskeletons are F-actin and type 2 myosin (myosin II). Using the energy provided by ATPase activity, myosin II moves F-actin to generate contractile force in cells (Aguilar-Cuenca et al., 2014; Vicente-Manzanares et al., 2009). This contractile force is required for the maintenance of cell shape, retraction of posterior region during cell migration, and constriction of the contractile ring during cytokinesis. To properly reorganize these actin cytoskeletal structures depending on the situation, cells sense environmental cues via ligand-receptor interaction. These extrinsic signals control the activity of small GTPase proteins including Cdc42, Rac1, and RhoA, which promote filopodium, lamellipodium, and contractile actomyosin bundle formation, respectively (Raftopoulou and Hall, 2004). Additionally, intracellular (intrinsic) signals also control the activity of small GTPase proteins.

#### **1.3.4. Common features of myosin II subclasses**

Myosin II is a member of myosin superfamily and can be further classified into four subclasses: skeletal muscle type, cardiac type, smooth muscle type, and nonmuscle type (Sellers, 2000). As a common structure, a single myosin II molecule consists of six subunits: two myosin heavy chains (MHCs), two myosin essential light chains (MELCs), and two myosin regulatory light chains (MRLCs) (Fig. 7A). Each MHC has a globular head for actin-binding and nucleotide-binding, followed by neck and coiled-coil tail regions. The head of MHC exhibits actin-activated  $Mg^{2+}$ -ATPase activity that converts chemical energy into mechanical force to move actin filaments, contributing to contractile force generation. To interact with F-actin, myosin II molecules self-assemble into multimeric bipolar filaments via tail regions. Among the subclasses, muscle type myosin II molecules form bipolar filaments (side-polar filaments in the case of smooth muscle) at all times, whereas nonmuscle myosin II (NMII) molecules do when required. Filament assembly and disassembly of NMII are spatiotemporally controlled by phosphorylation and dephosphorylation of MRLCs, respectively (Fig. 7B). A disassembled NMII molecule becomes folded 10S conformation to diffuse toward another region of the cell, where it is re-assembled into a bipolar filament after becoming extended 6S conformation through MRLC phosphorylation (Breckenridge et al., 2009; Kiboku et al., 2013). Such a 10S–6S transition of NMII enables flexible response to various signals for actin cytoskeletal reorganization.

### **1.3.5. NMII and its isoforms**

Different from the other specialized myosin II subclasses, NMII is expressed in various cell types including nerve cells, blood cells, endothelial cells, epithelial cells, and fibroblastic cells. NMII isoforms of mammals, NMIIA and NMIIB and NMIIC, exhibit different biochemical properties; dynamics of bipolar filament assembly, ATPase activity, motor activity, and actin binding ability (Aguilar-Cuenca et al., 2014; Heissler and Manstein, 2013; Shutova and Svitkina, 2018; Vicente-Manzanares et al., 2009) (Fig. 7C). These differences further raise distinct subcellular distributions and cellular functions between isoforms. In cultured cells, while NMIIA distributes throughout the cell, NMIIB distributes to limited regions such as posterior and tail region during normal fibroblast migration and perinuclear region during spreading (Hirata et al., 2009; Saitoh et al., 2001). Such different distributions are thought to depend on tail regions of each heavy chain, nonmuscle myosin heavy chain IIA (NMHC-IIA) or NMHC-IIB, suggested from experiments that used tail-exchanged chimeric mutants of NMHC-IIA and NMHC-IIB (Sandquist and Means, 2008; Vicente-Manzanares et al., 2008). During directed cell migration, NMIIA and NMIIB contributes to the retention of cell shape in anterior and posterior regions, respectively (Kuragano et al., 2018a). The loss of each isoform results in appearance of improper protrusions from corresponding regions, which finally misdirects cell migration. With respect to the ability for contractile force generation, the degrees of contribution seem to largely differ between NMIIA and NMIIB; NMIIA mainly contributes to generate contractile force in several cell types (Jorrisch et al., 2013; Shutova et al., 2017; Thomas et al., 2015). Among three isoforms, NMIIA and NMIIB are considered to be especially important for proper individual development, as suggested by studies with genetic-engineered mice. NMIIA deletion induces embryonic lethality due to defects in visceral endoderm and placenta (Conti et al., 2004; Wang et al., 2010). NMIIB deletion induces embryonic lethality or death during the first day after birth due to heart failure (Tullio et al., 1997). On the other hand, NMIIC deletion induces no obvious defects (Ma et al., 2010). These results also imply that NMIIA and NMIIB have isoform-specific functions which cannot be compensated by the other isoform.

## **1.4. Cytoskeletal crosstalk**

### **1.4.1. Physiological significance of cytoskeletal crosstalk**

Despite the fact that three types of cytoskeletons, MTs, actin cytoskeletons, and IFs, are composed of different proteins and regulated by different factors or mechanisms as mentioned above, each cytoskeletal system does not function independently of other cytoskeletons. Rather, they communicate with each other and regulate each other's behaviors including their dynamics and structures (Huber et al., 2015; Rodriguez et al., 2003). This communication is called as

“cytoskeletal crosstalk”, which is essential for complicated cellular processes such as cell migration (Waterman-Storer and Salmon, 1999; Wu et al., 2008), cell division (Hu et al., 2011; Landino and Ohi, 2016), and endothelial permeability (Tian et al., 2014; Tian et al., 2017). Although IFs crosstalk with MTs and actin cytoskeletons, in this thesis I focus on the actin–MT crosstalk. This crosstalk can be roughly classified into two categories: direct crosstalk (physical interaction), and indirect crosstalk (Rodriguez et al., 2003). And the latter can be further classified into two patterns: small GTPase-mediated crosstalk, and multi-cytoskeleton binding protein-mediated crosstalk.

#### **1.4.2. Direct actin–MT crosstalk via physical interaction**

In the case of direct crosstalk, MT and actin cytoskeletons are physically crosslinked by cytoskeletal linker proteins (Fig. 8A). For example, some of plakin family proteins, such as ACF7 and plectin 1c, have multiple cytoskeleton-binding domains that allow to crosslink different cytoskeletal elements (Bouameur et al., 2014). The loss of these crosslinkers raises uncontrollable cytoskeletal dynamics or organization, which further raises severe migration defects (Valencia et al., 2013; Wu et al., 2008). Interestingly, classical MAPs, generally recognized as MT regulators, have been found to bind to actin filaments and crosslink them to MTs (Cabral Fontela et al., 2017; Matsushima et al., 2012; Mohan and John, 2015). The MAP-mediated actin–MT crosslink is considered to be important for nerve cell morphology and functions. These static crosslink by plakins or MAPs (or other crosslinkers) leads to alignment of two cytoskeletal elements, which promotes their cooperative functions for efficient cell motility. In addition to a static crosslink, myosin Va and kinesin motor proteins contribute to a transient crosslink (Huang et al., 1999) (Fig. 8B). Such a motor-motor interaction is suggested to be important for cargo transfer between MT- and actin-based transportation rails (Ali et al., 2007).

#### **1.4.3. Indirect actin–MT crosstalk via small GTPase-mediated signal transduction**

MTs and actin cytoskeletons indirectly regulate each other through a small GTPase-mediated signal transduction. RhoA activates Rho-associated coiled-coil kinase (ROCK) that phosphorylates MRLCs, which in turn promotes contractile stress fiber formation (Fig. 9). RhoA also activates formin mDia that enhances actin nucleation and polymerization. Besides the effect on actin dynamics, active mDia forms a complex with EB1 and APC to stabilize MTs (Wen et al., 2004). Another small GTPase Rac1 also controls both MTs and actin (Fig. 10). Rac1 activates Arp2/3 complex to promote lamellipodial protrusion. In addition, Rac1-activated Pak1 kinase phosphorylates and inhibits Op18/Stathmin, a MT-depolymerizing protein (Wittmann et al., 2003; Wittmann et al., 2004). As a result, MT growth is promoted by Rac1. Most importantly, the activities of RhoA and Rac1 are regulated by cytoskeletons. GEF-H1, a guanine nucleotide exchange factor for RhoA, binds to MTs as an inactive state (Fig. 9). Once upon MTs are

depolymerized, GEF-H1 is released and activated to stimulate RhoA (Birkenfeld et al., 2008; Chang et al., 2008). Similarly, MT polymerization can stimulate Rac1 through APC-stimulated exchange factor (Asef) (Waterman-Storer et al., 1999) (Fig. 10). These feedback loops between small GTPase signaling and cytoskeleton organization regulate complicated cellular processes including cell migration.

#### **1.4.4. Indirect actin–MT crosstalk via multi-cytoskeleton binding proteins**

Similar to the findings of MAP-actin interaction, profilin and formins, generally recognized as actin regulators, have been found to bind and regulate MT structure/stability/dynamics (Fig. 11). Because it has not been long since MT-binding activity of profilin was reported (Nejedla et al., 2016), few features have been described about the mechanism or physiological significances of profilin-MT interaction. However, this interaction is interesting because either downregulation or upregulation of profilin expression accelerates MT growth (Henty-Ridilla et al., 2017; Nejedla et al., 2016). Because the surfaces of profilin for binding to actin or MT are partially overlapped, profilin cannot bind both cytoskeletons simultaneously (Henty-Ridilla et al., 2017). Accordingly, it is suggested that profilin may choose and bind to the one cytoskeleton depending on the situation. Although the precise mechanism has been unclear, MT-binding of profilin appears to involve formins. Importantly, most formins directly or indirectly bind to MTs (Bartolini and Gundersen, 2010; Chesarone et al., 2010; Zuidsherwoude et al., 2018). Among 15 formins (that are classified into 7 groups) expressed in human, I here introduce one of the well-characterized group, mDia family: mDia1, mDia2, and mDia3. Among functional domains of mDia, FH1 and FH2 are the most important domains because mDia constructs that harbor only FH1 and FH2 can stimulate actin nucleation/elongation (Higashida et al., 2004; Higashida et al., 2008), bind to MTs (Bartolini et al., 2008; Daou et al., 2014; Fernández and Miguel, 2018; Thurston et al., 2012), or align actin and MT cytoskeletons (Thurston et al., 2012). By binding to MT lattice, mDia protects MTs from drug- or cold-induced destabilization and slows down their growth/shrinkage (Bartolini et al., 2008; Bartolini et al., 2016). mDia1 is also located on MT plus-end via interaction with EB1 and APC, which promotes  $\alpha$ -tubulin detyrosination to create a cap-like structure that suppresses MT growth/shrinkage (Wen et al., 2004). Importantly, these MT-stabilizing abilities of mDia are independent from their actin activities (nucleation, elongation) (Bartolini et al., 2008; Cheng et al., 2011; Daou et al., 2014). However, it is also reported that perturbation of actin dynamics by drugs alters mDia1 localization from actin to MTs (Bartolini et al., 2012), suggesting that mDia1, and possibly mDia2 and mDia3, respond to changes in actin dynamics to coordinate actin and MT dynamics. Although I just mentioned about profilin and formins here, there could be more proteins that regulate both actin and MT cytoskeletons to coordinate their behaviors.

#### **1.4.5. Myosin II as an influencer of MT stability and dynamics**

NMII is also one of the important mediators of actin–MT crosstalk; myosin II affects MT stability and dynamics. In neurons, NMII inhibition with blebbistatin, a specific inhibitor of myosin II ATPase activity, was reported to promote neurite outgrowth that was associated with MT extension (Kollins et al., 2009; Rösner et al., 2007). Similarly, blebbistatin treatment also promotes MT bundling and stabilization at the posterior region (retraction tail) of migrating fibroblasts to maintain directional migration (Shutova et al., 2008). Such MT stabilization appears to involve hyperacetylation of  $\alpha$ -tubulin, and NMIIA-exerted cellular contractility plays important roles in this crosstalk (Even-Ram et al., 2007; Joo and Yamada, 2014; Joo and Yamada, 2016). In addition to MT stability, MT dynamics also seems to be controlled by cellular contractility. It was reported that endothelial cells cultured on soft substrates retain NMII activity at low level (Fischer et al., 2009), and cells treated with blebbistatin exhibit fast MT growth (Myers et al., 2011). Although little is known about the mechanism, MCAK is likely to be involved in contractility-mediated MT dynamics (D'Angelo et al., 2017). These findings suggest that NMII-exerted cellular contractility is a negative factor for MT growth; however, underlying mechanisms that affect MT dynamics downstream of cellular contractility have not been clarified. Additionally, whether the effect of NMII on MT dynamics completely depends on its ability to exert cellular contractility, or not, is unclear. We should take account of the possibility that there is an alternative mechanism that NMII controls MT dynamics independent of contractile force generation.

### **1.5. Purpose of this study**

In this study, I set a goal to elucidate functions of NMII in MT dynamics regulation. In the second chapter, I describe a novel method for analysis of cytoskeletal organization. And in the third chapter, I describe novel findings about isoform-specific regulation of NMII on MT growth dynamics and its possible underlying mechanisms.

#### **1.5.1. Analysis of cytoskeletal organization: surfactant-based fractionation [Chapter 2]**

Cytoskeletons are dynamically reorganized in response to intracellular- or extracellular signals. Such a dynamic cytoskeletal reorganization is achieved by the presence of unpolymerized pool which can quickly respond to the cues inducing polymerization. To characterize the roles of proteins or drugs on cytoskeletal organization states, cell biologists often quantify them through fractionation; cells are permeabilized with a surfactant-containing buffer and separated into cytoskeletal (polymerized) and cytoplasmic (unpolymerized) fractions, and the ratio of cytoskeletal proteins between these fractions is calculated after biochemical experiments. To investigate the actin–MT crosstalk, we need to use a fractionation method by which we can

analyze organization states of both MTs and actin cytoskeletons simultaneously. However, so far, there was not such a specialized method. In chapter 2, I describe a novel fractionation method for simultaneous quantification of both cytoskeletal organization states that I have established and reported (Sato et al., 2017).

### **1.5.2. NMII isoform-dependent regulation of MT growth dynamics [Chapter 3]**

Previous studies suggest that NMII is involved in MT dynamics regulation; however, several questions still remain to be resolved: (1) Do such MT effects really depend on the activity for cellular contractility exertion? (2) How does NMII regulate MT dynamics? (3) Are there any differences between NMII isoforms in MT dynamics regulation? The goal of this study is to elucidate the molecular mechanism of NMII isoform-dependent MT dynamics regulation by addressing these questions. In chapter 3, I finally propose a possible mechanism.

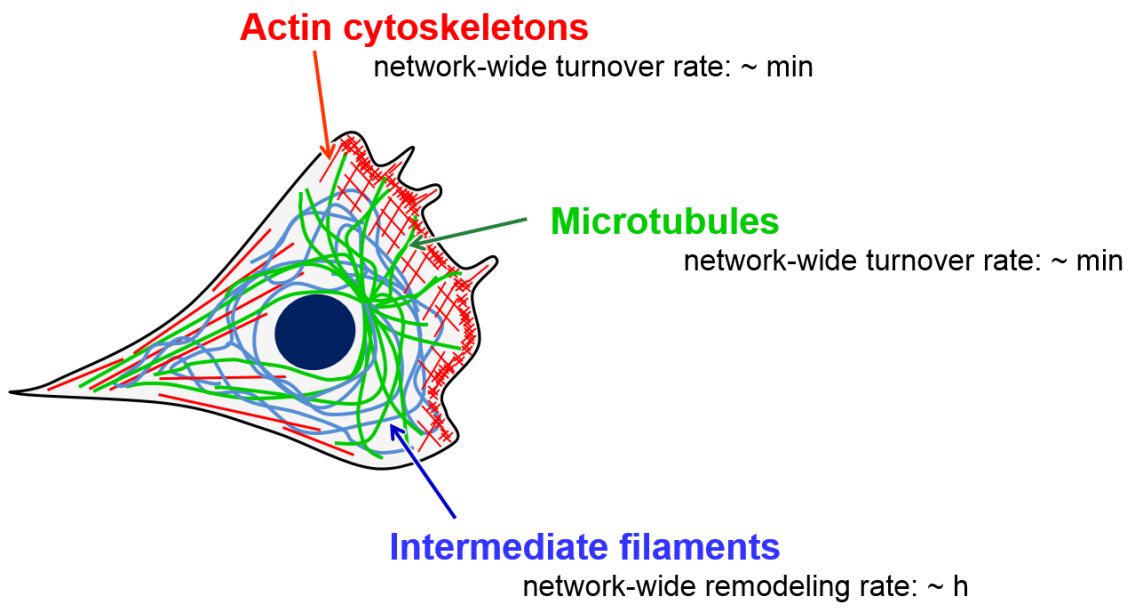


**Fig. 1. Cytoskeletal networks in eukaryote cells.**

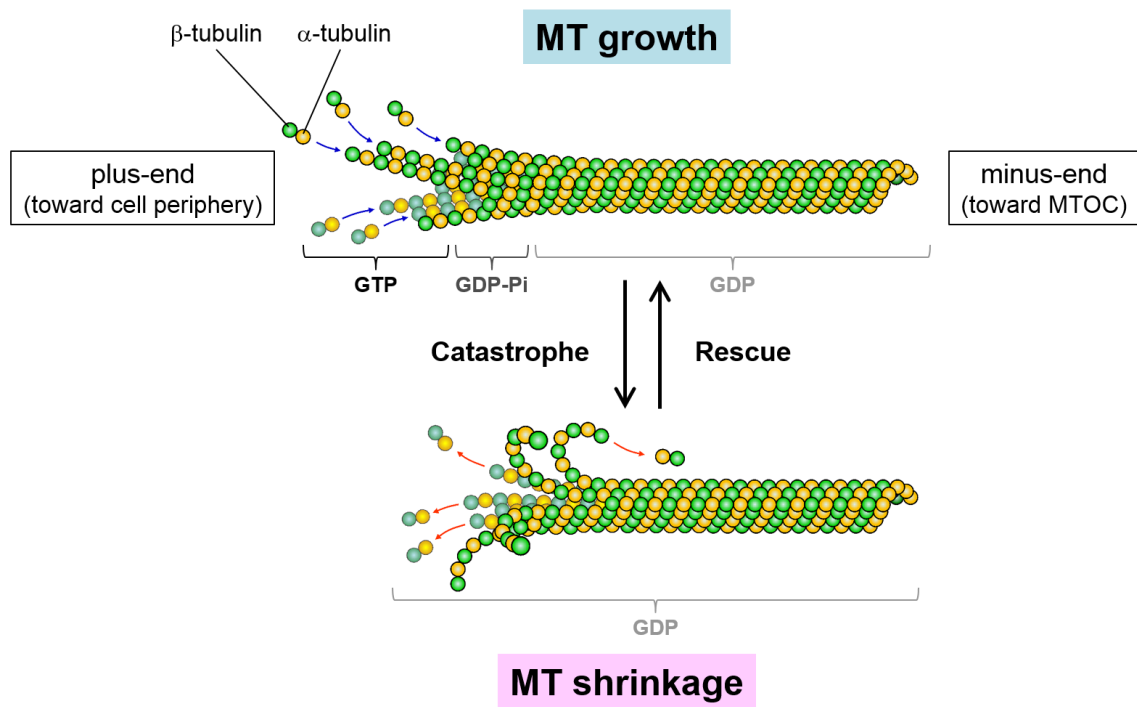


**Fig. 2. Microtubule (MT) structure and intrinsic dynamics.**

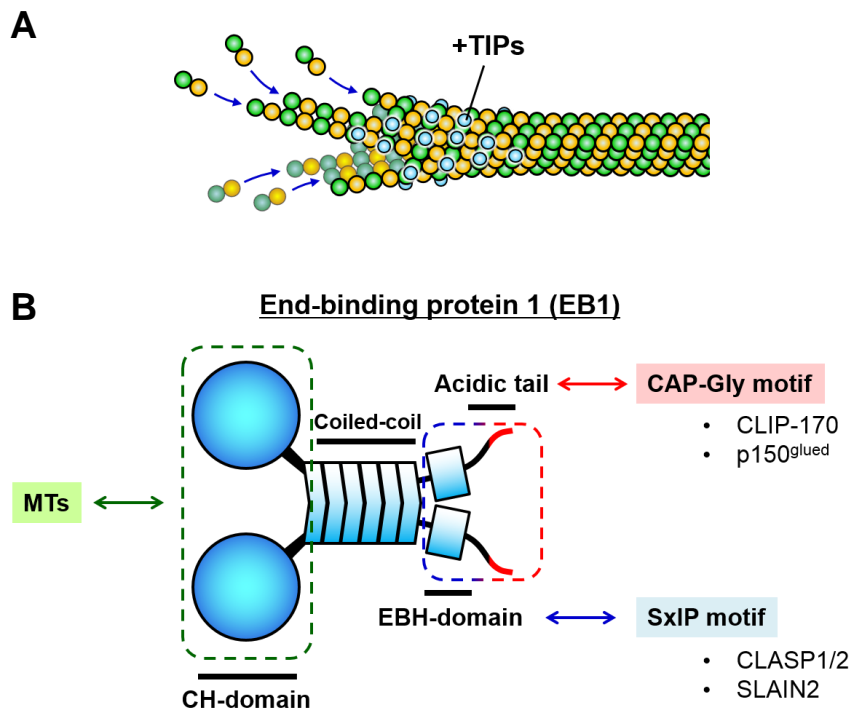


**Fig. 3. End-binding protein 1 (EB1)— a central member of +TIPs.**

(A) Plus-end tracking proteins (+TIPs) on a growing MT plus-end. (B) Structure of EB1.

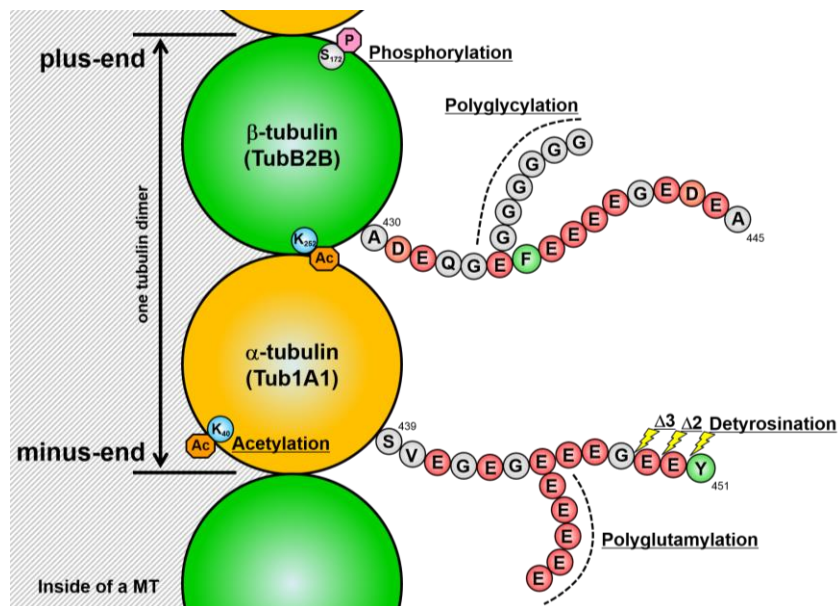


**Fig. 4. Posttranslational modifications of MT.**

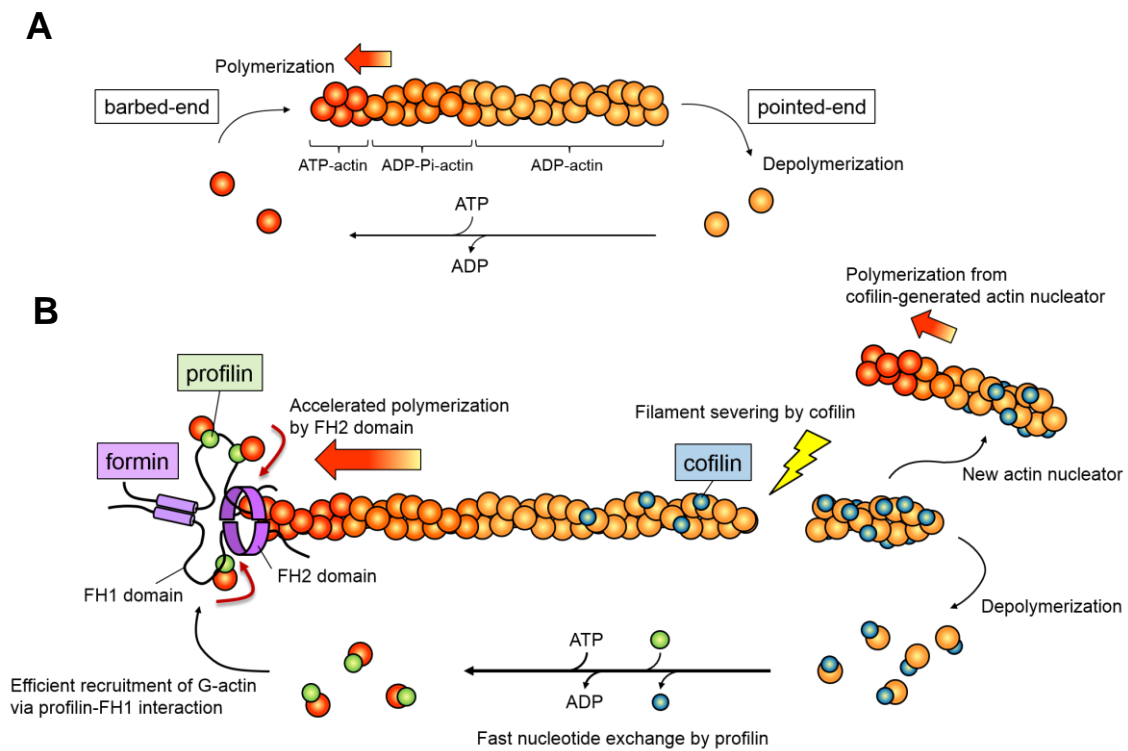


**Fig. 5. Intrinsic and regulated actin dynamics.**

(A) Intrinsic actin dynamics. (B) Regulated actin dynamics.

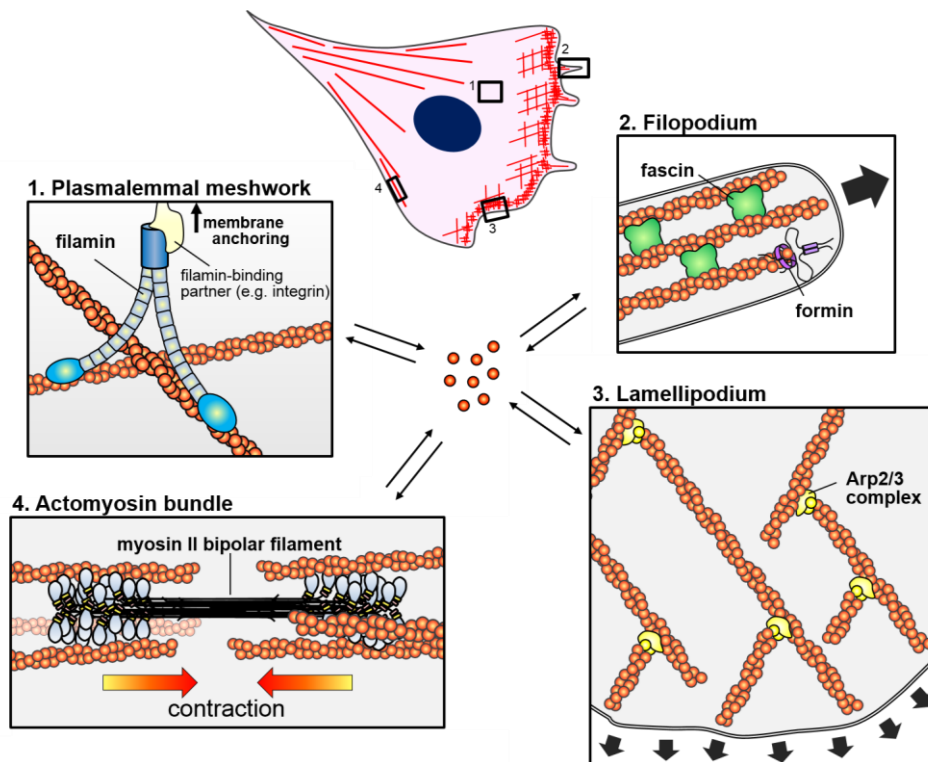


**Fig. 6. Various actin cytoskeletal structures.**

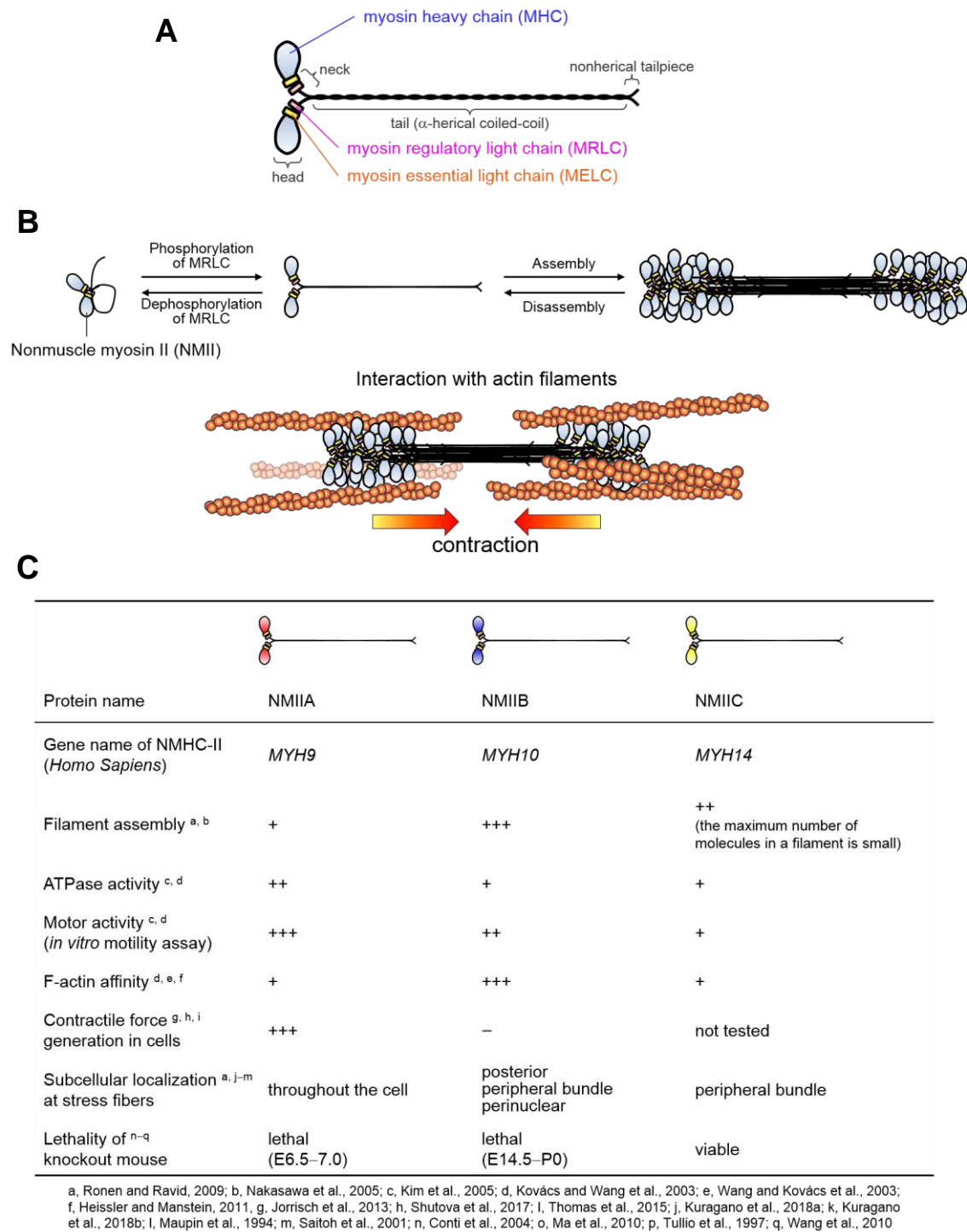


**Fig. 7. Common myosin II structure and unique dynamics/kinetics of nonmuscle myosin II (NMII).**

(A) Common structure of type II myosin. (B) Dynamic property of NMII. (C) NMII isoform properties.

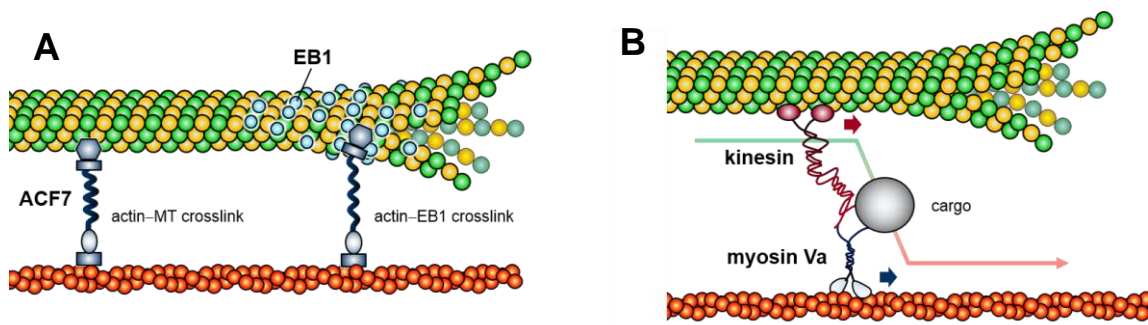


**Fig. 8. Direct crosslink between actin and MT cytoskeletons.**

- (A) Static actin–MT crosslink by cytoskeletal linker protein.
- (B) Transient actin–MT crosslink by motor proteins.

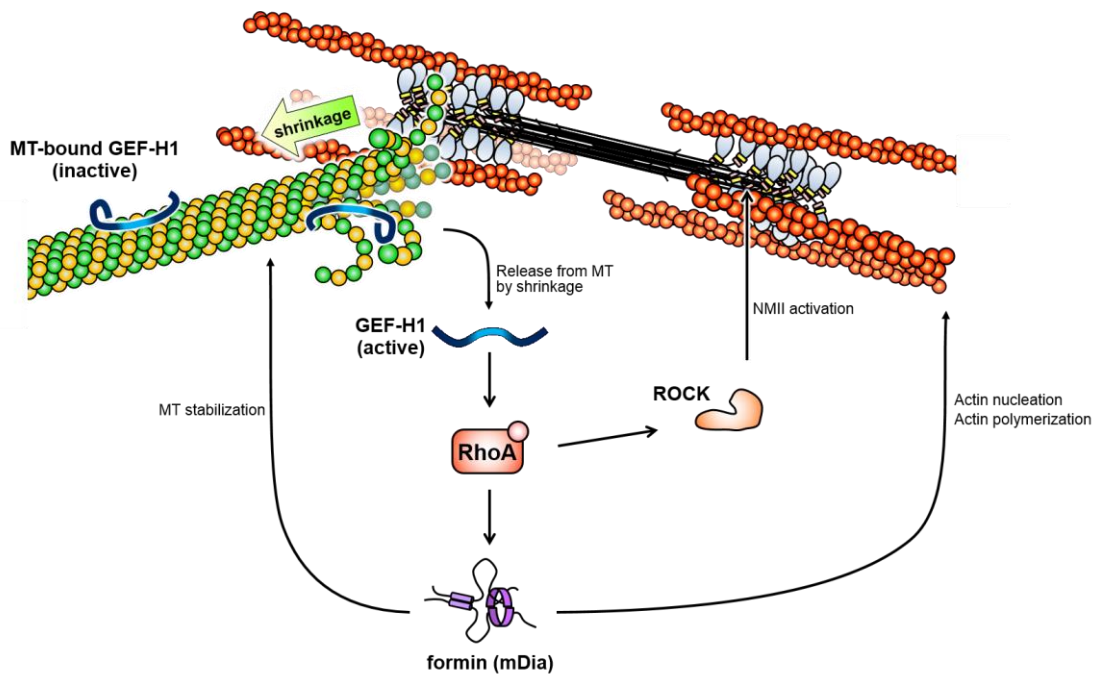


**Fig. 9. RhoA-mediated actin–MT crosstalk.**

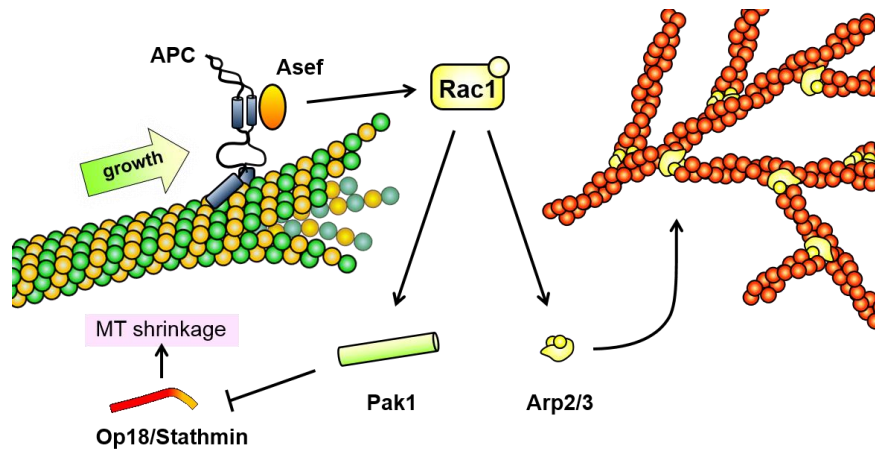


**Fig. 10. Rac1-mediated actin–MT crosstalk.**

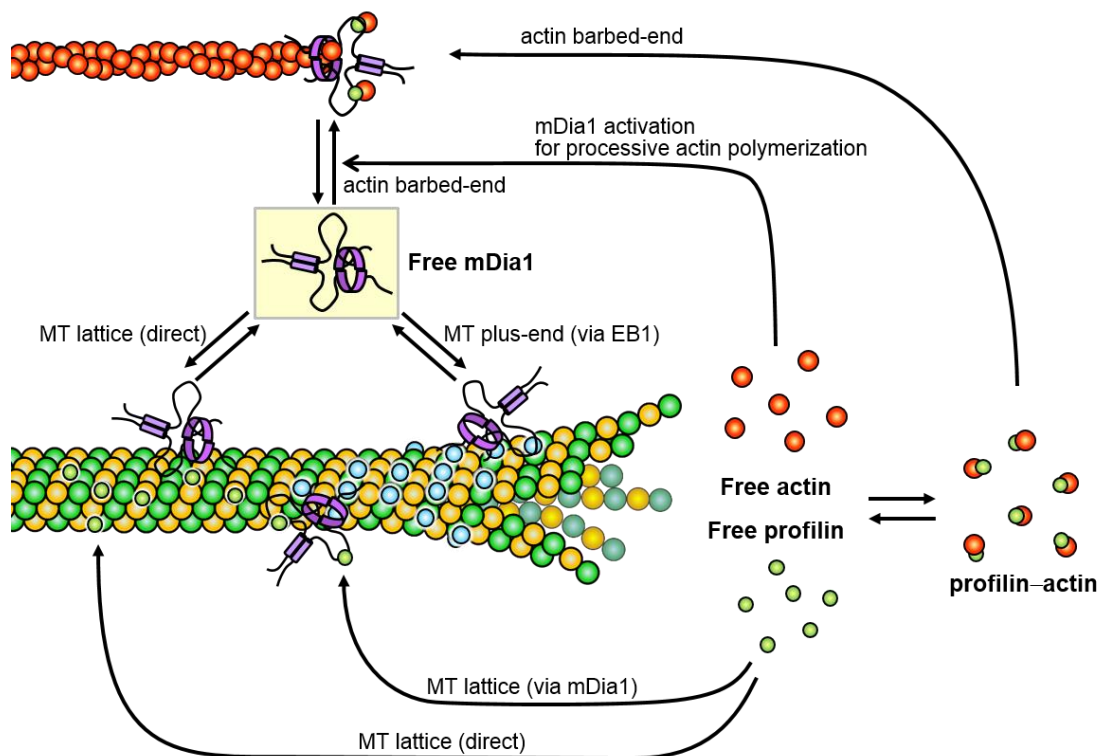


**Fig. 11. Formin/profilin-mediated actin–MT crosstalk.**

## ***Chapter 2.***

### **Establishment of “SERCYF (semi-retentive cytoskeletal fractionation)-method”, for simultaneous analysis of microtubules and actin cytoskeletons.**

---

#### **2.1. Abstract**

A variety of biochemical fractionation methods are available for quantification of cytoskeletal components. However, each method is designed to target only the one cytoskeletal network, either microtubule (MT) or actin cytoskeletons, and the non-targeted cytoskeletal networks are ignored. Considering the importance of MT–actin crosstalk, organizations of both the targeted and non-targeted cytoskeletal networks must be retained intact during fractionation for an accurate analysis of cytoskeletal organization. In this study, I show that existing fractionation methods, represented by MT-sedimentation-method for MTs and Triton X-100 solubility assay-method for actin cytoskeletons, disrupt the organization of the non-targeted cytoskeletons. I demonstrate a novel fractionation method for an accurate analysis of cytoskeletal organizations using taxol-containing PEM-based permeabilization buffer, which I name “semi-retentive cytoskeletal fractionation (SERCYF)-method”. The organizations of both MTs and actin cytoskeletons were retained intact even after permeabilization with this buffer. By using SERCYF-method, I analyzed the effects of nocodazole on cytoskeletal organizations biochemically and showed a promotion of the actin cytoskeletal organization by MT depolymerization, confirming that this method is suitable for simultaneous fractionation of different cytoskeletal networks.

#### **2.2. Introduction**

MTs and actin cytoskeletons are abundant subcellular components that regulate cell shape and motility (Kaverina and Straube, 2011; Pollard and Borisy, 2003). Their organizations change spatiotemporally through dynamic assembly/disassembly events in response to various signaling cues. The dynamic behaviors of MTs and actin cytoskeletons are mediated by their binding proteins, post-translational modifications, in addition to their polymerization/depolymerization. Moreover, MTs and actin cytoskeletons crosstalk to regulate their dynamics and/or stability with each other (Rodriguez et al., 2003), which is important for cell motility. MT–actin crosstalk is mediated by many factors, including linker proteins and small GTPases. The loss of MT–actin crosstalk impairs cell motility.

We can analyze cytoskeletal organizations biochemically by estimating the percentage of cytoskeletal components that are incorporated into the assembled cytoskeletons. This relies on several fractionation methods that prepare cytoskeletal (insoluble) and cytoplasmic (soluble, free) fractions of MTs (Bender et al., 2014; Nagae et al., 2013; Nejedla et al., 2016) and actin

cytoskeletons (Breckenridge et al., 2009; Dahan et al., 2014; Kiboku et al., 2013; Kolega, 1997). In these methods, cells are permeabilized with a surfactant-containing buffer, and then subcellular components are separated into cytoskeletal and cytoplasmic fractions through a method-specific procedure. In most cases, the fractionated proteins are quantified by immunoblot analysis (Fig. 12).

To perform accurate analysis of MT and actin cytoskeleton networks, the integrity of both cytoskeletons must be maintained throughout the experiment because they affect each other. However, the targeted cytoskeleton of the existing methods is either MT or actin cytoskeleton. In other words, organization of the non-targeted cytoskeletons is ignored, thus, they may exhibit abnormal organization. Irregularities in the non-targeted cytoskeletons may affect organization of the targeted cytoskeletons due to the existence of MT–actin crosstalk, leading to data misinterpretation.

To overcome this situation, in this chapter, I aimed to perform an accurate analysis of organization of MT and actin cytoskeleton networks. I report here the establishment of a novel fractionation method for an accurate biochemical analysis of MTs and actin cytoskeletons simultaneously, which is not possible using existing methods.

## **2.3. Results**

### **2.3.1. Treatment with buffers for existing fractionation methods induces cytoskeletal disruption**

First, I examined whether MT and actin cytoskeleton networks are retained intact after permeabilization with existing fractionation buffers. Although several investigators have performed cytoskeletal fractionations, there is no established protocol using a common buffer composition and procedure. Here, I tested whether MT sedimentation (MTS)- (Nagae et al., 2013) and Triton X-100 solubility assay (TSA)- (Kiboku et al., 2013) methods, representatives of the existing methods which are designed for MTs and actin cytoskeletons, respectively, can retain both cytoskeletons (Table 1). MRC-5 SV1 TG1 (hereafter, SV1) cells were used in this study because they exhibit prominent MTs and stress fibers (contractile structures mainly consisting of actin filaments and NMII filaments (Burrige and Wittchen, 2013)) (Fig. 13). Cells were permeabilized with MTS- or TSA-buffer prior to fixation and immunostaining, according to method-specific conditions. After treatment with MTS-buffer, MTs were visible, however, their morphology was abnormal; they were bundled, a characteristic of hyperstable MTs (Fig. 13). Furthermore, actin cytoskeletons were also abnormal, with thick and winding bundles. This defect could be related to a removal of nonmuscle myosin IIA (NMIIA), a major isoform of NMII in SV1 cells (Sato et al., 2007), from the actin cytoskeletons. Consistent with these results,

immunoblot analysis showed that subpopulations of  $\alpha$ -tubulin and  $\beta$ -actin, but not NMHC-IIA (a heavy chain subunit of NMIIA), were present in the cytoskeletal fraction (Fig. 14). Acetylated  $\alpha$ -tubulin, a modified form that accumulates in stable MTs (Al-Bassam and Corbett, 2012), was mainly detected in the cytoskeletal fraction. In the case of the TSA-method, immunofluorescence microscopy showed that, while distribution of the actin cytoskeletons was retained intact, most MTs were depolymerized during permeabilization (Fig. 13). Immunoblot analysis showed similar results; while subpopulations of  $\beta$ -actin and NMHC-IIA were present in the cytoskeletal fraction, almost all  $\alpha$ -tubulin was present in the cytoplasmic fraction (Fig. 14). In addition, acetylated  $\alpha$ -tubulin was detected in both cytoskeletal and cytoplasmic fractions, indicating that a subset of MTs was improperly fractionated into the cytoplasmic fraction. Altogether, these results demonstrate that MTS- and TSA-methods do not reflect precise cytoskeletal organizations in cells because of their partial disruption during permeabilization.

### **2.3.2. PEM-based fractionation buffer does not disrupt cytoskeletons significantly**

To overcome the disadvantages of the existing fractionation methods, I investigated an appropriate buffer for non-disruptive cytoskeletal fractionation. PEM-buffer, which is commercially available as a “general tubulin buffer”, is often used to analyze MTs. Furthermore, Gundersen and his colleagues used PEM-Triton X-100 (PEMT)-buffer for cell permeabilization and subsequent MT observation (Infante et al., 2000). Although they made no mention of the integrity of the actin cytoskeletons after PEMT-buffer treatment, overall cell shape appeared to be unaffected, implying that the cells maintained actin cytoskeletons properly. To test this possibility, we performed immunofluorescence microscopy after permeabilization with PEMT-buffer (Fig. 15). After 60 sec-permeabilization, I found that organizations of the actin cytoskeletons as well as MTs were retained intact, indicating that PEMT-buffer has a potential for non-disruptive fractionation of the both cytoskeletons. However, I also found that, while overall organization of the actin cytoskeletons was not affected by 180 sec-permeabilization, MT density decreased with permeabilization time, indicating that MTs depolymerized gradually. For biochemical analysis, I fractionated cells into cytoskeletal and cytoplasmic fractions as illustrated in Fig. 15. I analyzed permeabilization-time dependencies of the fractionated proteins and found that MTs depolymerized during permeabilization; the percentage of cytoskeletal  $\alpha$ -tubulin was constant (~50%) from 30 to 90 sec and significantly decreased (~40%) at 120 sec after permeabilization (Fig. 17A, C), which was comparable to the results of immunofluorescence microscopy.

### **2.3.3. Addition of low-dose taxol into PEMT-buffer achieves semi-retentive cytoskeletal fractionation**

To block MT depolymerization during PEMT-buffer treatment, I added a low dose (100 nM) of

taxol to PEMT-buffer (termed PEMTT-buffer). Immunofluorescence microscopy revealed that permeabilization with PEMTT-buffer did not induce MT depolymerization, even after 180 sec treatment (Fig. 16). Notably, bundled MTs were not observed after PEMTT-buffer treatment, confirming that this concentration of taxol did not induce MT hyperstabilization. Immunoblot analysis revealed that the percentage of cytoskeletal  $\alpha$ -tubulin was constant (~70%) from 30 to 120 sec after permeabilization (Fig. 17B–C), supporting the idea that neither MT depolymerization nor hyperstabilization was induced by addition of low-dose taxol. Importantly, permeabilization with PEMTT-buffer did not affect distribution of the actin cytoskeletons (Fig. 17B, D–E). Altogether, these results show that the fractionation procedure using PEMTT-buffer enabled immunofluorescence and biochemical analysis of intact MT and actin cytoskeleton networks. I then defined “60 sec” as an ideal permeabilization time for the new method because the time-dependent percentage changes of  $\alpha$ -tubulin,  $\beta$ -actin, and NMHC-IIA were small around 60 sec. Furthermore, acetylated  $\alpha$ -tubulin was reasonably detected only in the cytoskeletal fraction (Fig. 18). Thus, I named this improved fractionation method “semi-retentive cytoskeletal fractionation (SERCYF)-method”, by which we can perform simultaneous and accurate analysis of cytoskeletal organizations.

I then tested whether the SERCYF-method could be used to study other cell types and/or other types of actin cytoskeletons. For this purpose, I used U-2 OS human osteosarcoma because these cells exhibit an extensive lamellipodial actin network during migration. After permeabilization with PEMTT-buffer for 60 sec, I observed intact MTs and stress fibers through immunofluorescence microscopy (Fig. 19). I also observed lamellipodia, indicating that SERCYF-method did not disrupt organizations of lamellipodia as well as stress fibers. These results strongly support the validity of SERCYF-method for analysis of various types of cells and cytoskeletons.

#### **2.3.4. Verification of the usability of SERCYF-method: analysis of effects of MT depolymerization on actin cytoskeletons**

MTs and actin cytoskeletons affect each other’s organization via crosstalk mediators (Rodriguez et al., 2003). For example, GEF-H1, a MT-associated guanine-nucleotide exchange factor for RhoA, is involved in MT–actin crosstalk (Birkenfeld et al., 2008). Specifically, MT depolymerization induces a release of GEF-H1 from MTs into cytoplasm, resulting in reorganization of the actin cytoskeletons through RhoA activation (Chang et al., 2008; Krendel et al., 2002). To determine whether this crosstalk can be studied by SERCYF-method, I assessed effects of nocodazole, a MT-depolymerizing agent, on the cytoskeletons. Before biochemical analysis, I performed immunofluorescence microscopy of SV1 cells, with or without PEMTT-buffer permeabilization prior to fixation (Fig. 20). In addition to  $\alpha$ -tubulin,  $\beta$ -actin, and NMIIA, I also examined NMIIIB (another isoform of NMHC-II) and vinculin, a component of focal

adhesions (FAs). Without permeabilization, nocodazole-treated cells lost almost all MTs and exhibited denser stress fibers at the cell center compared with control cells. Vinculin was partially localized to FAs, but mostly dispersed into the cytoplasm of control and nocodazole-treated cells. With permeabilization, control cells exhibited normal distribution of both cytoskeletons. Notably, vinculin was localized only to FAs, indicating that cytoplasmic vinculin was removed during permeabilization. Nocodazole-treated cells exhibited only a few MTs, dense stress fibers, and many FAs. An excessive development of FAs is a characteristic of MT depolymerized cells (Enomoto, 1996). These results indicated the existence of MT–actin crosstalk, which is probably mediated through the GEF-H1/RhoA pathway, in SV1 cells. Moreover, permeabilization with PEMTT-buffer prior to fixation is an effective procedure for removal of cytoplasmic components, without disruption of cytoskeletal organizations.

Finally, I investigated effects of nocodazole on the cytoskeletons biochemically (Fig. 21). Consistent with the immunofluorescence results, the percentage of cytoskeletal  $\alpha$ -tubulin decreased to nearly background level, whereas that of  $\beta$ -actin significantly increased in nocodazole-treated cells. Interestingly, the effects of MT depolymerization on each NMHC-II isoform were different; the percentage of cytoskeletal NMHC-IIA was not affected, whereas that of NMHC-IIB increased in nocodazole-treated cells. These results imply that NMII-mediated MT–actin crosstalk exists, and that each isoform (IIA and IIB) contributes differently to this crosstalk. Vinculin was mainly detected in the cytoplasmic fraction of both control and nocodazole-treated cells without an apparent difference between groups, indicating that SERCYF-method is not suitable for biochemical analysis of FA components. Altogether, these results confirm the usefulness of SERCYF-method for accurate and simultaneous quantification of MT, actin filament, and NMII.

## **2.4. Discussion**

### **2.4.1. Possible reasons of cytoskeletal disruption by the use of the existing fractionation methods**

The purpose of this study was to establish a fractionation method for accurate quantification of organizations of MT and actin cytoskeleton networks. I demonstrated that PEMTT-buffer, but not MTS- or TSA-buffers, was suitable for semi-retentive cytoskeletal fractionation, which led me to ask why MTS- and TSA-buffers failed to retain cytoskeletal organizations.

The major difference between MTS- and PEMTT-buffers is the presence of glycerol (Table 1). MTS-buffer contains a high concentration of glycerol that prevents MT depolymerization during fractionation. Although glycerol stabilizes MTs by decreasing a critical concentration of tubulin for polymerization *in vitro* (Na and Timasheff, 1981), which resulted in abnormal

bundling of MTs after MTS-buffer treatment, indicating that it produces an artificial effect on MTs (Fig. 13). Glycerol may also excessively stabilize actin filaments in a similar way, resulting in the formation of thick and winding actin bundles. In contrast, NMII was likely destabilized by glycerol; almost all NMHC-IIA molecules were extracted from the cells (Fig. 14). Although the reason is unclear, interaction between actin and NMII might be reduced by glycerol. Instead of glycerol, I added a low dose of taxol to PEMT-buffer to prevent MT depolymerization during permeabilization. This resulted in the inhibition of MT depolymerization without MT hyperstabilization or any effect on the actin cytoskeletons (Fig. 15, 17). Notably, the percentage of cytoskeletal  $\alpha$ -tubulin quantified with SERCYF-method was significantly higher than that quantified with MTS-method (~70% vs ~40%). The results obtained using SERCYF-method appear to better reflect the situation in cells, judging from the normal cytoskeletal organizations after PEMTT-buffer (but not MTS-buffer) treatment in immunofluorescence microscopy.

There are some significant differences between TSA- and PEMTT-buffers, namely, PIPES concentration, salt concentration, and temperature during permeabilization (Table 1). Olmsted and Borisy reported that a buffer containing a high concentration of PIPES (maximal at 100 mM) and a physiological concentration of salt (150 mM) is best for purified tubulin polymerization *in vitro* (Olmsted and Borisy, 1975). TSA-buffer contains PIPES at a standard concentration (20 mM); however, its ability to maintain MT organization is likely insufficient (Fig. 13, 14). Although PEM-buffer does not contain additional salts, such as NaCl, 100 mM PIPES-NaOH (pH 6.8) already provides a considerable sodium ion concentration. Thus, PEM-buffer might meet the requirements of both PIPES and salt concentrations. Addition of a specific amount of salt to PEM-based permeabilization buffer might further improve the method. Furthermore, it is critical to maintain the temperature at 37°C during fractionation because MTs undergo depolymerization at lower temperatures. TSA-buffer treatment at 25°C would also cause MT depolymerization.

Although previous studies used PEMT-buffer for cytoskeletal fractionation (Dahan et al., 2014; Nejedla et al., 2016), experimental procedures of SERCYF-method differs from theirs. Nejedla et al. applied PEMT-buffer to cells collected by scraping and centrifugation (Nejedla et al., 2016). Because the goal of this study was to establish a fractionation method that does not affect cytoskeletal organization, I avoided any step that could affect cell shape (i.e. scraping and centrifugation). Dahan et al. used PEMT-buffer to fractionate NMHC-IIA in procedures similar to SERCYF-method, except that they incubated cells with PEMT-buffer on ice for 5 min (Dahan et al., 2014). They probably used a low temperature to prevent protein denaturation; however, I maintained the temperature at 37°C for two reasons. Firstly, as mentioned above, MTs depolymerize at lower temperatures. Secondly, low temperatures are likely to decrease a permeabilizing activity of surfactants. Indeed, large molecules, such as NMHC-IIA, were difficult to extract from cells at low temperatures (Fig. 22). Thus, the reduced surfactant activity requires a longer time for sufficient permeabilization. I therefore adopted a warm temperature (37°C) and

a short time (1 min) for permeabilization.

#### **2.4.2. Limits of SERCYF-method and future perspectives**

Based on arguments for buffer compositions and experimental procedures, I established SERCYF-method as illustrated in Fig. 16. By using this method, I achieved simultaneous fractionation of intact MTs and actin cytoskeletons. The usefulness of this method was evaluated by analyzing the effects of MT depolymerization on the actin cytoskeletons (Fig. 20, 21). This method was successful in analyzing a crosstalk between MTs and actin cytoskeletons and revealed that the percentages of cytoskeletal  $\beta$ -actin and NMHC-IIB increase after MT depolymerization. However, the percentage of cytoskeletal vinculin was unaffected, which is in conflict with an increase in the number of FAs in nocodazole-treated cells observed in immunofluorescence microscopy. The rinsing step during fractionation might cause this discrepancy; a binding activity of vinculin to FAs after permeabilization was probably too weak to resist rinsing with PEM-buffer. Despite this disadvantage, permeabilization with PEMTT-buffer prior to fixation is an effective procedure for immunofluorescence observation of FAs because they became more visible due to a removal of cytoplasmic components.

In addition to analysis of cytoskeletal organizations, SERCYF-method can be used for identification of some unique or specific cytoskeletal proteins between different cell types or conditions. Between normal and immortalized (or cancer) cells, cell shape (Pawlak and Helfman, 2001; Verderame et al., 1980; Yamada et al., 1976) and migration mode (Kuragano, 2018) are different. Considering that cytoskeletons play roles in determination of such properties, investigation of cytoskeletal proteins that differ between different cell types may help studies of cell behaviors in physiological and pathological conditions. Our group preliminary performed comparison of cytoskeletal fractions between normal and immortalized fibroblasts by SERCYF-method. Interestingly, the bands stained by CBB showed different patterns between these cell types (Fig. 23). As a next project, protein identification of these bands is ongoing.

#### **2.5. Conclusion**

In this chapter, I established SERCYF-method as a cytoskeletal fractionation procedure in which biochemical analysis can be performed without significant disruption of MTs or actin cytoskeletons. Thus, using this novel method, it is possible to analyze a specific cytoskeleton for study without having to change buffer compositions or experimental procedures. Because of this high versatility, this method will accelerate studies of MTs, actin cytoskeletons, and also their crosstalk.

## **2.6. Experimental procedures**

### **2.6.1. Cell culture**

MRC-5 SV1 TG1 cells (SV40-transformants of MRC-5; human embryonic lung fibroblasts) (RIKEN Cell Bank, Tsukuba, Japan) were maintained in Minimum Essential Medium Eagle (MEM) alpha (GIBCO/Life Technologies, Carlsbad, CA, USA) supplemented with 10% fetal bovine serum (FBS) (BioSource/Life Technologies), 50 U/mL penicillin and 50 mg/mL streptomycin (GIBCO). U-2 OS cells (human osteosarcoma) were kindly gifted from Dr. Keiju Kamijo (Tohoku Medical and Pharmaceutical University, Sendai, Japan) and were maintained in McCoy's 5A (modified) medium (GIBCO) supplemented with 10% FBS, 50 U/mL penicillin and 50 µg/mL streptomycin. All cells were cultured at 37°C in humidified air containing 5% CO<sub>2</sub>. Where indicated, nocodazole (Millipore Calbiochem, Billerica, MA, USA) was added to the culture medium at a final concentration of 10 µM, 1 hour before analysis.

### **2.6.2. Antibodies**

For immunofluorescence microscopy, primary antibodies were diluted as follows: mouse anti-β-actin monoclonal antibody (1:5000) (AC-15; SIGMA-Aldrich, St. Louis, MO, USA), rabbit anti-NMHC-IIA polyclonal antibody (1:5000) (Sato et al., 2007), rabbit anti-NMHC-IIB polyclonal antibody (1:5000) (Saitoh et al., 2001), and mouse anti-vinculin monoclonal antibody (1:5000) (hVIN-1; SIGMA-Aldrich). Secondary antibodies (Jackson ImmunoResearch Laboratories; West Grove, PA, USA) were diluted as follows: Cy3-labeled anti-mouse IgG (1:500), AMCA-labeled anti-rabbit IgG (1:200), and Alexa Fluor 488-labeled anti-rabbit IgG (1:200). Direct immunofluorescence of microtubules was performed using a FITC-labeled mouse anti-α-tubulin monoclonal antibody (1:1500) (a kind gift from Dr. Keiju Kamijo). For immunoblotting, primary antibodies were diluted as follows: mouse anti-α-tubulin monoclonal antibody (1:2000) (B-5-1-2; SIGMA-Aldrich), mouse anti-acetyl-α-tubulin monoclonal antibody (1:500) (6-11B-1; SIGMA-Aldrich), mouse anti-β-actin monoclonal antibody (1:2000), mouse anti-vinculin monoclonal antibody (1:500), mouse anti-GAPDH monoclonal antibody (1:30,000) (6C5; Millipore), rabbit anti-NMHC-IIA polyclonal antibody (1:60,000), and rabbit anti-NMHC-IIB polyclonal antibody (1:2000). Secondary antibodies (Bio-Rad Laboratories, Hercules, CA, USA) were diluted as follows: HRP-labeled anti-mouse IgG (1:10,000) and HRP-labeled anti-rabbit IgG (1:10,000).

### **2.6.3. Cell fractionation by MTS-method**

MTS-method was performed as described by Nagae et al. (Nagae et al., 2013) (see also Table 1). Cells were washed with 1 mL of pre-warmed (37°C) PBS and gently permeabilized with 180 µL of pre-warmed MTS-buffer, followed by incubation at 37°C for 15 min with gentle shaking every

5 min. The permeabilized cells were scraped with a cell scraper and collected into a plastic tube, followed by centrifugation ( $110,000 \times g$ , 1 hour,  $37^{\circ}\text{C}$ ). The resulting supernatant was transferred into a new plastic tube and mixed with 220  $\mu\text{L}$  of 2 $\times$ SDS sample buffer [100 mM Tris-HCl (pH 6.8), 4% SDS, 20% glycerol, 0.2% bromophenolblue] supplemented with  $\beta$ -mercaptoethanol ( $\beta$ -ME) at a final concentration of 5% (hereafter, the 2 $\times$ SDS sample buffer always contained  $\beta$ -ME) (cytoplasmic fraction). The resulting pellet was resuspended with 180  $\mu\text{L}$  of SDS lysis buffer [10 mM Tris-HCl (pH 7.5), 2 mM EDTA, 1% SDS] and mixed with 220  $\mu\text{L}$  of 2 $\times$ SDS sample buffer (cytoskeletal fraction). The samples were further denatured by boiling for 3 min.

#### **2.6.4. Cell fractionation by TSA-method**

TSA-method was performed as previously described (Kiboku et al., 2013) (see also Table 1). Cells were washed with 1 mL of pre-warmed PBS and gently permeabilized with 180  $\mu\text{L}$  of TSA-buffer, followed by incubation at  $25^{\circ}\text{C}$  for 3 min with gentle shaking every 1 min. The permeabilized cell extract was collected into a plastic tube, followed by centrifugation ( $22,000 \times g$ , 3 min,  $4^{\circ}\text{C}$ ). The resulting supernatant was transferred into a new plastic tube and was mixed with 220  $\mu\text{L}$  of 2 $\times$ SDS sample buffer (cytoplasmic fraction). The permeabilized cells remaining in the well were directly lysed with 220  $\mu\text{L}$  of 2 $\times$ SDS sample buffer and collected into a plastic tube that beforehand contained 180  $\mu\text{L}$  of TSA-buffer (cytoskeletal fraction). The samples were further denatured by boiling for 3 min.

#### **2.6.5. Cell fractionation by SERCYF-method**

SERCYF-method was performed as previously described (Sato et al., 2017) (see also Table 1). Cells were cultured on separate 24 well-plates when two or more samples were prepared, in order to avoid excessive permeabilization or peel-off of cells from wells during handling of other samples. Cells were once washed with 1 mL of pre-warmed PEM-buffer [100 mM PIPES-NaOH (pH 6.8), 1 mM EGTA, 2 mM  $\text{MgCl}_2$ ] and permeabilized with 150  $\mu\text{L}$  of pre-warmed PEMTT-buffer [PEM containing 100 nM (for SV1 cells) or 10 nM (for U-2 OS cells) taxol and 0.2% Triton X-100] at  $37^{\circ}\text{C}$  for 1 min, without shaking. The permeabilized cell extract was collected into a plastic tube. 120  $\mu\text{L}$  of pre-warmed PEM-buffer was gently added to the residual cells, and the resulting rinse buffer was immediately collected into the same tube. This cytoplasmic fraction was mixed with 330  $\mu\text{L}$  of 2 $\times$ SDS sample buffer. As a cytoskeletal fraction, the remaining cells were directly lysed with 330  $\mu\text{L}$  of 2 $\times$ SDS sample buffer and collected into a plastic tube that beforehand contained 150  $\mu\text{L}$  of PEMTT-buffer and 120  $\mu\text{L}$  of PEM-buffer. Both cytoplasmic and cytoskeletal fractions were further denatured by boiling for 3 min. To keep the system temperature at  $37^{\circ}\text{C}$ , culture plate was placed on a melted-ice pack which had been warmed in the incubator for at least one overnight. During the development of SERCYF-method, PEMT-buffer [PEM containing 0.2% Triton X-100], instead of PEMTT-buffer, was used.

### **2.6.6. Immunofluorescence microscopy**

A rapid fixation with methanol was adopted to avoid MT depolymerization. Cells cultured on fibronectin- (10 µg/mL; Roche Diagnostics, Basel, Switzerland) coated coverslips (Matsunami, Kishiwada, Japan) were fixed and permeabilized with cold methanol for 5 min at -20°C. For observation of pre-permeabilized cells, gentle permeabilization was performed prior to fixation. Buffer compositions and conditions are listed in Table 1. The coverslips were incubated with blocking buffer (3% bovine serum albumin (BSA) in PBS) for 15 min, followed by incubation with primary antibodies and corresponding secondary antibodies in blocking buffer sequentially. Each incubation step was performed for 1 hour at room temperature. The coverslips were rinsed with deionized water and mounted in DABCO to prevent bleaching. Immunofluorescence images were obtained using a fluorescence microscope (BX50WI; Olympus, Tokyo, Japan), equipped with a single chip color CCD camera (DP70; Olympus) and an objective lens (UPlanApo 60×/0.90; Olympus). Image processing was performed using ImageJ software.

### **2.6.7. SDS-PAGE and Immunoblotting**

SDE-PAGE was performed in a standard protocol described by Laemmli. Briefly, 10 µl (for MTS- and TSA-method) or 15 µl (for all experiment except MTS- or TSA-method) of SDS samples were separated by using 10% polyacrylamide gel in the running buffer [25 mM Tris, 0.1% SDS, 192 mM glycine]. The gel was washed with deionized water and was soaked with soaking buffer for 10 min. Proteins separated in the gel was transferred to the PVDF membrane (Millipore). The membrane was immediately blocked in blocking buffer [5% skimmed milk in TBS-T (20 mM Tris, 150 mM NaCl, 0.05% Tween-20)] for 30 min at room temperature, followed by incubation with primary antibodies in blocking buffer overnight at 4°C. The membrane was further incubated with secondary antibodies for 1 hour at room temperature. Chemiluminescent signals were produced using Immobilon Western Chemiluminescent HRP Substrate (Millipore) and detected using a LAS-3000 (Fujifilm, Tokyo, Japan). The percentages of cytoskeletal fractions were calculated by densitometry using ImageJ software.

**Table 1. Comparison of the fractionation methods**

Method	Buffer composition	Permeabilization condition	Separation step	Fractionation efficiency (assessed in this study)			Reference
				MT	Actin	NMHC-II	
Microtubule sedimentation (MTS)	100 mM PIPES-NaOH (pH6.8) 2 mM EGTA 5 mM MgCl <sub>2</sub> 2 M Glycerol 2.5 mM GTP 0.1% NP-40 1 × Protease inhibitor cocktail	37°C 15 min	Centrifugation (110,000 × g, 1 h)	Δ	Δ	×	Nagae et al., 2013
Triton X-100 solubility assay (TSA)	20 mM PIPES-NaOH (pH6.8) 150 mM KCl 10 mM Imidazole 1 mM EGTA 1 mM MgCl <sub>2</sub> 1 mM DTT 0.05% Triton X-100 1 × Phosphatase inhibitor 1 × Protease inhibitor cocktail	25°C 3 min	Collection of cell extract as the cytoplasmic fraction	×	○	○	Kiboku et al., 2013
PIPES-EGTA-magnesium-Triton (PEMT)	100 mM PIPES-NaOH (pH6.8) 1 mM EGTA 2 mM MgCl <sub>2</sub> 0.2% Triton X-100 1 × Protease inhibitor cocktail	37°C 15–120 sec (see text)	Collection of cell extract as the cytoplasmic fraction	Δ	○	○	Infante et al., 2000
Semi-retentive cytoskeletal Fractionation (SERCYF)	100 mM PIPES-NaOH (pH6.8) 1 mM EGTA 2 mM MgCl <sub>2</sub> 100 nM Taxol 0.2% Triton X-100 1 × Protease inhibitor cocktail	37°C 1 min (see text)	Collection of cell extract as the cytoplasmic fraction	○	○	○	Sato et al., 2017

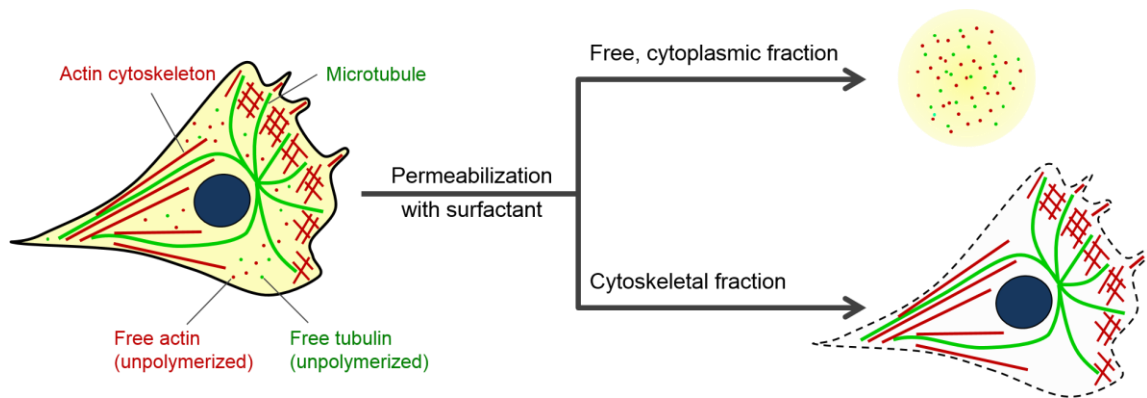


**Fig.12. Concept of cytoskeletal fractionation.**

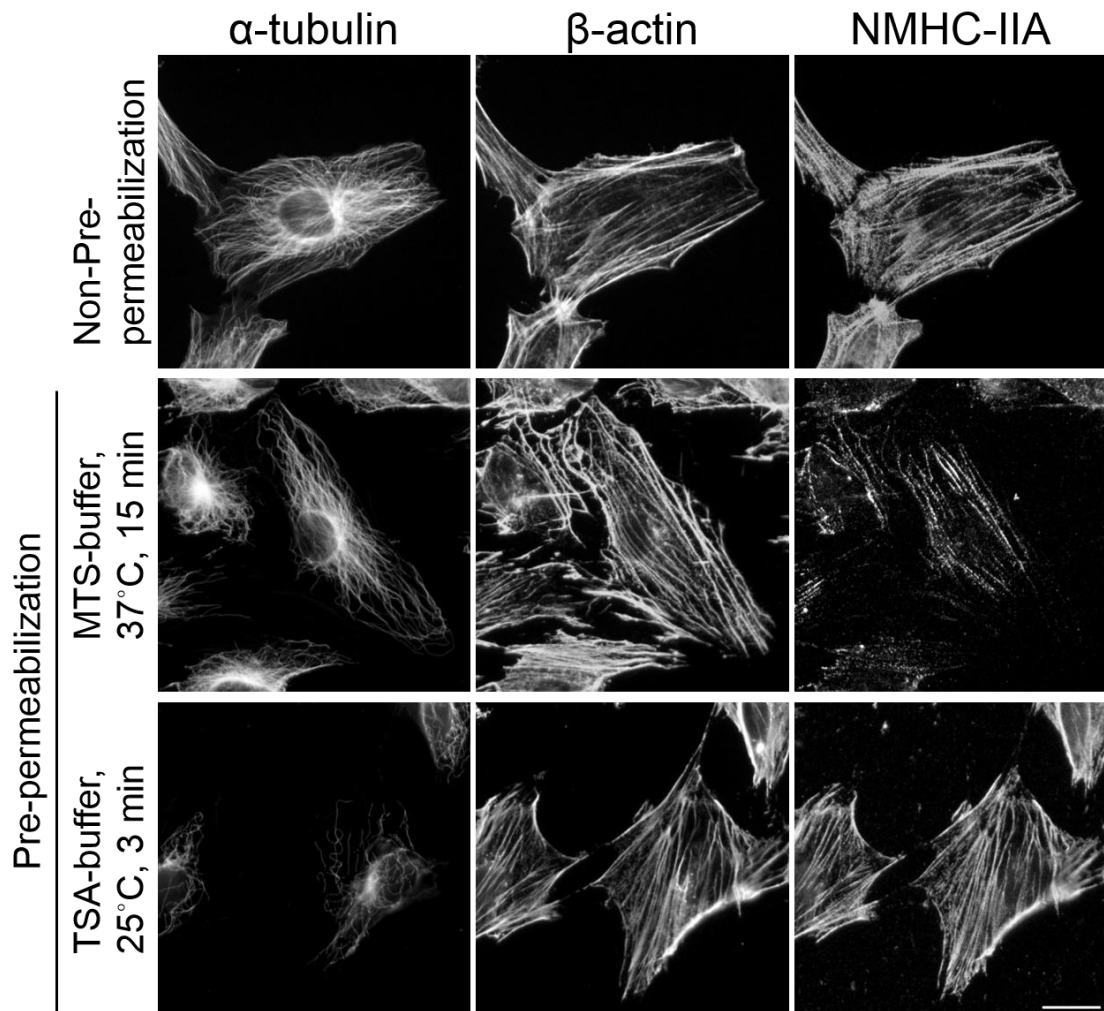


**Fig. 13. Immunofluorescence microscopy for the assessment of pre-existing fractionation methods.**

Immunostaining images of  $\alpha$ -tubulin,  $\beta$ -actin, and NMHC-IIA in non-pre-permeabilized and pre-permeabilized cells under the indicated conditions. Scale bar, 20  $\mu$ m.

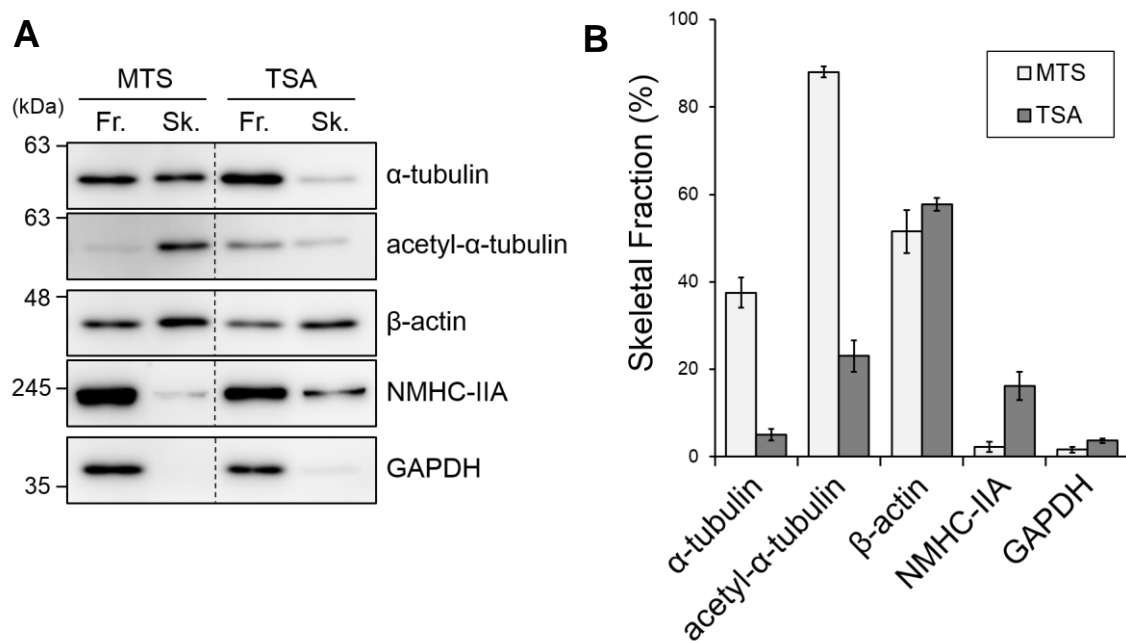


**Fig. 14. Immunoblotting for the assessment of pre-existing fractionation methods.**

(A) Immunoblots of fractionated proteins prepared by MTS- or TSA-method. “Fr.” indicates free, cytoplasmic fractions, “Sk.” indicates cytoskeletal fractions. Anti-GAPDH antibody and anti-acetyl- $\alpha$ -tubulin antibody were used as indicators of cytoplasmic fractions and cytoskeletal fraction, respectively. (B) The percentages of cytoskeletal fractions, calculated from (A). Data represent mean  $\pm$  SEM from three independent experiments.

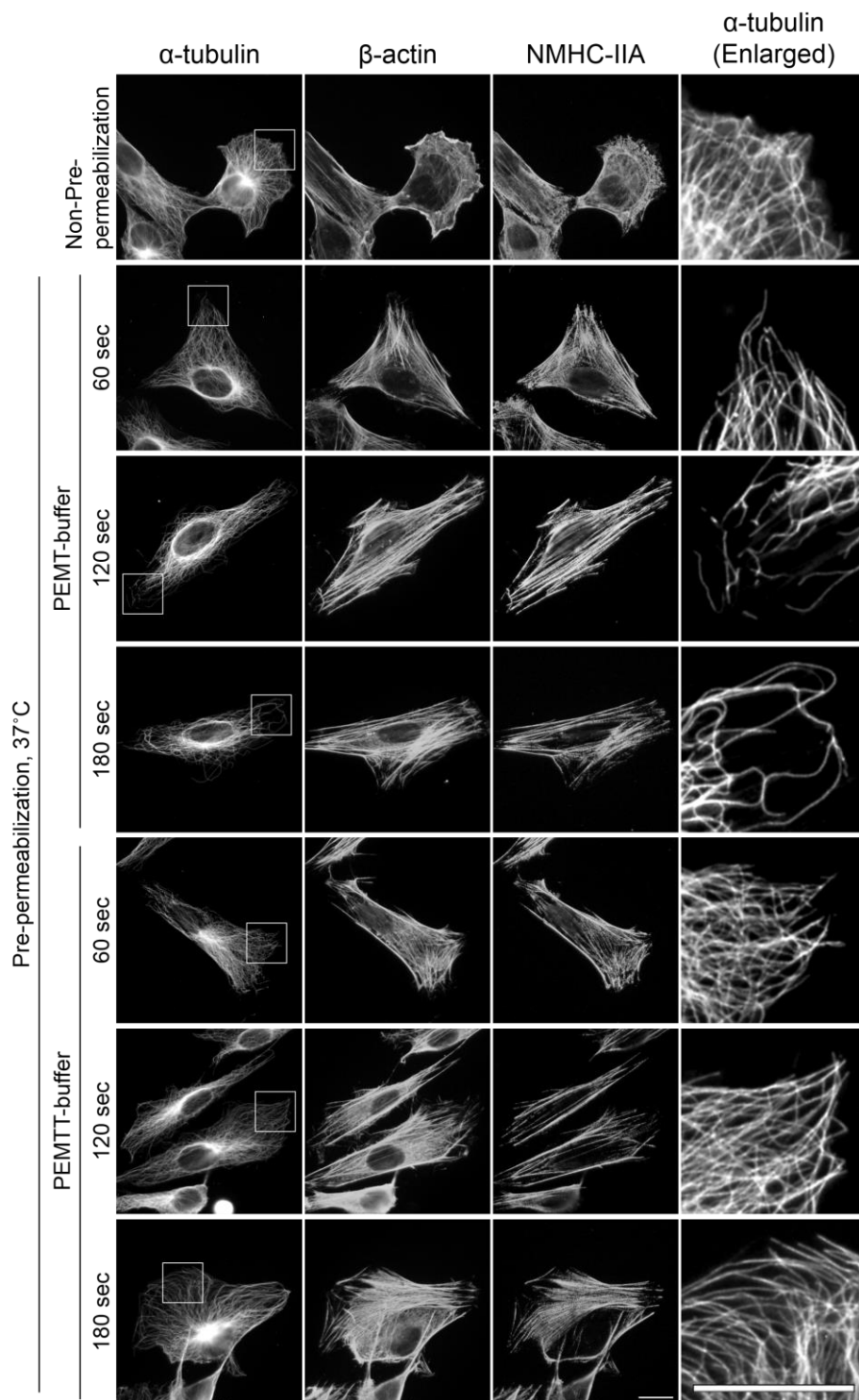


**Fig. 15. Immunofluorescence microscopy for the assessment of a PEM-based fractionation method.**

Immunostaining images of  $\alpha$ -tubulin,  $\beta$ -actin, and NMHC-IIA in non-pre-permeabilized and pre-permeabilized cells under the indicated conditions. Areas indicated by squares in each  $\alpha$ -tubulin image were enlarged. Scale bar, 20  $\mu$ m.

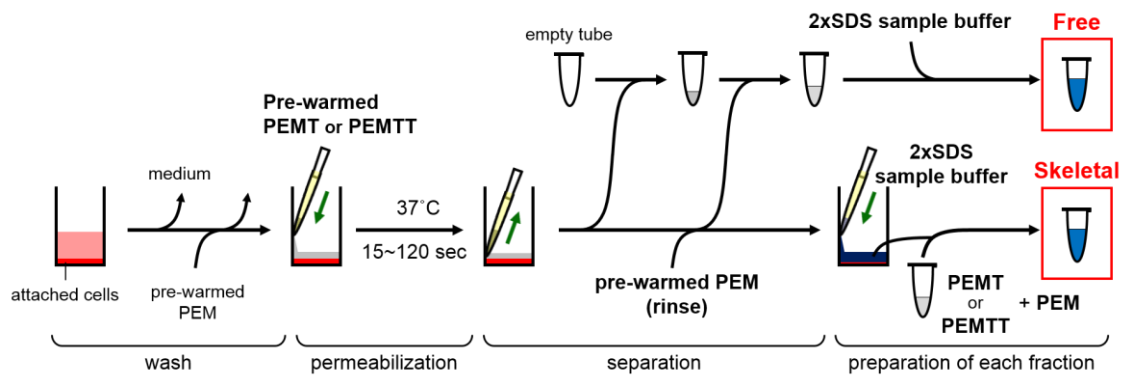


**Fig. 16. Schematic illustration depicting the experimental procedure for the preparation of SDS samples by a PEM-based fractionation method.**

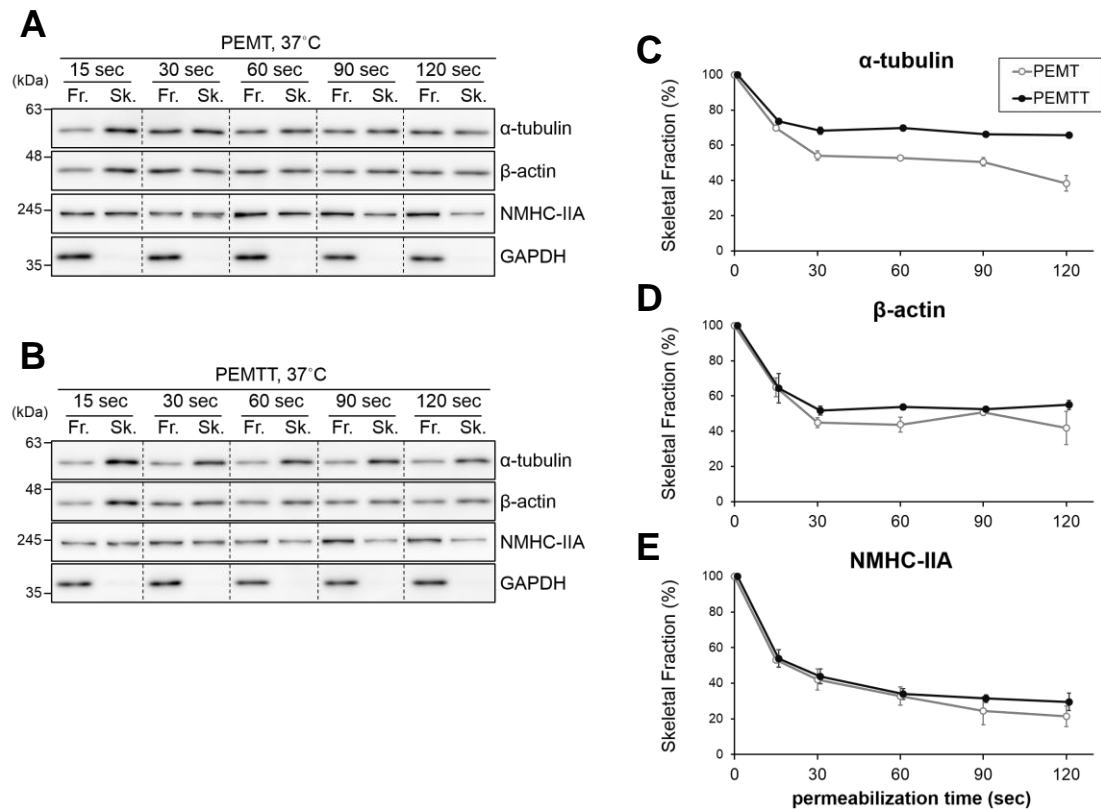


**Fig. 17. Immunoblotting for the assessment of a PEM-based fractionation method.**

(A, B) Immunoblots of fractionated proteins prepared with PEMT- (A) or PEMTT-buffer (B) from cells permeabilized at the indicated time points at 37°C. (C–E) The percentages of cytoskeletal fractions, calculated from (A; gray lines) and (B; black lines). Data represent mean  $\pm$  SEM from three independent experiments. The values at 0 sec (without permeabilization) were regarded as 100%.

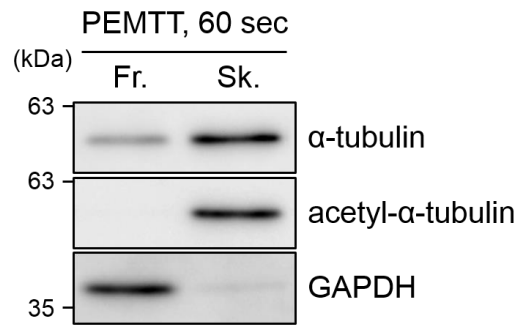


**Fig. 18. Immunoblotting for the validation of usability of SERCYF-method.**

Immunoblots of fractionated proteins prepared by SERCYF-method (PEMTT-buffer, 60 sec permeabilization at 37°C).

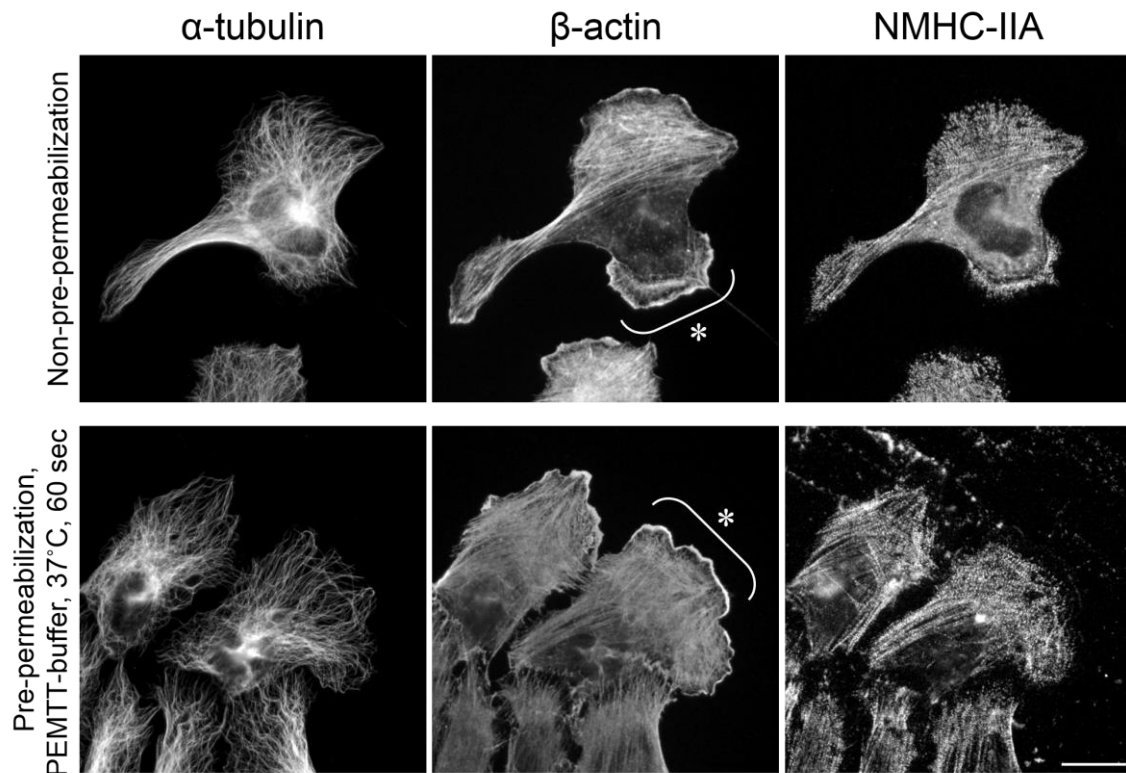


**Fig. 19. Immunofluorescence microscopy for the validation of usability of SERCYF-method in different cell types and different actin cytoskeletal structures.**

Immunostaining images of  $\alpha$ -tubulin,  $\beta$ -actin, and NMHC-IIA in non-pre-permeabilized and pre-permeabilized U-2 OS cells with PEMTT-buffer for 60 sec at 37°C. Asterisks and brackets indicate representative lamellipodial protrusions. Scale bar, 20  $\mu$ m.

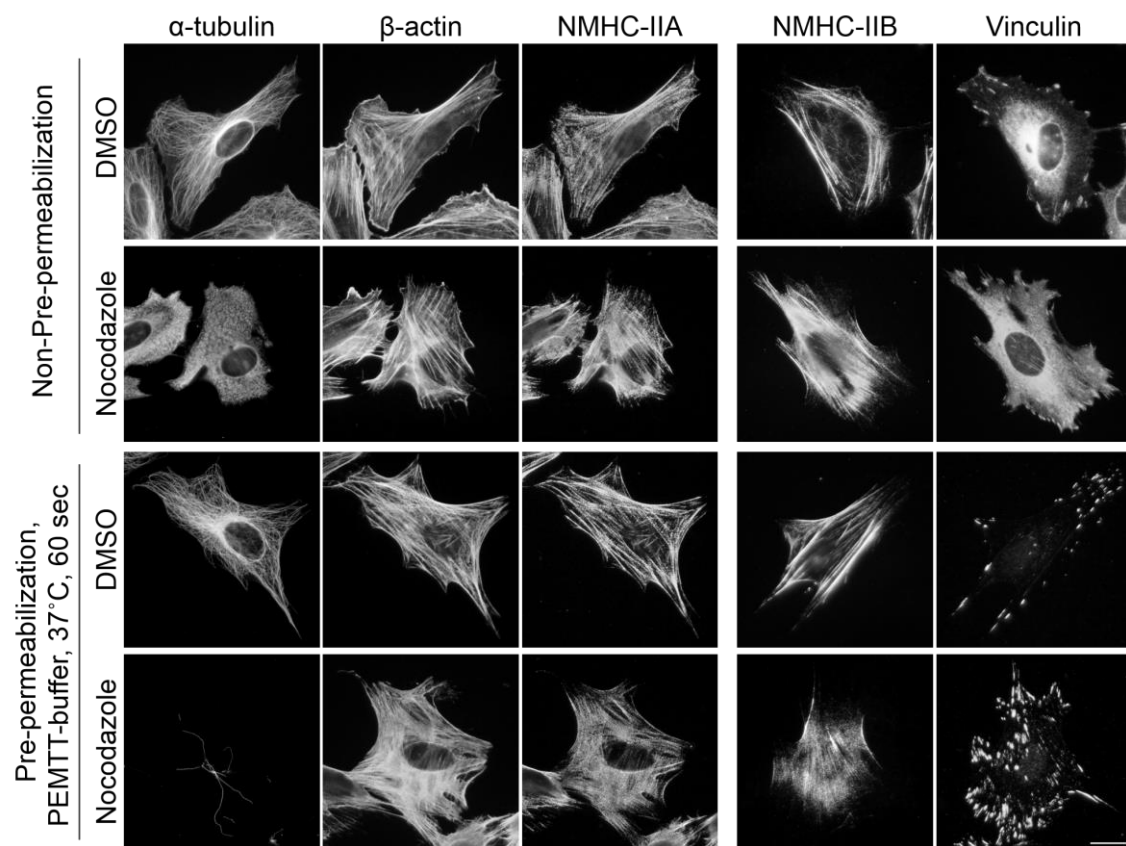


**Fig. 20. Immunofluorescence microscopy for analysis of the effects of nocodazole-induced MT depolymerization on actin cytoskeletons by SERCYF-method.**

Immunostaining images of  $\alpha$ -tubulin,  $\beta$ -actin, NMHC-IIA, NMHC-IIB, and vinculin in non-pre-permeabilized and pre-permeabilized cells with PEMTT-buffer for 60 sec at 37°C. Before fixation or pre-permeabilization, cells were treated with DMSO or 10  $\mu$ M nocodazole for 1 hour. Scale bar, 20  $\mu$ m.

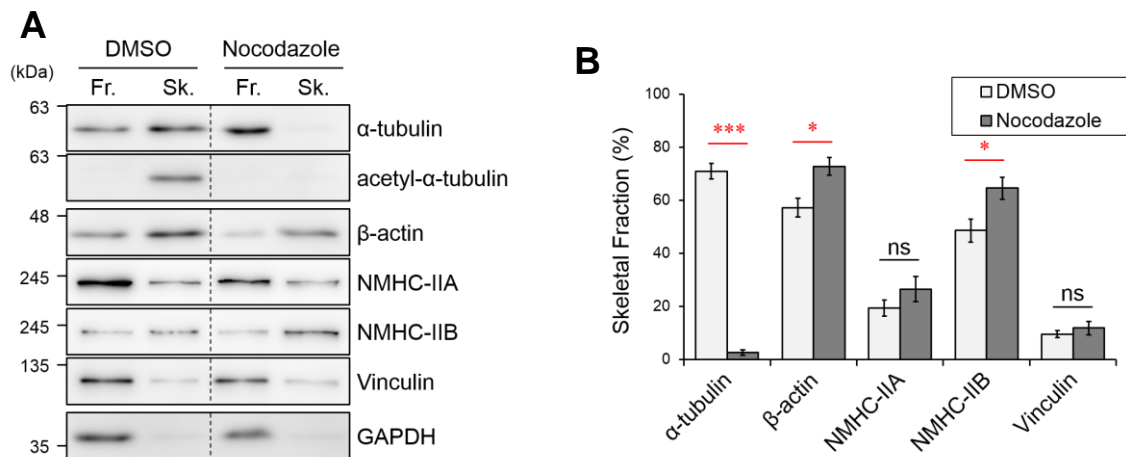


**Fig. 21. Immunoblotting for analysis of the effects of nocodazole-induced MT depolymerization on actin cytoskeletons by SERCYF-method.**

(A) Immunoblots of fractionated proteins prepared by SERCYF-method. The cells were treated in the same way as in Fig. 19. (B) The percentages of cytoskeletal fractions, calculated from (A). Data represent mean  $\pm$  SEM from five independent experiments. \*,  $p < 0.05$ ; \*\*\*,  $p < 0.001$ ; ns, non-significant, calculated by unpaired Student's  $t$ -test.

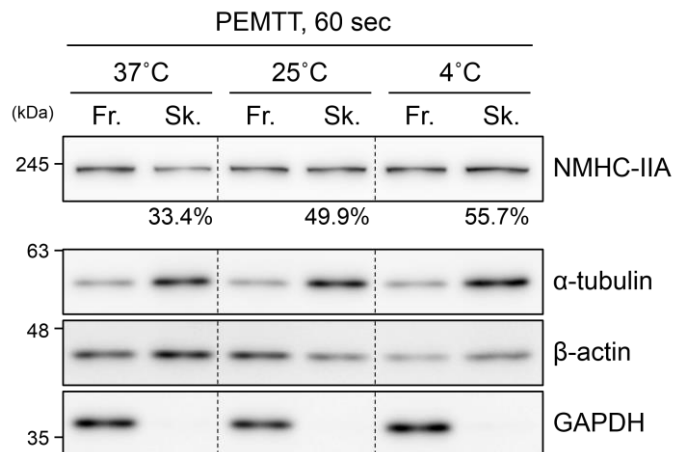


**Fig. 22. Immunoblotting for analysis of the impact of temperature on fractionation efficiency of SERCYF-method.**

Immunoblots of fractionated proteins prepared with PEMTT-buffer. Pre-permeabilization was performed for 60 sec at the indicated temperature. The values under the NMHC-IIA panel represent the percentages of cytoskeletal NMHC-IIA in each experiment.

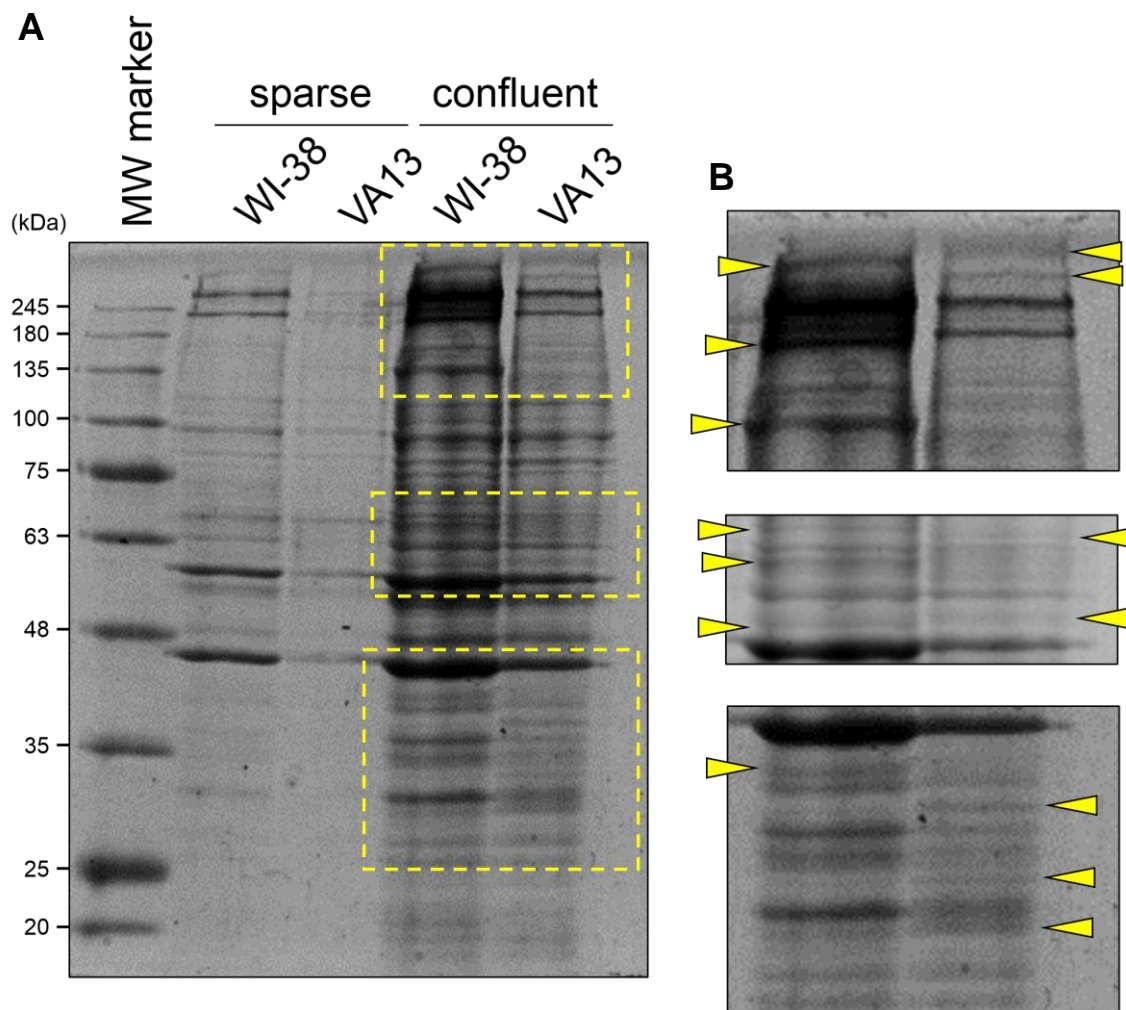


**Fig. 23. CBB-staining of a polyacrylamide gel for analysis of the profiling of cytoskeleton-associated proteins between different cell types by SERCYF-method.**

(A) An image of a polyacrylamide gel stained with CBB after SDS-PAGE of cytoskeletal fractions extracted from WI-38 (normal fibroblasts) cells and VA13 (immortalized cells derived from WI-38 cells) at different culture densities. (B) Enlarged images of indicated regions in (A). Arrowheads indicate cell type-specific bands. This experiment was performed by Yuki Tagawa, M. S.

## ***Chapter 3.***

### **Functional analysis of nonmuscle myosin IIA and IIB in MT the regulation of microtubule dynamics**

---

#### **3.1. Abstract**

Nonmuscle myosin II (NMII) is one of the regulators of actin–microtubule (MT) crosstalk. NMII-exerted cellular contractility was reported to decrease MT growth speed; however, the mechanism whereby NMII regulates MT dynamics remains unclear. Here I show that both of well-characterized NMII isoforms, NMIIA and NMIIB, are involved in the regulation of MT dynamics, but the underlying mechanisms are different. NMIIA-depleted U-2 OS cells, which do not exert cellular contractility, exhibited fast MT growth, supporting the previous reports. In these cells, expression levels of some mammalian diaphanous-related formins (mDia) were reduced. Consistently, mDia1-depletion accelerated MT growth, similar to NMIIA-depletion, suggesting that NMIIA slows down MT growth by stabilizing the expression of mDia proteins. NMIIB-depleted cells also exhibited fast MT growth, even though these cells can exert cellular contractility at a control level, suggesting that NMIIB slows down MT growth in a manner independent of cellular contractility. Destabilization of actin filaments in NMIIB-depleted cells, which was indicated by cytoskeletal fractionation and FRAP analyses, would be one of the causes of MT growth acceleration. Collectively, these results suggest that NMIIA and NMIIB differently slow down MT growth and that NMIIB regulates MT growth via contractility-independent novel mechanism.

#### **3.2. Introduction**

Actin and MT cytoskeletons intrinsically undergo dynamic polymerization and depolymerization cycles, and in cells, each cytoskeletal dynamics is additionally regulated by numerous factors. Such cytoskeletal regulators include the other cytoskeletons; actin cytoskeletons regulate MT dynamics and stability; similarly, MTs regulate actin dynamics and stability (Huber et al., 2015; Rodriguez et al., 2003). The crosstalk between actin and MT cytoskeletons plays important roles in fundamental cellular functions such as cell migration and cell shape determination. Not only physical interaction between different cytoskeletons, indirect crosstalk pathways are also important in these functions. For example, actin-myosin contractile machinery controls morphogenesis of endothelial cells and nerve cells through the regulation of MT dynamic instability (D'Angelo et al., 2017; Dent and Gertler, 2003; Myers et al., 2011; Rösner et al., 2007). In the process of endothelial branching morphogenesis, NMII generates contractile force at specific regions of the cell, which makes MTs dynamically stable; MTs at contracted regions

exhibit slow but long-lived growth (D'Angelo et al., 2017; Myers et al., 2011).

However, the molecular mechanism of NMII-dependent MT dynamics regulation has been unclear. To elucidate the underlying mechanism in mammalian cells, we should carry out experiments with distinguishing NMII isoforms, NMIIA, NMIIIB, and NMIIIC (Aguilar-Cuenca et al., 2014; Shutova and Svitkina, 2018; Vicente-Manzanares et al., 2009). Among these, NMIIA and NMIIIB are especially important at individual level, as indicated by the embryonic lethality of mice lacking gene that encodes NMIIA heavy chain (NMHC-IIA) (Conti et al., 2004; Wang et al., 2010) or NMHC-IIB (Tullio et al., 1997). As these mice show different symptoms and die at different stages of development, NMIIA and NMIIIB are suggested to have non-redundant functions that cannot be compensated by the other isoform. Functional differences of NMIIA and NMIIIB are being revealed at single cell level. With respect to the role in exertion of contractility to the cell, it has been reported that NMIIA is indispensable, whereas NMIIIB is not largely required (Jorrisch et al., 2013; Shutova et al., 2017; Thomas et al., 2015). Importantly, it has also been reported that NMIIA-exerted cellular contractility is inversely correlated with MT acetylation, which is coordinated by NMII inactivator, MYPT1/myosin-binding subunit of myosin phosphatase, and MT deacetylator, HDAC6 (Even-Ram et al., 2007; Joo and Yamada, 2014; Joo and Yamada, 2016). Such actomyosin–MT coordination controls extracellular matrix rearrangement and is required for proper morphogenesis of submandibular glands. NMIIA thus plays an important role in MT regulation in the context of cellular contractility exertion; however, whether NMIIIB has any functions in the MT-regulatory mechanism has been unclear. Considering the fact that NMIIIB is also required for proper embryonic development similar to (but different from) NMIIA, it is possible that NMIIIB also participates in MT regulation. But at the same time, it seems that NMIIIB is not required for the exertion of cellular contractility (Jorrisch et al., 2013; Shutova et al., 2017; Thomas et al., 2015)—Does not NMIIIB regulate MT dynamics?

The purpose of the present study was to explore the function of each NMII isoform on MT dynamics, and in turn, to elucidate the underlying mechanisms of NMII isoform-dependent MT dynamics regulation. To accomplish this goal, I examined the dynamics of EGFP tagged-end-binding protein 1 (EB1-EGFP), which accumulates at growing MT plus-ends (Mimori et al., 2000; Skube et al., 2010), in NMII isoform-depleted cells; subsequently, I performed comprehensive analysis of their behaviors by using plusTip Tracker software package (Applegate et al., 2011; Matov et al., 2010) to determine MT growth parameters. My results showed that, as well as NMIIA, NMIIIB also has suppressive effect on MT growth, but in a manner independent of cellular contractility. Furthermore, NMIIIB appear to regulate MT growth via novel mechanism that is different from NMIIA-dependent mechanism.

### **3.3. Results**

#### **3.3.1. NMIIA, but not NMIIB, is critical for exertion of cellular contractility in U-2 OS osteosarcoma cells**

First of all, I characterized NMIIA and NMIIB localizations in U-2 OS cells and compared the effects of small interfering RNA (siRNA)-mediated depletion of each isoform on actin and MT cytoskeletons (Fig. 24, 25). Immunofluorescence microscopy revealed that subcellular localization of each NMII isoform was similar to that of other cell types (Kuragano et al., 2018a; Kuragano et al., 2018b; Maupin et al., 1994; Saitoh et al., 2001; Shutova et al., 2017); NMIIA was localized to overall stress fibers (SFs) throughout the cell and also diffusely distributed in cytoplasm, whereas NMIIB was strongly localized to some specific SFs including peripheral bundles and central regions of arc-like fibers (Fig. 24). Transfection of siRNAs designed to target each NMII heavy chain effectively depleted corresponding NMII isoforms (Fig. 25). Notably, total NMHCII signal was significantly decreased by the depletion of NMIIA but not by the depletion of NMIIB, indicating that the expression level of NMIIA was much higher than that of NMIIB in U-2 OS cells. Depletion of NMIIA significantly decreased the number of SFs, and some irregularly thick SFs which incorporate the residual NMIIA and most of NMIIB were formed. Depletion of NMIIB did not show obvious alteration in SF formation but showed thick lamellipodial protrusions (Fig. 24: arrows). These results indicate that NMIIA is required for the formation of proper SFs, whereas NMIIB is not largely involved in SF formation; however, considering the emergence of lamellipodial protrusions by NMIIB-depletion, it may regulate actin dynamics, which could have been overlooked because this phenotype is unremarkable compared to the severe phenotype of NMIIA-depleted cells. In contrast to the large effect on actin cytoskeletons, depletion of either NMIIA or NMIIB resulted in no obvious change in overall MT distribution or  $\alpha$ -tubulin expression level (Fig. 24, 25).

To assess the contributions of each NMII isoform to cellular contractility in my cell line, I performed a collagen gel contraction assay. As shown in Fig. 26, cells plated on top of a collagen gel can slightly, but significantly, contract it (compare “cell-free” and “ctrl.” panels in Fig. 26A). While control and NMIIB-depleted cells equally contracted the gels, NMIIA-depleted cells did not contract the gel at all (Fig. 26A). Size measurement and statistical analysis also revealed that the activity to contract gels was significantly decreased by NMIIA-depletion (Fig. 26B). This assay suggests that, at least at endogenous expression levels, NMIIA, but not NMIIB, contributes to exertion of cellular contractility in U-2 OS cells, as observed in other cell types (Jorrisch et al., 2013; Shutova et al., 2017; Thomas et al., 2015).

#### **3.3.2. Both NMIIA and NMIIB contribute to suppression of MT growth**

I next analyzed MT plus-end dynamics in NMII-depleted cells by time-lapse confocal imaging of

EB1-EGFP. I adopted EB1, but not tubulin, for imaging because of the advantage of its comprehensiveness; we can detect all MT growth episodes even in cell center where MT density is too high to directly observe their behaviors. Detection of EB1 comets, estimation of comet trajectories, and post-processing analysis (determination of growth speed, duration, and length of each trajectory) of EB1 behaviors were automatically performed by plusTipTracker software, a MATLAB-based program developed by Danuser's laboratory (Applegate et al., 2011; Matov et al., 2010).

By using plusTipTracker, I detected approximately 1000 trajectories per cell in my experimental procedure (for 60 sec at 1-sec intervals). From the image sequences, I obtained mean MT growth speed, mean MT growth lifetime, and mean MT growth length of each cell, and then I compared these parameters of NMII-depleted cells with those of control cells (Fig. 27). The right panels of Fig. 26A show EB1 comet trajectories with colors according to the speed of each trajectory. NMIIA-depleted cells, which do not exert cellular contractility, showed significantly faster MT growth, compared to control cells (Fig. 27A, B). This result is consistent with the result of blebbistatin treatment in the previous study where the loss of cellular contractility accelerated MT growth (Myers et al., 2011). The effect of NMIIA-depletion on MT growth speed spanned the whole cell region; from the center to the periphery (Fig. 27A). Unexpectedly, NMIIB-depleted cells, which do exert cellular contractility at control levels, also showed significantly fast MT growth (Fig. 27A, B). This effect also spanned the whole cell region, despite the fact that NMIIB was not distributed in the peripheral region of lamella (Fig. 27A), implying that certain downstream factors, rather than the NMIIB molecule per se, regulate MT dynamics. In both groups, MT growth lifetime was not affected, and MT growth length was increased (Fig. 27C, D). Together, these results indicate that both NMIIA and NMIIB have suppressive effects on MT growth, and that, at least in the case of NMIIB, this effect rises in a manner independent of cellular contractility.

### **3.3.3. Both NMIIA and NMIIB are required for maintenance of actin and MT cytoskeletal organization**

Based on the finding that actin cytoskeletal architecture and possibly its dynamics were altered by NMIIA- and NMIIB-depletion, respectively (Fig. 24), and on the report showing actin polymerization frequently initiate from the tip of MT plus-end (Henty-Ridilla et al., 2016), I hypothesized that changes in MT growth speed in NMII-depleted cells are resulted from the altered actin stability or dynamics. To verify this hypothesis, I need to check whether actin stability or dynamics are affected by NMII-depletion. Although inhibition of NMII activity with blebbistatin is known to affect actin dynamics (Ponti et al., 2004; Yamashiro et al., 2018), little is known about the role of each NMII isoform on actin properties.

At first, I analyzed the cytoskeletal organization states of NMII-depleted cells by semi-

retentive cytoskeletal fractionation (SERCYF)—a Triton X-100-based method that enables simultaneous and semi-retentive fractionation of both actin and MT cytoskeletons (Sato et al., 2017), which is described in Chapter 2. Immunofluorescence microscopy revealed that both actin and MT networks were not largely disrupted even after the treatment of permeabilization buffer, confirming that this method was suitable for cytoskeletal fractionation (Fig. 28). For biochemical analysis of cytoskeletal organization, I separated cellular components into cytoplasmic and cytoskeletal (including nuclear) fractions, and then analyzed the amount of  $\beta$ -actin present in each fraction by immunoblotting (Fig. 29A). I found that depletion of either NMIIA or NMIIB significantly increased the percentage of cytoplasmic  $\beta$ -actin (Fig. 29B), suggesting that both NMIIA and NMIIB contribute to the formation of specific actin cytoskeletal architectures. Alternatively, they could regulate actin dynamic properties: promotion of polymerization and/or suppression of depolymerization. At the same time, I analyzed  $\alpha$ -tubulin distribution by SERCYF and found that NMII-depletion also tended to increase the percentage of cytoplasmic  $\alpha$ -tubulin (Fig. 29C). Because the concentration of free tubulin dimer is critical for MT growth speed, the increase in cytoplasmic  $\alpha$ -tubulin could reflect the accelerated MT growth in NMII-depleted cells.

### 3.3.4. NMIIA and NMIIB differently regulate actin organization and dynamics

To further investigate the effects of NMII-depletion on actin cytoskeletons, I analyzed their dynamics by fluorescence recovery after photobleaching (FRAP) experiments. Among various actin cytoskeletal structures, I selected a lamella, thin and flat region formed behind the leading edge, as a region of interest (ROI); because the actin cytoskeletal structures in lamellae contain both NMIIA and NMIIB, and many MTs also develop there (Fig. 24). After photobleaching of mCherry-actin by laser scanning, the process of fluorescence recovery was measured (Fig. 30A). To quantify the actin dynamics, each recovery data was fitted to an exponential curve provided by a molecular association–dissociation model. Statistical analysis indicated that a two-component model provided the best fit to the data (Fig. 30A–C); all of  $\chi^2$ -test, Akaike's information criteria, and *F*-test showed the validity of the two-component model. The half recovery time of the faster component ( $t_{\text{half1}}$ ) was  $3.1 \pm 0.7$  sec, and that of the slower component ( $t_{\text{half2}}$ ) was  $26.1 \pm 4.8$  sec. To characterize these components, I next analyzed the dynamics of mCherry-actin G13R, an unpolymerizable actin mutant (Posern et al., 2002). The mutated actin molecules freely diffuse in the cytoplasm. Because of this characteristic, the fluorescence recovery of this mutant was quite rapid; the half recovery time was  $3.6 \pm 0.2$  sec (Fig. 30D). This value was similar to that of  $t_{\text{half1}}$  of the wildtype actin, suggesting that the faster component of mCherry-actin represents free diffusion in the cytoplasm. On the other hand, the slower component could represent dynamic actin turnover—polymerization and depolymerization. This idea is supported by the previous report showing  $26.1 \pm 0.9$  sec as a turnover rate of lamellar actin networks in PtK1 epithelial cells by using total internal reflection-FRAP (Gupton et al., 2007).

Hereafter, I focus on and discuss only the slower component because the recovery of the faster component (free diffusion) was too fast to analyze precisely.

I next performed FRAP experiments in NMII-depleted cells. Fig. 30E and F show the representatives of recovery processes of mCherry-actin fluorescence in NMII-depleted cell. The unrecovered fraction in the graphs represents molecules which bind too strongly to specific structures to dissociate from the structures during the experimental periods (Fig. 30F). In the case of my experiment, the unrecovered fraction would reflect the presence of stable actin cytoskeletal structures, such as stress fibers (transverse arcs in the lamella). In control cells, approximately one fourth of lamellar actin molecules were classified as such a stable fraction. While NMIIB-depleted cells formed the stable actin cytoskeletal structures similar to control cells, NMIIA-depleted cells did not (Fig. 30G). These results suggest that NMIIA is required for the formation of stable actin networks in the lamella, but NMIIB is not. The importance of NMIIA for the formation of transverse arcs is consistent with our previous work (Kuragano et al., 2018b). Interestingly, I also found that the effects of depletion on actin turnover rate were different between NMIIA and NMIIB; only NMIIB-depletion significantly decreased  $t_{\text{half2}}$  (Fig. 30H). Collectively, FRAP experiments suggested that actin cytoskeletal dynamics are regulated by NMII, and importantly, these effects are isoform specific—NMIIA is important for the formation of lamellar actin networks, but does not regulate actin turnover; NMIIB is not important for the formation of lamellar actin networks, but does suppress actin turnover.

### **3.3.5. Fast actin dissociation is one of the cause of accelerated MT growth in NMIIB-depleted cells**

The most important interest is whether altered actin dynamics by NMII-depletion affects MT dynamics. To address this possibility, I next treated siRNA-transfected cells with jasplakinolide, an actin depolymerization inhibitor, to suppress actin turnover and assessed its effect on MT growth. At 10 nM, at which overall cell shape and actin organization were not disrupted (Fig. 31), jasplakinolide did not affect MT growth in control or NMIIA-depleted cells (Fig. 32A, B). Interestingly, in NMIIB-depleted cells, which showed accelerated actin turnover, jasplakinolide moderately but significantly decreased MT growth speed. This effect was partial; compared to control cells, NMIIB-depleted cells showed still faster MT growth even in the presence of jasplakinolide. These results suggest that fast actin turnover, and more specifically, actin depolymerization, is one of the factors that accelerate MT growth and that additional factors are involved in MT regulation downstream of NMIIB.

To support the idea that actin depolymerization affects MT growth, I next treated cells with latrunculin A to induce actin depolymerization and assessed its effect on MT growth. In the presence of 10 nM latrunculin A, an actin polymerization inhibitor, cells showed thick lamellipodial protrusions, as observed in NMIIB-depleted cells (Fig. 33). In addition, similar to

NMIIIB-depleted cells, latrunculin A-treated cells showed faster MT growth (Fig. 34). After all, fast actin depolymerization should be one of the causes of accelerated MT growth observed in NMIIIB-depleted cells.

### **3.3.6. NMIIA contributes to expression of mDia proteins**

My next question is what molecules connect actin dynamics to MT dynamics. Here, I focused on a member of diaphanous-related formins (DRFs), mDia. Although formin family proteins are widely recognized as promoters of actin nucleation and polymerization, they also function as MT stabilizers by directly or indirectly binding to MTs (Bartolini and Gundersen, 2010; Chesarone et al., 2010; Zuidschewoude et al., 2018). In vitro experiments showed that direct binding of mDia2 decreased MT growth and shrinkage speed (Bartolini et al., 2008).

I hypothesized that the expression level or activity of mDia proteins are altered by NMII-depletion, which consequently affects MT dynamics. To verify this hypothesis, I examined the expression levels of three mDia isoforms, mDia1, mDia2, and mDia3, by immunoblotting. Interestingly, protein amounts of all mDia isoforms were significantly decreased by NMIIA-depletion, but NMIIIB-depletion did not affect their expression significantly (Fig. 35). Consistent with this result, immunofluorescence microscopy also showed that NMIIA-depleted cells exhibited significantly weaker mDia1 signals than control cells (Fig. 36). To investigate the cause of reduced mDia expression in NMIIA-depleted cells, I sought to determine whether cellular contractility is involved in the mechanism. For this purpose, I treated cells with 20  $\mu$ M ( $\pm$ )-blebbistatin for 2 days to inhibit NMII-dependent contractile force generation and analyzed mDia1 expression level by immunofluorescence microscopy. I found that in the presence of blebbistatin, the amount of mDia1 was partially decreased (Fig. 37); however, the extent of the decrease was small compared to NMIIA-depletion. These results imply that NMIIA-exerted cellular contractility weakly contributes to stabilize mDia1 expression and that the presence per se of NMIIA exhibits an additional contribution to that.

Based on the fact that mDia proteins stabilize MTs and slow down their growth (Bartolini et al., 2008; Bartolini et al., 2016), I hypothesized that the decrease in the amount of mDia proteins is the cause of fast MT growth in NMIIA-depleted cells. Here I performed a single depletion of mDia1 because transfection of siRNA targeting mDia2 induced irregularly rounded cell shape and cell death by unknown causes (data not shown). mDia1-depleted cells exhibited nearly normal cytoskeletal distribution, except that these cells tended to exhibit thick lamellipodial protrusion (Fig. 38). mDia1-depletion did not affect distribution or expression of NMII isoforms (Fig. 39, 40). I next analyzed the effect of mDia1-depletion on MT growth. Consistent with the mDia's role in MT stabilization, mDia1-depletion significantly accelerated MT growth (Fig. 41). These results suggest that mDia1 is a candidate that connects NMIIA-exerted cellular contractility and/or the presence per se of NMIIA to MT growth dynamics.

### **3.4. Discussion**

NMII-exerted cellular contractility has been considered as a suppressor of MT dynamic instability (D'Angelo et al., 2017; Myers et al., 2011); however, the mechanism has not been clarified. The purposes of the present study were to explore the functions of NMIIA and NMIIB on MT dynamics and to elucidate how they regulate it. For these purposes, I used U-2 OS cells and found that NMIIA, but not NMIIB, was required for exertion of cellular contractility. Notably, NMIIA-depleted cells and NMIIB-depleted cells similarly exhibited fast MT growth, in spite of the significantly different contraction states between these two groups (Fig. 24-27). To explore the cause of MT growth acceleration, I focused on actin cytoskeletons and found that NMIIA and NMIIB differently regulated actin organization and dynamics (Fig. 28-30). Importantly, the enhanced actin dissociation observed in NMIIB-depleted cells appeared to be linked with MT growth acceleration (Fig. 31-34). Different from NMIIB-depleted cells, NMIIA-depleted cells expressed less mDia proteins, which have MT stabilizing activity, and this phenomenon might be partially caused by the loss of cellular contractility (Fig. 35-37). Consistent with the stabilizing effect of mDia1, its depletion accelerated MT growth without affecting overall cytoskeletal organizations (Fig. 38-41). Collectively, these results suggest that both NMIIA and NMIIB have a function to suppress MT growth, but the regulatory mechanisms are different—NMIIA exerts cellular contractility to stabilize expression of mDia proteins that interact and suppress MT dynamics; NMIIB suppresses actin dissociation that induces acceleration of MT growth in a manner independent of cellular contractility.

#### **3.4.1. NMIIB-dependent MT regulation**

The most important point of this study is the finding that NMIIB is involved in MT dynamics regulation. Although NMII has been considered to control MT dynamics and stability by generating contractile force (D'Angelo et al., 2017; Even-Ram et al., 2007; Joo and Yamada, 2014; Joo and Yamada, 2016; Myers et al., 2011), I demonstrated that NMIIB-depleted cells exhibited significantly fast MT growth in spite of their normal cellular contractility (Fig. 26, 27). Interestingly, the extent of acceleration of MT growth observed in NMIIB-depleted cells was comparable to that observed in NMIIA-depleted cells.

To discuss this unexpected result, I first focus on the fundamental properties and functions of NMIIB. Compared to NMIIA, NMIIB exhibits higher duty ratio (the fraction of time for strong binding states with actin filaments during ATPase cycles) (Kovács et al., 2003; Rosenfeld et al., 2003; Wang et al., 2003) and higher assembling ability to form bipolar filaments (Murakami et al., 1995; Nakasawa et al., 2005; Ronen and Ravid, 2009). Based on such unique properties, NMIIB is suggested to function as an “actin crosslinker”, contrasting to NMIIA’s function as an “actin translocator” because of its higher motor activity (Heissler and Manstein, 2013; Vicente-Manzanares et al., 2009; Wang et al., 2003). The higher assembling ability of NMIIB was also

shown my fractionation experiment; the percentage of cytoskeletal fraction of NMHC-IIB was much higher than that of NMHC-IIA (Fig. 29). Combining with the result that the expression level of NMIIB was much lower than that of NMIIA (Fig.25), it is possible that there is only a small difference between the absolute amounts of NMIIA and NMIIB which are incorporated into functional actomyosin filaments in U-2 OS cells. Functioning as an actin crosslinker, NMIIB may structurally stabilize actin filaments. Interestingly, binding of myosin II induces cooperative conformational changes in actin filaments (Miki et al., 1982; Tokuraku et al., 2009), which inhibits binding of cofilin to the filaments in an allosteric manner (Ngo et al., 2016). Because of the high duty ratio, NMIIB binds to actin filaments for a relatively long time, which could efficiently protect actin filaments from sever/depolymerization by cofilin. Consistent with the actin stabilizing ability of NMIIB, my analyses demonstrated that free (cytoplasmic) fraction of actin and the rate of actin dissociation were significantly increased in NMIIB-depleted cells (Fig. 29, 30). Frequent lamellipodial protrusions observed in NMIIB-depleted cells (Fig. 24) or low-dose latrunculin A-treated cells (Fig. 33) would develop by using the increased actin monomers in the cytoplasm (Vitriol et al., 2015).

For the exploration of the mechanism of NMIIB-dependent MT regulation, I used jasplakinolide to inhibit actin dissociation that was enhanced by NMIIB-depletion. This inhibitor significantly suppressed the effect of NMIIB-depletion on MT growth speed (Fig. 32), implying that actin depolymerization reactions and/or an increase in cytoplasmic actin concentration have inhibitory effects on MT growth. Interestingly, formin mDia1 senses an increase in actin concentration; when monomeric actin is increased in the cytoplasm by the addition of low-dose latrunculin B or by the release of cellular tension, the number of mDia1 exhibiting processive movement, which represents actin polymerization, is increased (Higashida et al., 2008; Higashida et al., 2013). In addition, most formins function as MT regulators; they directly and indirectly bind to MTs, which aligns MTs with actin filaments, promote MT posttranslational modifications, and structurally and dynamically stabilize MTs (Bartolini and Gundersen, 2010; Bartolini et al., 2008; Chesarone et al., 2010; Thurston et al., 2012; Wen et al., 2004; Zuidschewoude et al., 2018). From these reports, I hypothesized that actin monomers increased by NMIIB-depletion bind to MT-bound mDia1 to prioritize it to promote actin polymerization, thereby the mDia1-detached MTs become unstable and exhibit fast growth. To validate this hypothesis, I analyzed the expression levels of mDia proteins. Although the effect of NMIIB-depletion on the expression of mDia1, mDia2, and mDia3 were small, their expression balance seemed to be altered (Fig.35). Because the activation states and MT-binding states of mDia proteins could not be analyzed in the present study, I need to investigate them by using more specialized techniques, such as a single-molecule speckle microscopy (SiMS) for tracking of each mDia movement (Higashida et al., 2004; Higashida et al., 2008; Higashida et al., 2013; Yamashiro et al., 2014), and a proximity ligation assay (PLA) for detection of MT-bound mDia proteins (Bartolini et al., 2016; Jurewicz

et al., 2018; Söderberg et al., 2006), in the future. Considering the similar phenotypes of NMIIB-depleted cells and mDia1-depleted cells that exhibited frequent lamellipodial protrusions (Fig. 38, 39), it is well possible that mDia1 is involved in the mechanism. Taken together, although there are still a few unclear aspects, this study demonstrated that NMIIB is surely involved in the MT regulatory mechanism and that this mechanism is not related to cellular contractility.

### **3.4.2. NMIIA-dependent MT regulation**

Unlike NMIIB, NMIIA was required for cellular contractility in U-2 OS cells (Fig.26). In NMIIA-depleted cells, MT growth speed was significantly increased (Fig. 27). This result is consistent with previous reports which showed that endothelial cells exhibited significantly fast MT growth under the condition where cellular contractility is low (Myers et al., 2011). Although such a relationship between cellular contractility and MT dynamics is likely to be controlled by MT depolymerizing kinesin MCAK that regionally regulates MT dynamics (D'Angelo et al., 2017), little is known about the underlying mechanism.

To test the possibility of involvement of mDia proteins in the NMII-dependent MT regulatory mechanism, I performed their immunoblotting as mentioned above. The protein amounts of all three mDia isoforms, mDia1, mDia2, and mDia3, were significantly decreased by NMIIA-depletion (Fig. 35). I then used blebbistatin to decrease cellular contractility to validate my hypothesis that cellular contractility is important for their expression or stability. Contrary to the expectation, however, the extent of the decrease in mDia1 protein level by blebbistatin treatment was smaller than that by NMIIA-depletion (Fig. 36, 37). The major difference between blebbistatin-treated cells and NMIIA-depleted cells are the presence of NMIIA molecules. Even in the presence of blebbistatin, NMIIA might have potential to maintain the stability of mDia proteins and/or their expression independent of actin translocation and consequent contractile force generation.

Considering the formin's functions on MTs, I hypothesized that the severe loss of all three mDia isoforms was the main cause of the fast MT growth observed in NMIIA-depleted cells. Unfortunately, although I had planned to perform a triple depletion of all mDia isoforms, cells transfected with mDia2-targeting siRNA alone experienced unexpected cell death. To reproduce the situation of NMIIA-depletion, I have to design siRNAs that do not improperly affect cell integrity. However, considering the result showing that a single depletion of mDia1 was enough effective to accelerate MT growth (Fig. 41), which was a comparable level with NMIIA-depletion, the significant decrease of mDia1 expression by NMIIA-depletion could be the main cause of the fast MT growth. For a better understanding, it is important to investigate the impacts of single depletions of either mDia2 or mDia3 on MT growth.

### **3.4.3. Underlying mechanisms and biological significance of NMII-MT axis**

Although this study demonstrated a portion of the NMII-dependent MT regulatory mechanisms, there are two important points I should address: proteins that connect NMII with MT dynamics, and biological significance of this axis. As discussed above, mDia1 (and possibly, mDia2 and mDia3) could be involved in the mechanism of this axis. Additionally, CLIP-170, a member of EB1-binding partners, has been reported to interact with mDia1 to accelerate actin polymerization (Henty-Ridilla et al., 2016). Because CLIP-170 accelerates MT growth by recruiting polymerization-competent tubulin dimers (Arnal et al., 2004; Folker et al., 2005; Nishimura et al., 2012), it is interesting whether the mDia1–CLIP-170 interaction affects MT dynamics, as well as actin dynamics, under the control of NMII. With respect to biological significance, the NMII–MT axis has been considered to be important for morphogenesis of endothelial cells and nerve cells (D'Angelo et al., 2017; Dent and Gertler, 2003; Myers et al., 2011; Rösner et al., 2007). I will assess whether the phenotypes in cell shape observed in NMII-depleted cells can be linked with their changes in MT dynamics. In addition, since there are many reports demonstrating the importance of NMII in cell migration (Heissler and Manstein, 2013; Vicente-Manzanares et al., 2009), I should examine the involvement of MT dynamics in such migration defects.

In addition to NMIIA and NMIIB, mammalian cells can express NMIIIC (Golomb et al., 2004). Compared to NMIIA and NMIIB, NMIIIC has not studied well. Hence, whether NMIIIC regulates MT dynamics has been unclear. Because NMIIIC expression level is higher in cancer cells than normal cells (Jana et al., 2006), comprehensive knowledge of the roles of NMII isoforms (including NMIIIC) in MT dynamics regulation could contribute to revealing the mechanism of specific migration of cancer cells, which might lead to therapy for cancer metastasis.

### **3.5. Conclusion**

In this chapter, to elucidate the functions of NMII in MT dynamics regulation, I analyzed the effects of NMII isoform-specific depletion on the structures and dynamics of MT and actin cytoskeletons (Fig. 42). I found that NMIIA and NMIIB differently regulate MT dynamics—NMIIA slows down MT growth through the stabilization of mDia expression; NMIIB slows down MT growth through the suppression of actin dissociation (Fig. 43). Thus, although both isoforms downregulate MT growth, the underlying mechanisms are likely to be different. For a better understanding, it is required to answer the question of which molecules link each NMII isoform to MT dynamics.

## **3.6. Experimental procedures**

### **3.6.1. Cell culture**

U-2 OS cells and U-2 OS cells stably expressing EB1-EGFP were maintained in McCoy's 5A (modified) medium (GIBCO/Life Technologies, Carlsbad, CA, USA) supplemented with 10% fetal bovine serum (FBS) (BioSource/Life Technologies), 50 U/mL penicillin and 50 µg/mL streptomycin (GIBCO). All cells were cultured at 37°C in humidified air containing 5% CO<sub>2</sub>. Where indicated, the cells were treated with jasplakinolide (Merck Millipore, Burlington, MA, USA), latrunculinA (Merck Millipore), or blebbistatin (Merck Millipore) at indicated conditions.

### **3.6.2. Antibodies**

Antibodies used in this study is listed on Table 2.

### **3.6.3. siRNA transfection**

siRNAs targeting human NMHC-IIA gene (*MYH9*: GGCCAAAGAGAACGAGAAGUU, as sense strand), human NMHC-IIB gene (*MYH10*: GGAUCGCUACUAUUCAGGAUU), and control (GCGCGCUUUGUAGGAUUCGUU) were purchased from Thermo Scientific Dharmacon (Waltham, MA). siRNA targeting pig mDia1 gene (*DAIPH1*: CAGAAUCUCUCAAUCUUUCUGGGUU) was kindly gifted from Dr. Keiju Kamijo (Tohoku Medical and Pharmaceutical University, Sendai, Japan). Note that although this mDia1 siRNA was originally designed to deplete pig mDia1, it clearly depleted human mDia1 as indicated in Fig. 39 (there is only one mismatch: substitution from the underlined cytosine to uracil in the sequence, for the perfect match with human DIAPH1). A total of  $2 \times 10^4$  cells cultured in a 24 well-plate with antibiotics-free medium were transfected with 20 pmol of each siRNA with Lipofectamine RNAiMAX Transfection Reagent (Invitrogen, Carlsbad, CA, USA), according to the manufacturer's instruction. Three days after transfection, cells were subjected to analyze by immunofluorescence or immunoblotting as described below.

### **3.6.4. Plasmid transfection**

A plasmid encoding mCherry-actin was kindly gifted from Dr. Keiju Kamijo. siRNA-transfected cells cultured in a 24 well-plate with antibiotics-free medium for one day were further transfected with 1 µg of each plasmid with Xfect Transfection Reagent (Takara Bio USA, Mountain View, CA, USA), according to the manufacturer's instruction. Consequent analyses were performed two days after transfection.

### **3.6.5. Collagen gel contraction assay**

Cold Cellmatrix Type I-A collagen solution (Nitta Gelatin, Osaka, Japan) was sufficiently mixed

with cold 10×condensed medium (Nitta Gelatin) on ice, followed by the addition of cold reconstruction buffer [50 mM NaOH, 260 mM NaHCO<sub>3</sub>, 200 mM HEPES]. The collagen solution mix was dispensed into the bottom of 24 well-plates and incubated at 37°C for gelation. siRNA-transfected cells were plated on the gel to allow spreading and proliferating on the collagen gels. At the next day of plating, the gels were peeled off from the bottom of the plate by using a micro needle. The cells were further cultured on the floating gels for additional one day. If these cells generate contractile force, the gels are contracted and become smaller. Images of the gels were captured from top-down view by using LAS-3000 (Fujifilm, Tokyo, Japan). Image processing and size measurement were performed using ImageJ software (NIH, Bethesda, MD, USA).

### **3.6.6. Immunofluorescence microscopy**

Fixation and permeabilization steps, that is, formaldehyde-Triton method or methanol method, depended on each experiment (see each figure legend). For the methanol method, cells cultured on fibronectin (10 µg/mL; Roche Diagnostics, Basel, Switzerland) -coated coverslips (Matsunami, Kishiwada, Japan) were fixed and permeabilized with cold methanol for 5 min at -20°C. After being washed with cold PBS three times (at least 5 min per each wash), the coverslips were incubated with blocking buffer (3% BSA in PBS) for 15 min and incubated with primary antibodies and corresponding secondary antibodies in blocking buffer sequentially. Each incubation step was performed for 1 hour at room temperature. After being washed with PBS three times, the coverslips were rinsed with deionized water and mounted in DABCO to prevent photo-bleaching. For formaldehyde-Triton method, cells on fibronectin-coated coverslips were fixed with 3.7% formaldehyde in PBS for 15 min and permeabilized with 0.1% Triton X-100 in PBS for 10 min. The rest steps were same as that of methanol method. Antibodies used for immunofluorescence are listed in Table 2, and fluorescent-labeled phalloidin reagents used for actin filament staining were as follows: Alexa Fluor 350-labeled phalloidin (1:300; Molecular Probes, Eugene, OR, USA), FITC-labeled phalloidin (1:500; SIGMA-Aldrich, St. Louis, MO, USA), TRITC-labeled phalloidin (1:3000; SIGMA-Aldrich). Immunofluorescence images were obtained using a fluorescence microscope (BX50WI; Olympus, Tokyo, Japan), equipped with a single chip color CCD camera (DP70; Olympus) and an objective lens (UPlanApo 60×/0.90 NA; Olympus). Image processing and quantification of fluorescence intensity were performed using ImageJ software.

### **3.6.7. Confocal time-lapse imaging of EB1-EGFP**

U-2 OS cells stably expressing EB1-EGFP were plated and cultured on fibronectin-coated glass-bottom dishes (Matsunami, or IWAKI, ASAHI GLASS, Tokyo, Japan) in McCoy's 5A (modified) medium supplemented with 10% FBS. At the day of imaging, culture medium was exchanged to DMEM/F12 (1:1) (GIBCO/Life Technologies) supplemented with 10% FBS, and cells were

maintained at 37°C in humidified air containing 5% CO<sub>2</sub>. Time-lapse imaging was performed using an inverted microscope (Ti-E; Nikon, Tokyo, Japan) and a confocal laser microscope system (A1R; Nikon) equipped with an oil-immersion objective lens (Apo-TIRF 60×/1.49 NA; Nikon). To keep the culture condition (at 37°C in humidified air containing 5% CO<sub>2</sub>), stage incubator equipped with a feedback sensor (INUBG2H-TIZB; Tokai Hit, Fujinomiya, Japan) were used during imaging. The images were acquired for 60 sec at 1-sec intervals by using NIS-Elements AR version 5.01 (Nikon).

### **3.6.8. Analysis of MT growth dynamics with plusTip Tracker software**

MT growth dynamics was analyzed by using a plusTip Tracker software package, version 1.1.4 (Applegate et al., 2011; Matov et al., 2010), which automatically determines MT growth parameters from image sequences of fluorescently tagged-+TIP proteins such as EB1-EGFP. The algorithms of comet detection, comet tracking, and post-processing analysis has been described in the previous reports, in detail (Applegate et al., 2011; Matov et al., 2010). Parameters used for comet detection were as follows: camera bit depth, 12 bit; detection method, watershed-based method with  $\sigma_1 = 1$  and  $\sigma_2 = 4$  and  $K = 3$ . Parameters used for comet tracking were as follows: search radius range, 1–5 pixels; minimum sub-track length, 3 frames; maximum gap length, 5 frames; maximum shrinkage factor, 3; maximum forward angle, 30°; maximum backward angle, 10°; fluctuation radius, 2 pixels. For comparison of MT growth dynamics between groups (e.g. control cells vs NMIIA-depleted cells), each MT growth parameter such as speed was collected from 30 cells in each group. Spatial speed maps of color-coded comet trajectories of EB1-EGFP were also obtained by using plusTip Tracker, with a parameter of 35  $\mu\text{m}/\text{min}$  as maximum speed.

### **3.6.9. FRAP analysis of mCherry-actin**

U-2 OS cells expressing mCherry-actin were cultured by the same procedure as described in the “Confocal time-lapse imaging of EB1-EGFP” section. Photobleaching and time-lapse imaging were performed using the same microscope and equipment as EB1-EGFP imaging. A photobleaching ROI (a circle with a diameter of 5  $\mu\text{m}$ ) was created at lamellar or bulk region. mCherry fluorescence at the ROI was bleached by irradiation with a 561.5 nm laser at 100% power for 5 sec. Fluorescence images of mCherry-actin were acquired for 10 sec before the initiation of photobleaching and 90 sec after the end of photobleaching at 2-sec intervals. For the calculation of fluorescent recovery, three ROIs were created: “measure ROI” that was positioned inside of the photobleached region (a circle with a diameter of 3  $\mu\text{m}$ ), “total ROI” that covers the entire cell throughout the image series, and “background ROI” that was positioned at no cell region. Fluorescence intensities of these ROIs at each time point were measured using ImageJ software. Relative fluorescence intensity (RFI) was calculated using Eqn 1 below, where  $I_{msr}(t)$  is a time series of fluorescence intensity in the measure ROI,  $I_{tot}(t)$  is a time series of fluorescence

intensity in the total ROI, and  $I_{bgd}(t)$  is a time series of fluorescence intensity in the background ROI.

$$RFI(t) = \frac{I_{msr}(t) - I_{bgd}(t)}{I_{tot}(t) - I_{bgd}(t)} \quad (1)$$

Consequently, RFI was normalized using Eqn 2 below, where  $\mu$  is an average value of RFI before photobleaching.

$$NFI(t) = \frac{RFI(t)}{\mu} \quad (2)$$

This normalized fluorescence intensity (NFI) was plotted on a graph and performed curve-fitting to a function provided by association–dissociation models in Eqn 3 or 4 below, where  $A$  and  $B$  are magnitude of each fraction,  $k_{off}$  is a dissociation rate constant of the corresponding fraction ( $k_{off1} > k_{off2}$ ), and  $c$  is a baseline.

One-component model:

$$F(t) = A\{1 - \exp(-k_{off} \cdot t)\} + c \quad (3)$$

Two-component model:

$$F(t) = A\{1 - \exp(-k_{off1} \cdot t)\} + B\{1 - \exp(-k_{off2} \cdot t)\} + c \quad (4)$$

A three-component model was provided by a similar formula; addition of a third exponential-component to Eqn 4. A half recovery time  $t_{half}$  was further calculated using Eqn 5 below.

$$t_{half} = \frac{\ln 2}{k_{off}} \quad (5)$$

Validation of the fitting was performed in reference to a previous study (Tsutsumi et al., 2016).  $\chi^2$  values for each fitting were calculated using Eqn 6 below.

$$\chi^2 = \sum_i \left[ \frac{F(t_i) - NFI(t_i)}{\sigma(t_i)} \right]^2 \quad (6)$$

This formula represents the extent of the difference between the fitted function  $F(t)$  and the normalized experimental data  $NFI(t)$ . A  $\chi^2$  is a result of the summation of squared values of the differences between  $F(t_i)$  and  $NFI(t_i)$ , weighted by the standard deviation  $\sigma(t_i)$ , at all time points  $t_i$ . The model providing smaller  $\chi^2$  value is the more appropriate model.

Value of Akaike information criteria (AIC) were calculated using Eqn 7 below, where  $N$  is the number of data points used for each curve fitting and  $K$  is the number of parameters.

$$AIC = N \cdot \ln \left( \frac{\chi^2}{N} \right) + 2K + \frac{2K(K+1)}{N-K-1} \quad (7)$$

Similar to  $\chi^2$  values, the model providing smaller AIC value is the more appropriate model.

Finally,  $F$ -values and  $p$ -values were calculated to show the difference between the models (one-component model vs. two-component model, or two-component model vs three-component model).  $F$ -values were calculated using Eqn 8 below, where  $DF$  is the degree of freedom ( $N-K-1$ ). The values with a subscript “1” mean the corresponding values of the simpler model, and those

with a subscript “2” mean the corresponding values of the more complicated model.

$$F = \frac{(\chi_1^2 - \chi_2^2)/DF_1 - DF_2}{\chi_2^2/DF_2} \quad (8)$$

*p*-values for each *F*-value were calculated using the “FDIST” formula of Microsoft Excel 2013.

### 3.6.10. SDS-PAGE and Immunoblotting

SDS-PAGE and consequent immunoblotting were performed using standard techniques as described previously (Sato et al., 2017). Briefly, separated proteins after SDS-PAGE were transferred to an Immobilon-P PVDF membrane (Millipore Calbiochem, Billerica, MA, USA). The membrane was incubated with blocking buffer [5% skimmed milk in TBS-T (20 mM Tris, 150 mM NaCl, 0.05% Tween-20)] for 30 min. The membrane was then incubated with the primary antibodies in blocking buffer overnight at 4°C, followed by the secondary antibodies for 1 hour at 25°C. Antibodies used for immunoblotting are listed in Table 2. For immunoreaction with anti-mDia1, anti-mDia2, and anti-mDia3 antibodies, Can Get Signal Immunoreaction Enhancer Solution (TOYOBO, Osaka, Japan), instead of blocking buffer, was used. The chemiluminescent signal was produced using the Immobilon Western Chemiluminescent HRP Substrate (Millipore) and detected using a LAS-3000. The percentages of cytoskeletal fractions were calculated by densitometry using ImageJ software.

### 3.6.11. Quantification of cytoskeletal organization by SERCYF-method

SERCYF analysis was performed as described previously (Sato et al., 2017) with a minor change. Briefly, confluent cultured cells in a 24 well-plate were gently permeabilized with pre-warmed PEMTT-buffer [0.2% Triton X-100, 10 nM taxol in PIPES-EGTA-magnesium (PEM)-buffer [100 mM PIPES-NaOH (pH 6.8), 1 mM EGTA, 2 mM MgCl<sub>2</sub>]], followed by incubation at 37°C for 1 min. The permeabilized cell extract and consequent rinsing PEM were collected into a plastic tube. This cytoplasmic fraction was mixed with 2×SDS sample buffer [100 mM Tris-HCl (pH 6.8), 4% SDS, 20% glycerol, 0.2% bromophenolblue] supplemented with β-mercaptoethanol (β-ME) at a final concentration of 5%. The residual cells in the bottom of the well were lysed with 2×SDS sample buffer and collected into a plastic tube. The samples were further denatured by boiling for 3 min and analyzed by immunoblotting. For immunofluorescence microscopy of pre-permeabilized cells, cells on fibronectin-coated coverslips were permeabilized with PEMTT-buffer at 37°C for 1 min and were immediately fixed with methanol. See “Immunofluorescence microscopy” section for the rest steps. Note that “10 nM” was adopted as taxol concentration in this study because 100 nM taxol, concentration adopted for human immortalized fibroblasts used in the previous study, promoted MT bundling in U-2 OS cells (data not shown). 10 nM taxol-containing PEMTT-buffer did not promote MT bundling or MT depolymerization during the permeabilization step.

### **3.6.12. Statistical analysis**

All statistical analyses were performed using EZR (Saitama Medical Center, Jichi Medical University, Saitama, Japan), a graphical user interface for R. Each bar graph represents mean  $\pm$  standard error of mean (SEM). In dot plot graphs, each circle (or triangle) represents the value of individual cells. Also, the median (center line), 25<sup>th</sup> percentile (lower line), and 75<sup>th</sup> percentile (upper line) of each dataset were shown at the left of corresponding dot plots. In all experiments, p-values were calculated, and the extent of significance was indicated as the number of asterisks: \*,  $p < 0.05$ ; \*\*,  $p < 0.01$ ; \*\*\*,  $p < 0.001$ . The method of statistical test used in each experiment was indicated at each figure legend.

**Table 2. Antibodies used in this chapter**

Antibody	Dilution			Source
	Immunofluorescence	Immunoblotting (standard)	Immunoblotting (SERCYF)	
anti-NMHC-IIA pAb	1:5000	1:100,000-200,000	1:60,000	Sato et al., 2007
anti-NMHC-IIB pAb	1:2000	1:5000	1:500	Saitoh et al., 2001
anti- $\alpha$ -tubulin mAb (B-5-1-2)	1:5000	1:100,000	1:4000	SIGMA
anti-GAPDH mAb (6C5)	-	1:100,000	1:30,000	Millipore
anti- $\beta$ -actin mAb (AC15)	1:5000	1:100,000	1:4000	SIGMA
FITC-labeled anti- $\alpha$ -tubulin mAb (DM1A)	1:1000	-	-	Gifted from Dr. Keiju Kamijo
anti-acetyl- $\alpha$ -tubulin mAb (6-11B-1)	-	-	1:500	SIGMA
anti-mDia1 mAb	1:500	1:500	-	Gifted from Dr. Keiju Kamijo
anti-mDia2 pAb	-	1:2500	-	Gifted from Dr. Sadanori Watanabe (Watanabe et al., 2008)
anti-mDia3 pAb	-	1:500	-	Gifted from Dr. Keiju Kamijo
FITC-labeled anti-mouse IgG	1:200	-	-	Jackson ImmunoResearch Laboratories
Cy3-labeled anti-rabbit IgG	1:500	-	-	Jackson ImmunoResearch Laboratories
Cy3-labeled anti-mouse IgG	1:500	-	-	Jackson ImmunoResearch Laboratories
Alexa Fluor 488-labeled anti-rabbit IgG	1:200	-	-	Jackson ImmunoResearch Laboratories
HRP-labeled anti-rabbit IgG	-	1:10,000	1:10,000	Bio-Rad Laboratories
HRP-labeled anti-mouse IgG	-	1:10,000	1:10,000	Bio-Rad Laboratories

Abbreviations: pAb, polyclonal antibody; mAb, monoclonal antibody; FITC, fluorescein isothiocyanate; Cy3, cyanine 3; HRP, horseradish peroxidase

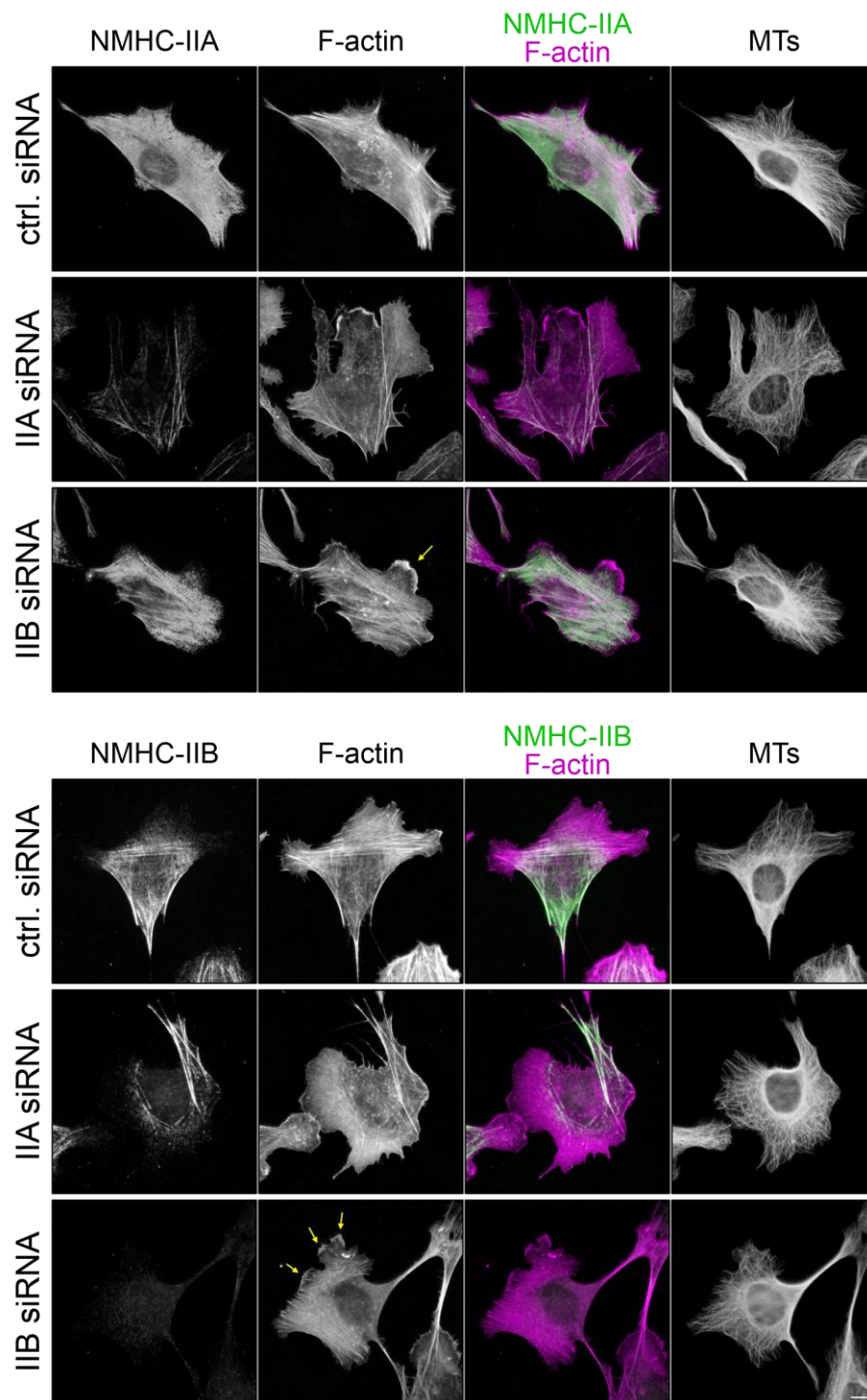


**Fig. 24. Immunofluorescence microscopy for characterization of NMII localization and analysis of the effects of their depletion by siRNA transfection.**

Immunostaining images of NMHC-IIA, NMHC-IIB, and  $\alpha$ -tubulin (MTs) in indicated siRNA-transfected cells. The cells were further stained with phalloidin to visualize F-actin. Arrows indicate thick lamellipodial protrusions in NMIIB-depleted cells. Scale bar, 10  $\mu$ m.

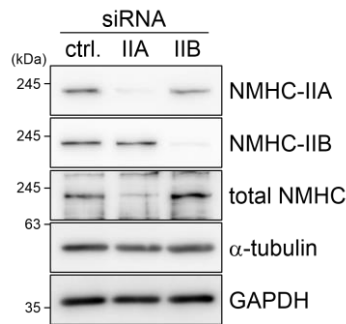


**Fig. 25. Immunoblotting for validation of siRNA-mediated depletion of NMHC-II isoforms.** Immunoblots of cytoskeletal proteins in siRNA-transfected cells. Anti-GAPDH antibody was used as a loading control.

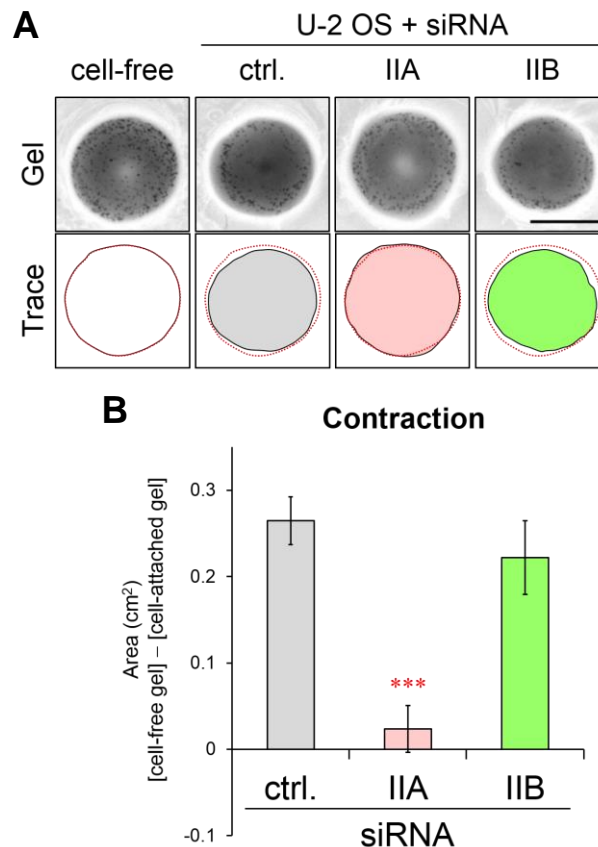


**Fig. 26. Collagen gel contraction assay for analysis of cellular contractility in NMHC-II-depleted cells.**

(A) Top-down images of collagen gels after contraction by siRNA-transfected cells and cell-free collagen gel. Scale bar, 1 cm. Bottom panels represent the traces of gel contour, obtained from corresponding top panels. Dotted red lines are contours of cell-free gel. (B) Changes in the size of each collagen gel, calculated from (A); the area of each cell-attached gel was subtracted by that of cell-free gel. Data represent mean  $\pm$  SEM from four independent experiments. \*\*\*,  $p < 0.001$ , calculated by one-way ANOVA with Dunnett's test.

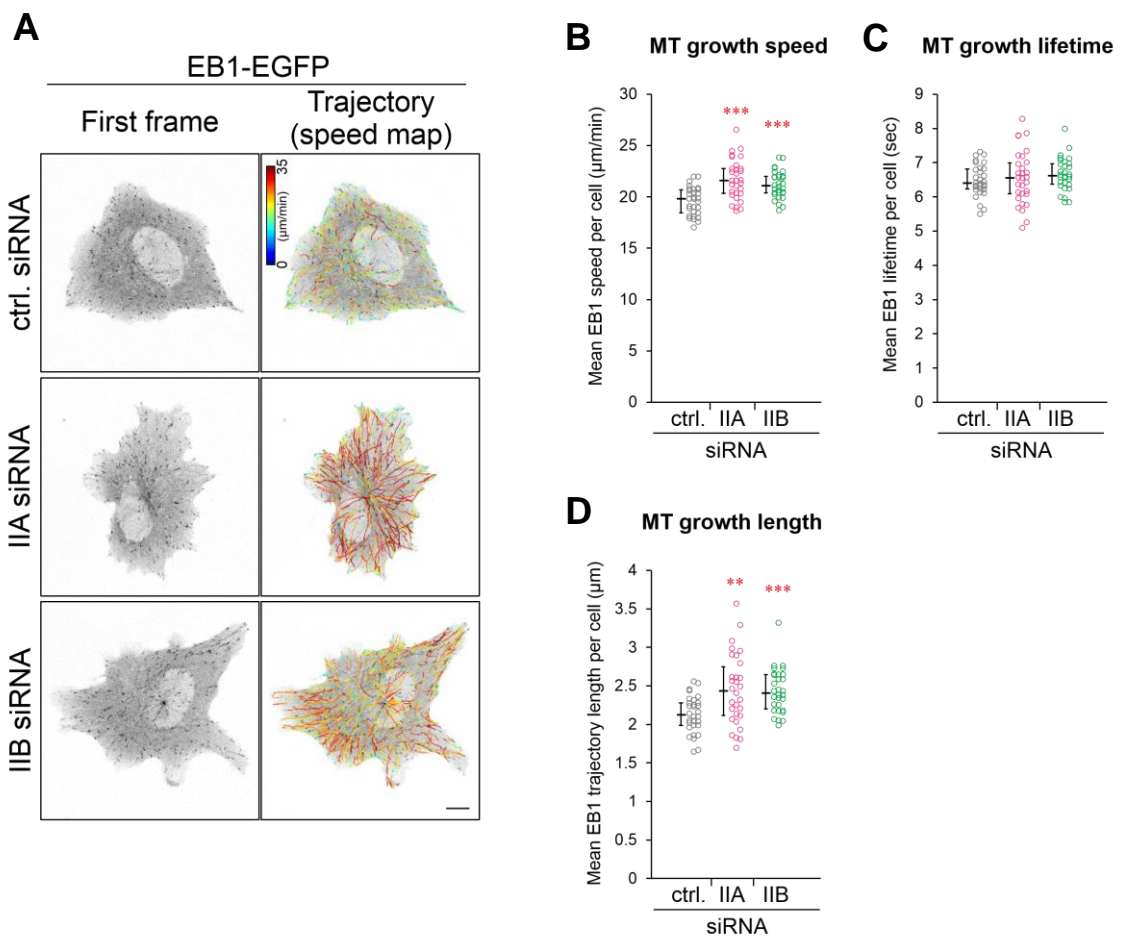


**Fig. 27. Time-lapse imaging of EB1-EGFP for analysis of MT growth dynamics in NMII-depleted cells.**

(A) Still images of time-lapse imaging of EB1-EGFP in siRNA-transfected cells. Left, the first images of the movie of each cell; Right, Spatial speed maps of color-coded comet trajectories of EB1-EGFP, overlaid on the corresponding first images. Scale bar, 10  $\mu\text{m}$ . (B–D) MT growth parameters, calculated using plusTip Tracker software. Mean MT growth speed (B), MT growth lifetime (C), and MT growth length (D) of each cell are as open circles. The median values (center lines), 25<sup>th</sup> percentiles (lower lines), and 75<sup>th</sup> percentiles (upper lines) of each group are also shown at the left of corresponding dot plots. 30 cells per each condition were analyzed. \*\*,  $p < 0.01$ ; \*\*\*,  $p < 0.001$ , calculated by Kruskal–Wallis one-way ANOVA with Steel’s test.

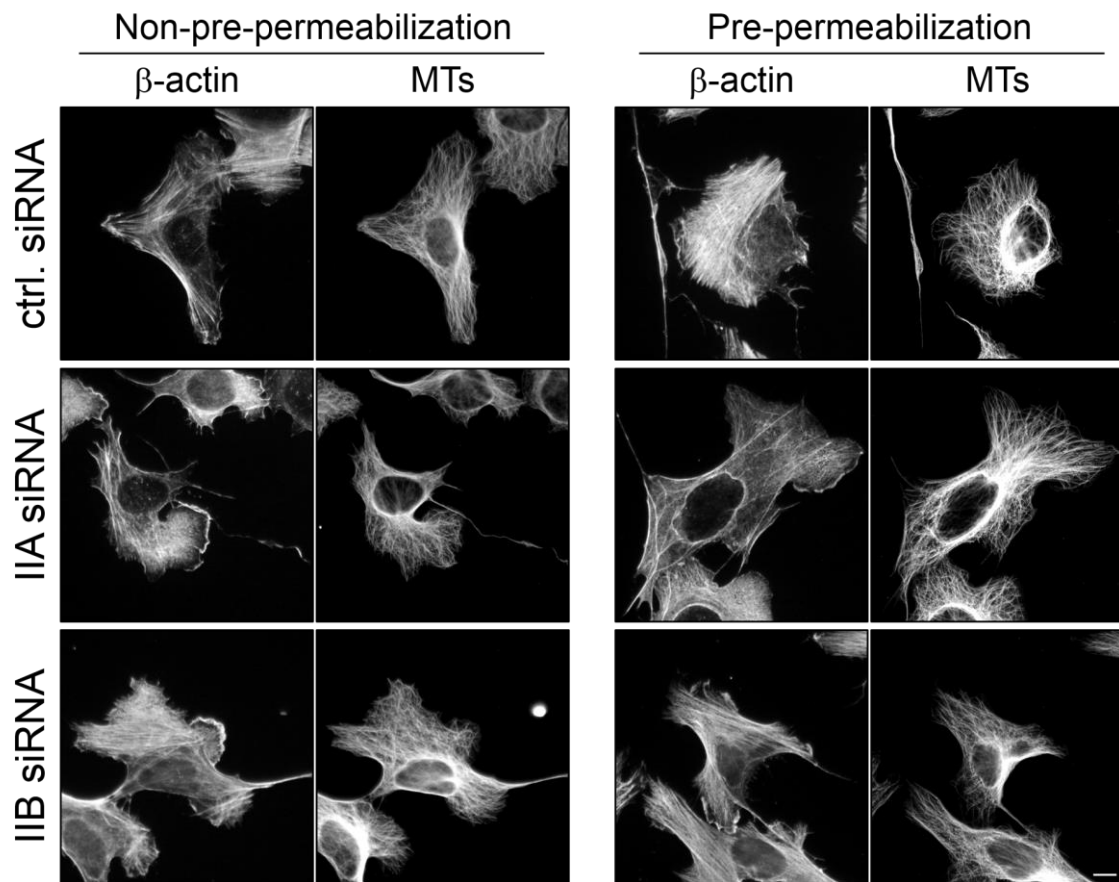


**Fig. 28. Immunofluorescence microscopy for validation of cytoskeletal retention after PEMTT-buffer-mediated cell permeabilization.**

Immunostaining images of  $\beta$ -actin and  $\alpha$ -tubulin in siRNA-transfected cells. Left, the cells were fixed without pre-permeabilization; Right, the cells were fixed after pre-permeabilization with PEMTT-buffer for 60 sec at 37°C. Scale bar, 10  $\mu$ m.

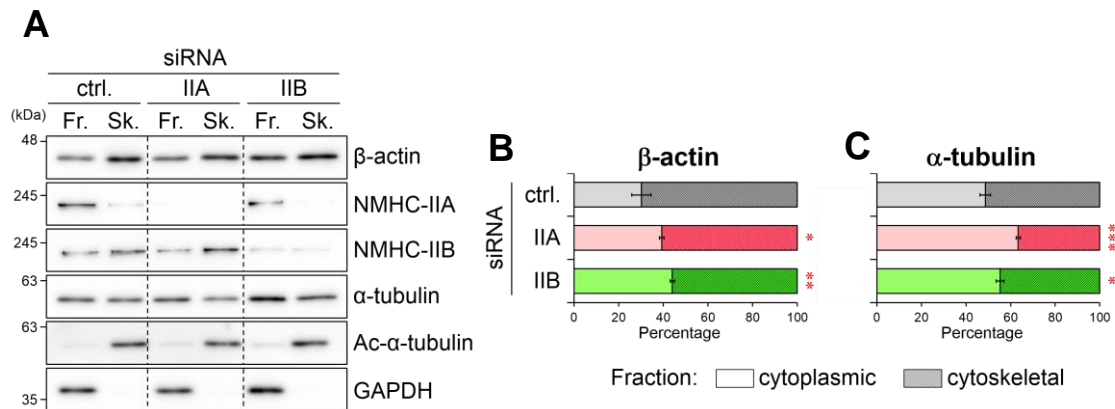


**Fig. 29. SERCYF analysis of cytoskeletal organizations in NMII-depleted cells.**

(A) Immunoblots of fractionated proteins prepared by SERCYF-method from siRNA-transfected cells. Anti-GAPDH antibody was used as a loading control. “Fr.” indicates free, cytoplasmic fractions, “Sk.” indicates cytoskeletal fractions. Anti-GAPDH antibody and anti-acetyl- $\alpha$ -tubulin antibody were used as indicators of cytoplasmic fractions and cytoskeletal fractions, respectively.

(B, C) The percentages of  $\beta$ -actin (B) or  $\alpha$ -tubulin (C) detected at each fraction, calculated from (A). Data represent mean  $\pm$  SEM from five independent experiments. \*,  $p < 0.05$ ; \*\*,  $p < 0.01$ ; \*\*\*,  $p < 0.001$ , calculated by one-way ANOVA with Dunnett’s test.

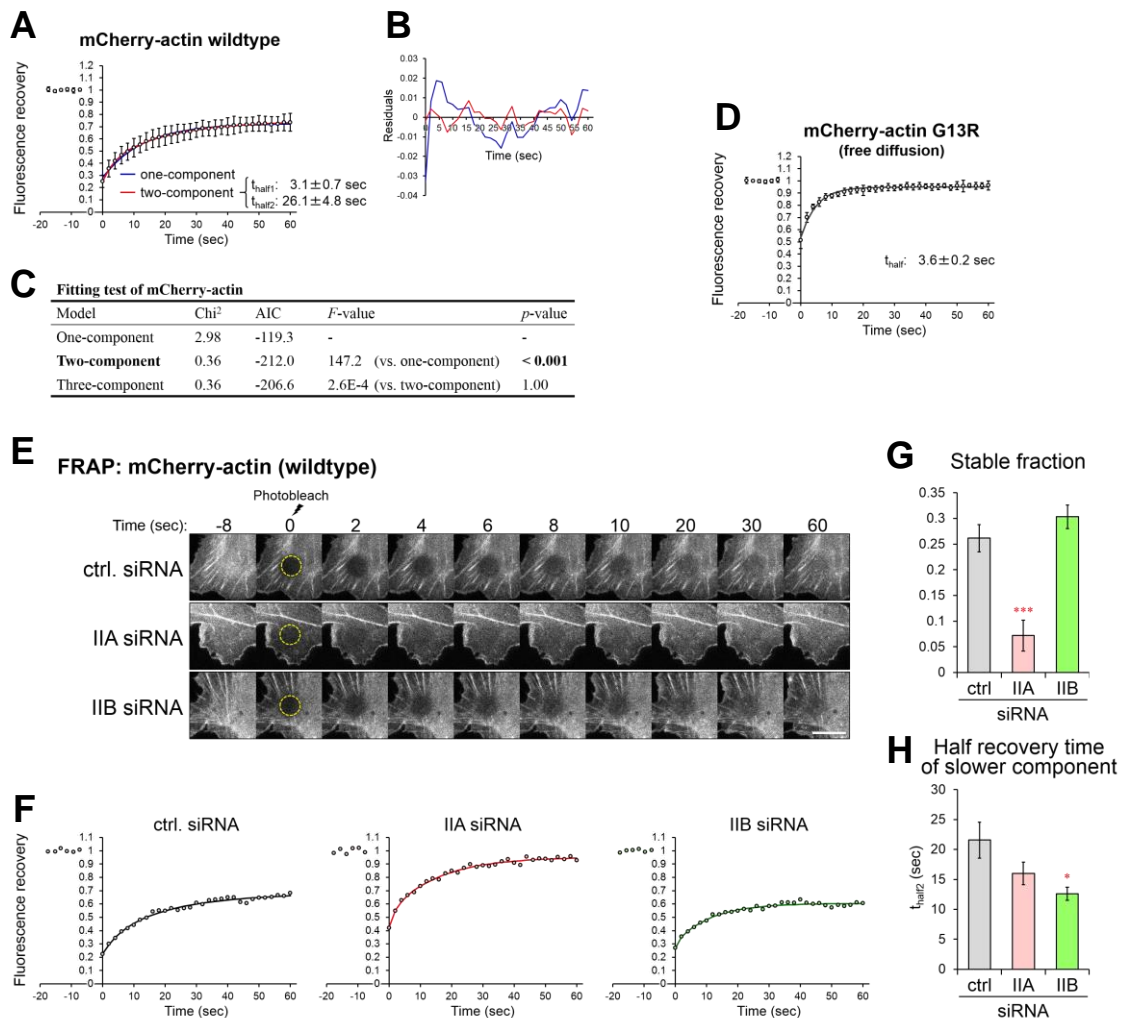


**Fig. 30. FRAP analysis of mCherry-actin for measurement of actin dynamics in NMII-depleted cells.**

(A) Fluorescence recovery curves of mCherry-actin wildtype. The average normalized fluorescence intensity (NFI) at each time point is shown as circles with standard deviation calculated from 10 cells. The blue line represents the result of fitting to a one-component model, and the red line represents the result of fitting to a two-component model. (B) Differences between NFI and the fitting functions at each time point. Colors of the lines are same as those in (A). (C) A summary of the statistical analyses of the fitting tests. (D) Fluorescence recovery curves of mCherry-actin G13R mutant. The average normalized fluorescence intensity (NFI) at each time point is shown as circles with standard deviation calculated from 10 cells. The line represents the result of fitting to a one-component model. (E, F) Representative kymographs and fluorescence recovery curves of mCherry-actin wildtype in siRNA-transfected cells. Each data was fitted to a two-component model. (G, H) Stable fractions (G) and half recovery times of the slower component (H) of mCherry-actin wildtype. 16 cells per each condition were analyzed. Data represent mean  $\pm$  SEM. \*,  $p < 0.05$ ; \*\*\*,  $p < 0.001$ , calculated by one-way ANOVA with Dunnett's test.

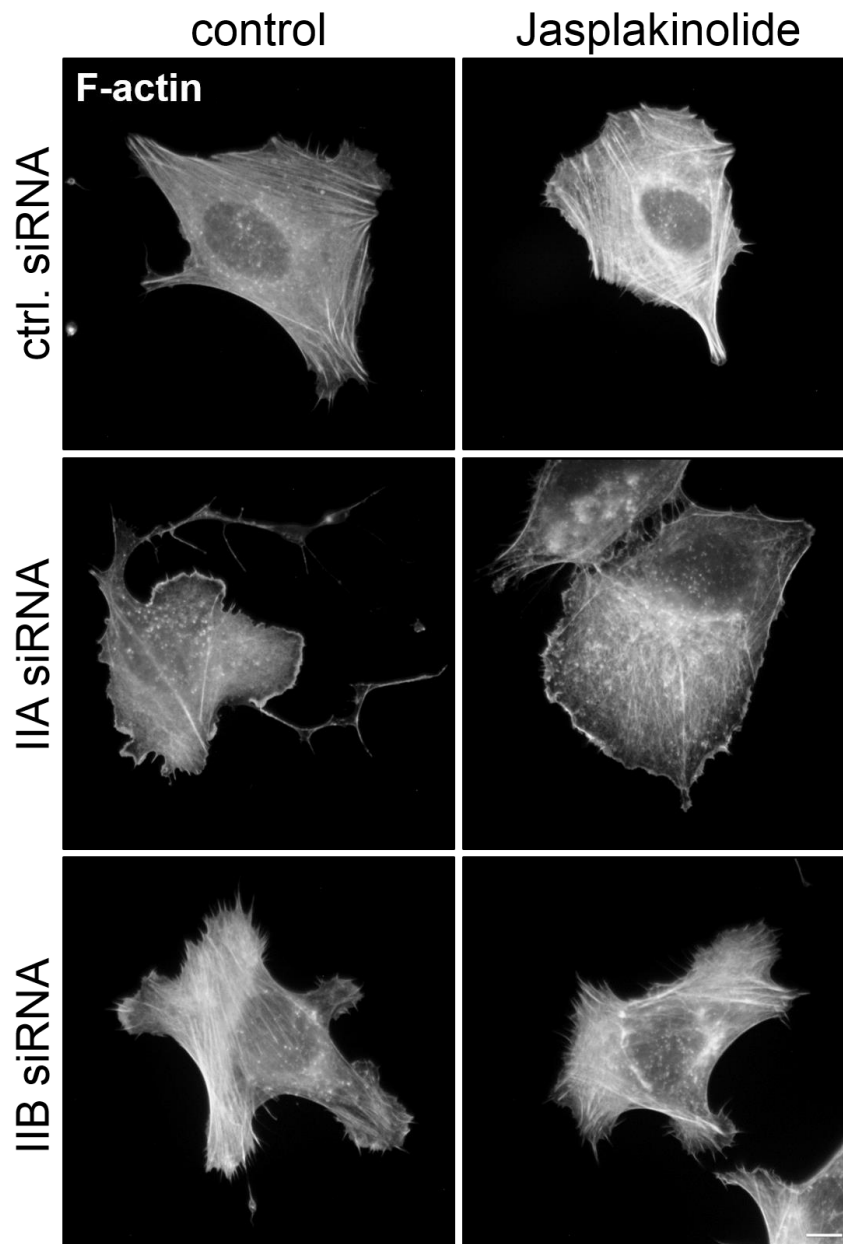


**Fig. 31. Fluorescence microscopy for analysis of the effects of low-dose jasplakinolide on actin filaments.**

Staining images of F-actin in siRNA-transfected cells. Before fixation, cells were treated with 10 nM jasplakinolide for 1 hour. Scale bar, 10  $\mu$ m.

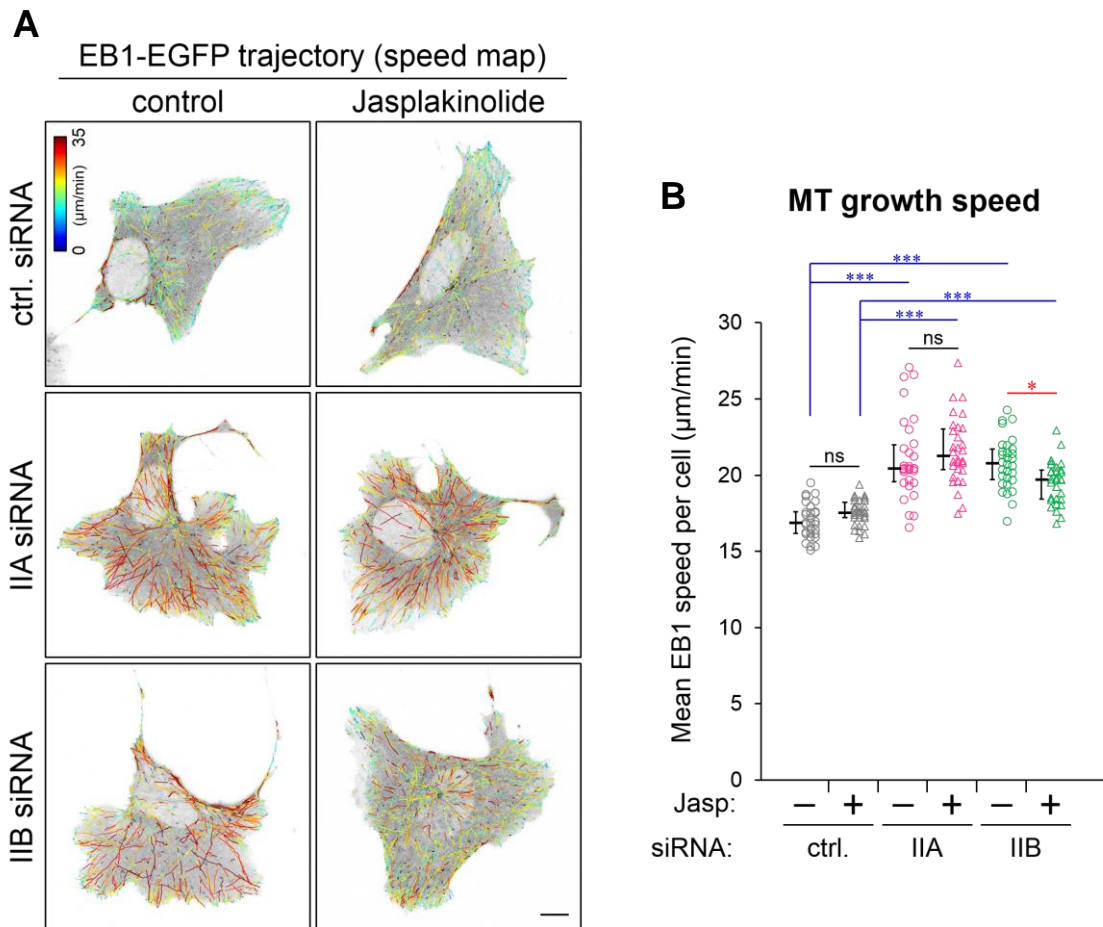


**Fig. 32. Time-lapse imaging of EB1-EGFP for analysis of MT growth speed in jasplakinolide-treated NMII-depleted cells.**

(A) Spatial speed maps of color-coded comet trajectories of EB1-EGFP in siRNA-transfected cells, overlaid on the first images of corresponding movie. Before imaging, the cells were treated with 10 nM jasplakinolide for 1 hour. Scale bar, 10  $\mu\text{m}$ . (B) Mean MT growth speed of each cell. The median values (center lines), 25<sup>th</sup> percentiles (lower lines), and 75<sup>th</sup> percentiles (upper lines) of each group are also shown at the left of corresponding dot plots. 30 cells per each condition were analyzed. \*,  $p < 0.05$ ; \*\*\*,  $p < 0.001$ ; ns, non-significant, calculated by Kruskal–Wallis one-way ANOVA with Steel–Dwass’ test.

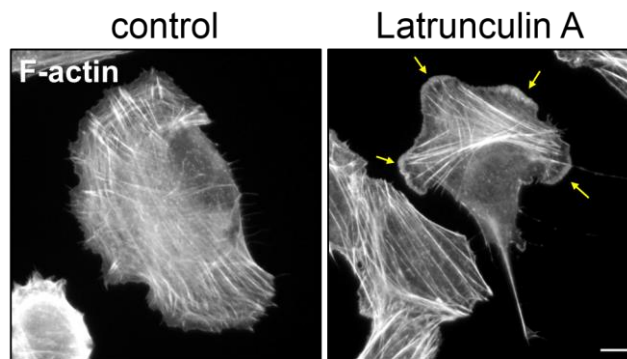


**Fig. 33. Fluorescence microscopy for analysis of the effects of low-dose latrunculin A on actin filaments.**

Staining images of F-actin in cells. Before fixation, cells were treated with 10 nM latrunculin A for 1 hour. Arrows indicate thick lamellipodial protrusions in latrunculin A-treated cells. Scale bar, 10  $\mu\text{m}$ .

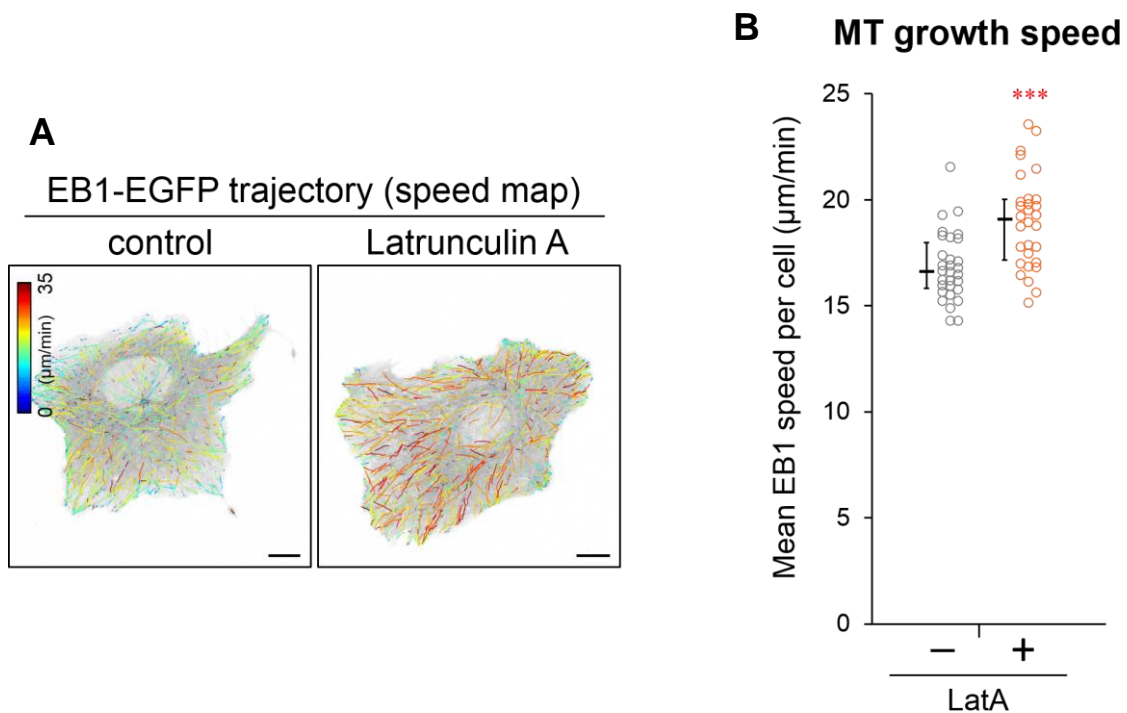


**Fig. 34. Time-lapse imaging of EB1-EGFP for analysis of MT growth speed in latrunculin A-treated cells.**

(A) Spatial speed maps of color-coded comet trajectories of EB1-EGFP, overlaid on the first images of corresponding movie. Before imaging, cells were treated with 10 nM latrunculin A for 1 hour. Scale bars, 10  $\mu\text{m}$ . (B) Mean MT growth speed of each cell. The median values (center lines), 25<sup>th</sup> percentiles (lower lines), and 75<sup>th</sup> percentiles (upper lines) of each group are also shown at the left of corresponding dot plots. 30 cells per each condition were analyzed. \*\*\*,  $p < 0.001$ , calculated by Mann-Whitney  $U$  test.

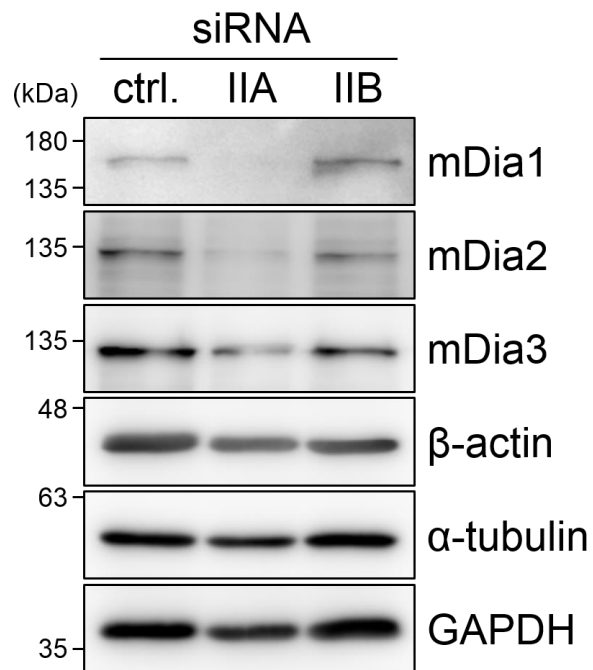


**Fig. 35. Immunoblotting for analysis of the effects of NMII-depletion on expression of mDia proteins.**

Immunoblots of mDia proteins in siRNA-transfected cells.

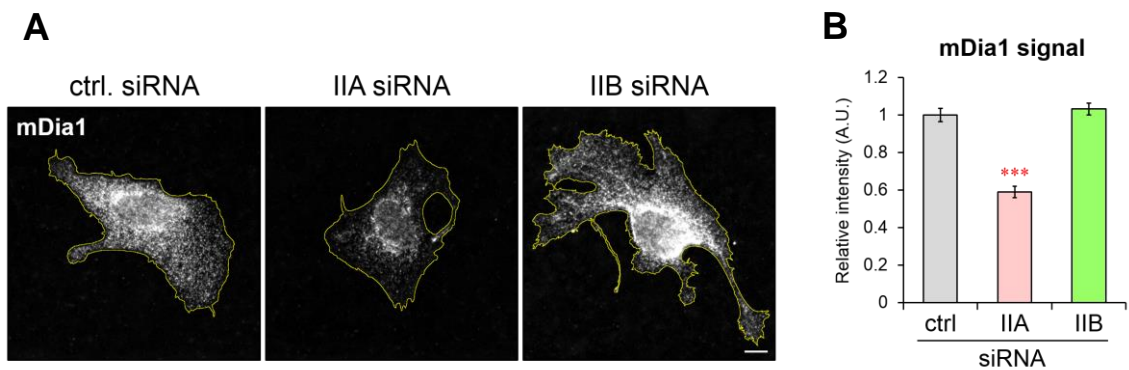


**Fig. 36. Immunofluorescence microscopy for analysis of the effects of NMII-depletion on mDia1 expression.**

(A) Immunostaining images of mDia1 in siRNA-transfected cells. Contours of the cells are drawn in reference to F-actin images visualized with phalloidin. Scale bar, 10  $\mu$ m. (B) Relative immunofluorescence intensity, calculated from (A). More than 30 cells per each condition were analyzed. Data represent mean  $\pm$  SEM. \*\*\*,  $p < 0.001$ , calculated by Kruskal–Wallis one-way ANOVA with Steel’s test.

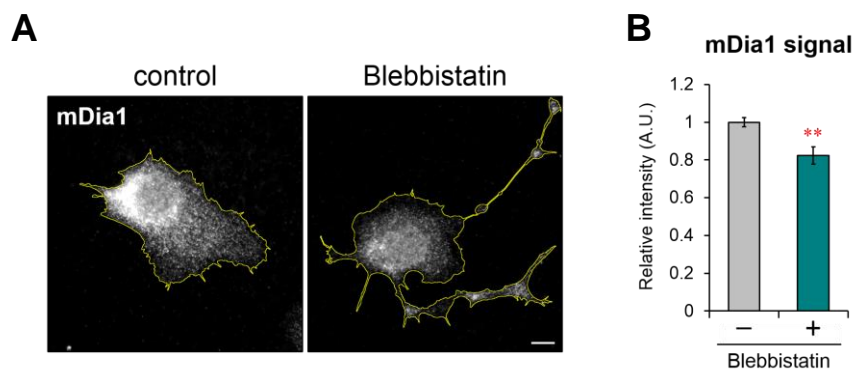


**Fig. 37. Immunofluorescence microscopy for analysis of the effects of blebbistatin treatment on mDia1 expression**

(A) Immunostaining images of mDia1 in cells. Before imaging, cells were treated with 20  $\mu$ M ( $\pm$ )-blebbistatin for 2 days. Contours of the cells are drawn in reference to F-actin images visualized with phalloidin. Scale bar, 10  $\mu$ m. (B) Relative immunofluorescence intensity, calculated from (A). 15 cells from control cells and 14 cells from blebbistatin-treated cells were analyzed. Data represent mean  $\pm$  SEM. \*\*,  $p < 0.01$ , calculated by Mann–Whitney  $U$  test.

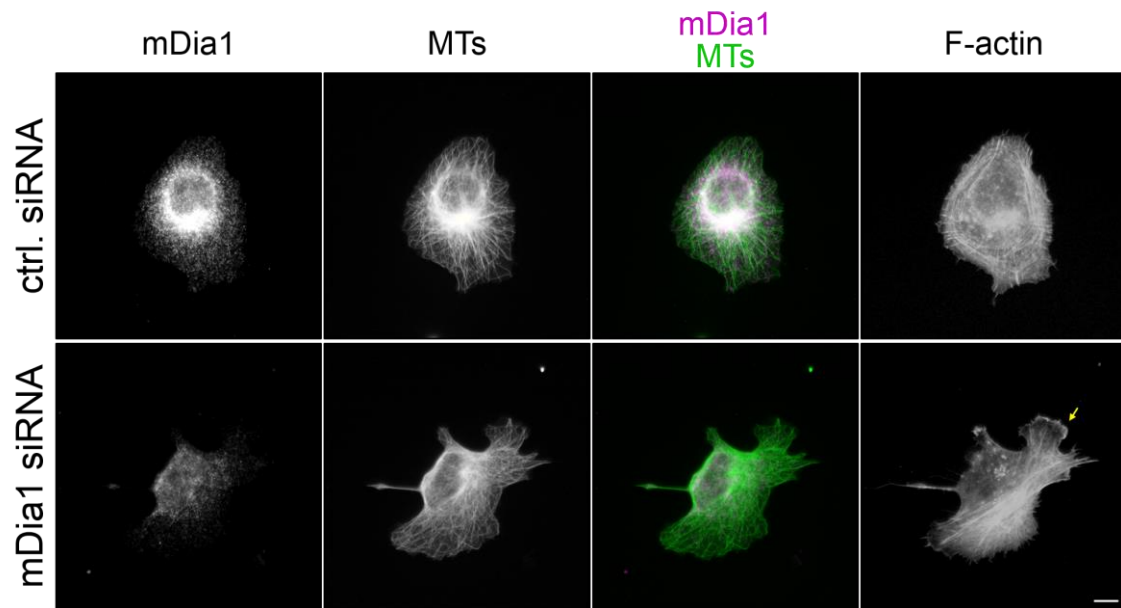


**Fig. 38. Immunofluorescence microscopy for analysis of the effects of mDia1-depletion on actin and MT cytoskeletons.**

Immunostaining images of mDia1 and  $\alpha$ -tubulin in siRNA-transfected cells. The cells were further stained with phalloidin to visualize F-actin. Arrow indicates a thick lamellipodial protrusion in mDia1-depleted cells. Scale bar, 10  $\mu$ m.

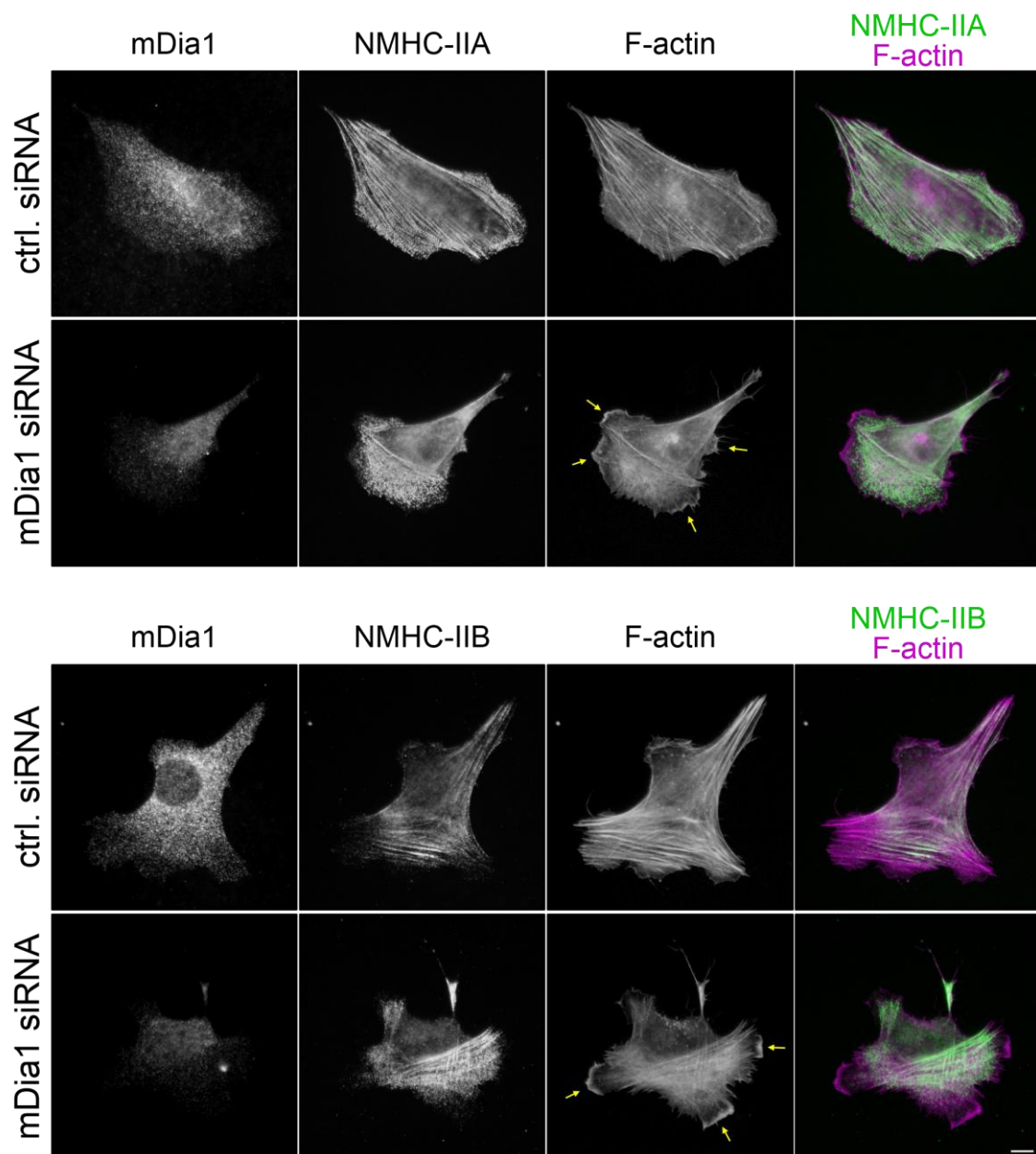


**Fig. 39. Immunofluorescence microscopy for analysis of the effects of mDia1-depletion on NMII isoforms.**

Immunostaining images of mDia1, NMHC-IIA, and NMHC-IIB in siRNA-transfected cells. The cells were further stained with phalloidin to visualize F-actin. Arrows indicate thick lamellipodial protrusions in NMIIB-depleted cells. Scale bar, 10  $\mu$ m.

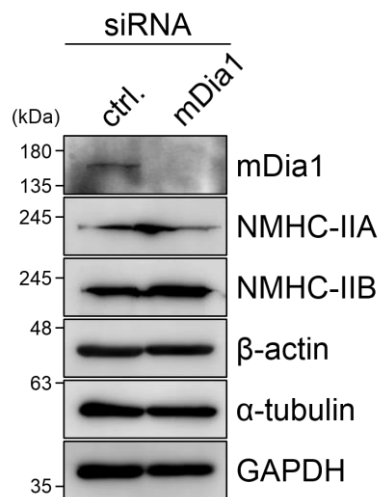


**Fig. 40. Immunoblotting for validation of mDia1-depletion.**

Immunoblots of mDia1 and cytoskeletal proteins in siRNA-transfected cells.

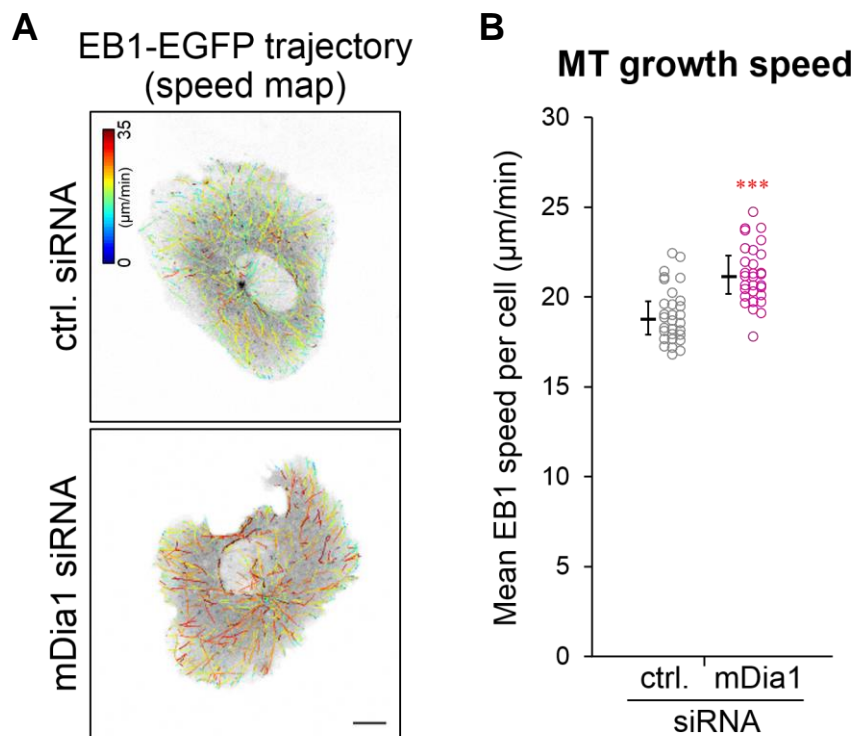


**Fig. 41. Time-lapse imaging of EB1-EGFP for analysis of MT growth speed in mDia1-depleted cells.**

(A) Spatial speed maps of color-coded comet trajectories of EB1-EGFP in siRNA-transfected cells, overlaid on the first images of corresponding movie. Scale bars, 10  $\mu\text{m}$ . (B) Mean MT growth speed of each cell. The median values (center lines), 25<sup>th</sup> percentiles (lower lines), and 75<sup>th</sup> percentiles (upper lines) of each group are also shown at the left of corresponding dot plots. 30 cells per each condition were analyzed. \*\*\*,  $p < 0.001$ , calculated by Mann–Whitney  $U$  test.

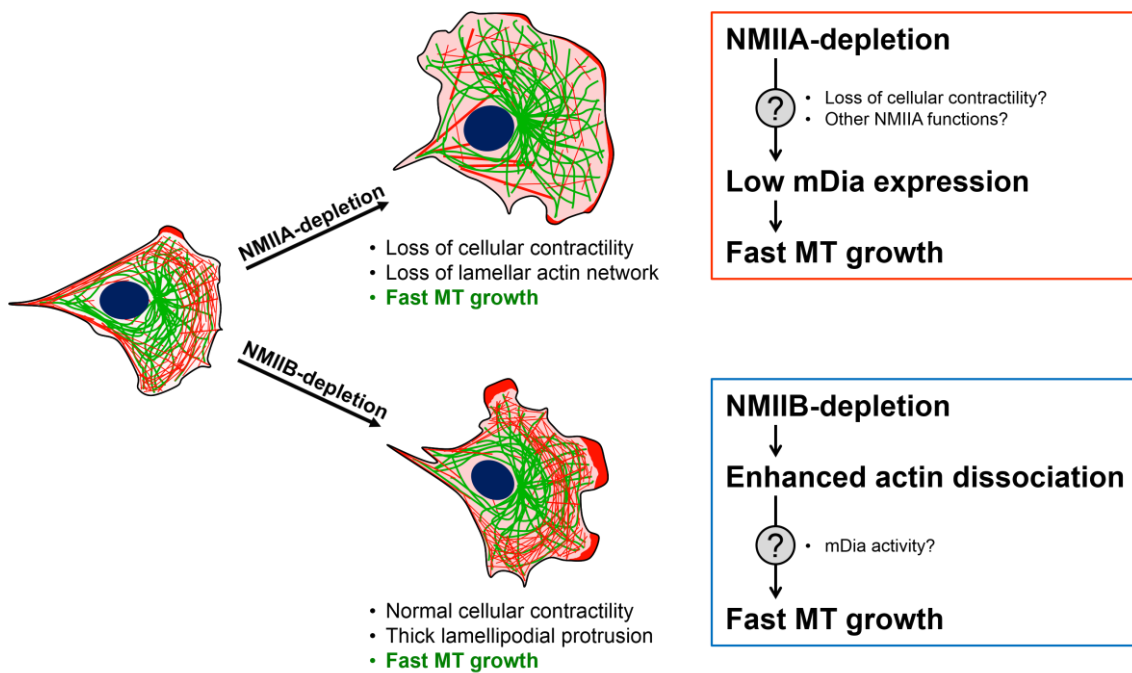


Fig. 42. Summary of the phenotypes of NMII-depleted cells.

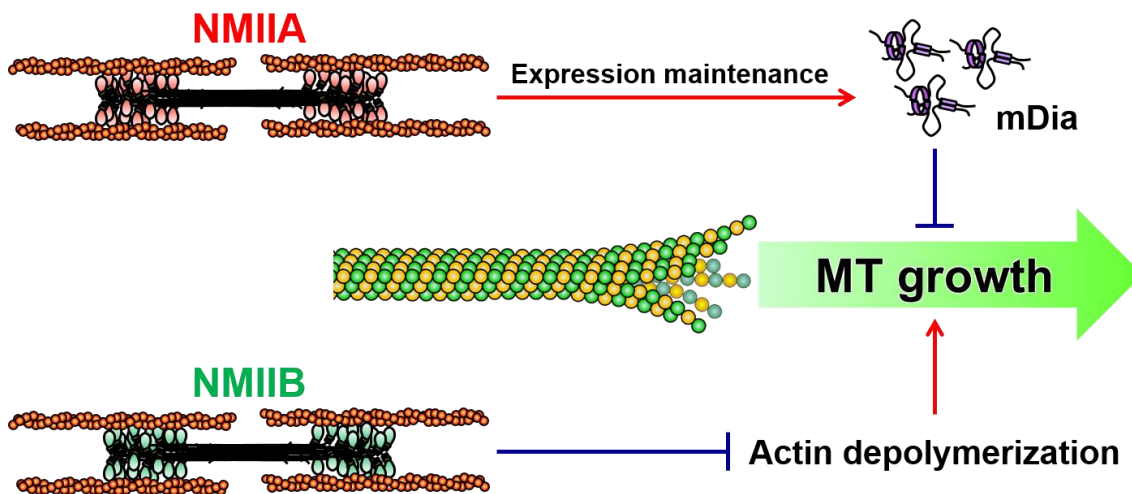


Fig. 43. Schematic model of NMII isoform-dependent MT dynamics regulation.

## General discussion

---

Precise control of each cytoskeletal network is quite important for multiple cellular functions such as cell migration and cell division. Additionally, further communication between different cytoskeletons is also required. There has been increasing recognition of the importance of such cytoskeletal crosstalk; several proteins have been reported to function as crosstalk mediators.

In the context of contractile force generation, NMII is considered to be as one of the mediators that link actin and MT cytoskeletons; however, the underlying mechanism remains unclear. In this thesis, I tackled this problem by two steps—the first step was to establish a method which I named “SERCYF”, for simultaneous and semi-retentive cytoskeletal fractionation; the second step was to investigate the roles of NMIIA and NMIIB in regulating MT dynamics, partially using SERCYF.

In chapter 2, I demonstrated the SERCYF-method as a semi-retentive cytoskeletal fractionation method. The buffer composition of this method is simple: PIPES, EGTA, magnesium, low-dose taxol, and a surfactant. In addition, the experimental procedures of this method are also simple: no requirement of special machinery or techniques. Because of these simplicities, anyone can apply the SERCYF-method easily. Beyond such advantages, the number of cells improperly detached from the substrate appears to be very small even after the treatment with the permeabilization buffer. Although the reason remains unclear, this point is also a big advantage of this method; thus, the use of SERCYF-method, instead of other methods, will improve the quantitative accuracy of the fractionation experiments.

In chapter 3, I demonstrated the distinct functions of NMIIA and NMIIB in actin–MT crosstalk. There are several reports addressing the function of NMII in MT regulation, and most of them focused on NMII’s ability to generate contractile force. My research, however, showed that NMIIB regulates MT dynamics in a manner independent of contractile force generation. The detailed mechanism remains unclear, but actin dissociation seems to be involved in the mechanism. Interestingly, NMIIA-dependent MT regulatory mechanism was found to be largely different from NMIIB-dependent one; NMIIA-depleted cells showed unexpected decrease in mDia expression. As mDia proteins dynamically and structurally stabilize MTs, the loss mDia could be the main cause of acceleration of MT growth in NMIIA-depleted cells. In this study, I investigated the expression levels of only mDia isoforms, mDia1, mDia2, and mDia3, but it is possible that other formin proteins, such as DAAM1, INF1, or FHOD1, are also affected by NMIIA-depletion. Another question is how mDia isoforms were decreased—protein degradation? translational inhibition? or transcriptional inhibition? There are no reports showing a quantitative control of formin proteins levels by NMII. Because NMII and formins are involved in the regulation of both actin and MT dynamics, it is worth investigating the detailed relationship between NMII and formin proteins.

In summary, in this study I analyzed the functions of NMII isoforms in actin–MT crosstalk and demonstrated that NMIIA and NMIIIB differently regulate MT dynamics as well as actin dynamics. In addition, in the process, I established a fractionation method that can be applied for both actin and MT analysis. I believe this method contributes to the development of cell biology, especially in the field of cytoskeletal crosstalk. Also I believe that detailed analysis of the significance of NMII-dependent MT regulation on cell shape determination and cell migration will help us to understand the complicated cellular processes.

## References

---

- Addi, C., Bai, J. and Echard, A.** (2018). Actin, microtubule, septin and ESCRT filament remodeling during late steps of cytokinesis. *Curr. Opin. Cell Biol.* **50**, 27–34.
- Aguilar-Cuenca, R., Juanes-García, A. and Vicente-Manzanares, M.** (2014). Myosin II in mechanotransduction: Master and commander of cell migration, morphogenesis, and cancer. *Cell. Mol. Life Sci.* **71**, 479–492.
- Akhmanova, A. and Steinmetz, M. O.** (2010). Microtubule +TIPs at a glance. *J. Cell Sci.* **123**, 3414–3418.
- Akhmanova, A. and Steinmetz, M. O.** (2015). Control of microtubule organization and dynamics: two ends in the limelight. *Nat. Rev. Mol. Cell Biol.* **16**, 711–726.
- Al-Bassam, J. and Corbett, K. D.** (2012).  $\alpha$ -Tubulin acetylation from the inside out. *Proc. Natl. Acad. Sci.* **109**, 19515–19516.
- Ali, M. Y., Krementsova, E. B., Kennedy, G. G., Mahaffy, R., Pollard, T. D., Trybus, K. M. and Warshaw, D. M.** (2007). Myosin Va maneuvers through actin intersections and diffuses along microtubules. *Proc. Natl. Acad. Sci.* **104**, 4332–4336.
- Applegate, K. T., Besson, S., Matov, A., Bagonis, M. H., Jaqaman, K. and Danuser, G.** (2011). plusTipTracker : Quantitative image analysis software for the measurement of microtubule dynamics. *J. Struct. Biol.* **176**, 168–184.
- Arnal, I., Heichette, C., Diamantopoulos, G. S. and Chrétien, D.** (2004). CLIP-170/tubulin-curved oligomers coassemble at microtubule ends and promote rescues. *Curr. Biol.* **14**, 2086–95.
- Bartolini, F. and Gundersen, G. G.** (2010). Formins and microtubules. *Biochim. Biophys. Acta - Mol. Cell Res.* **1803**, 164–173.
- Bartolini, F., Moseley, J. B., Schmoranzler, J., Cassimeris, L., Goode, B. L. and Gundersen, G. G.** (2008). The formin mDia2 stabilizes microtubules independently of its actin nucleation activity. *J. Cell Biol.* **181**, 523–536.
- Bartolini, F., Ramalingam, N. and Gundersen, G. G.** (2012). Actin-capping protein promotes microtubule stability by antagonizing the actin activity of mDia1. *Mol. Biol. Cell* **23**, 4032–4040.
- Bartolini, F., Andres-Delgado, L., Qu, X., Nik, S., Ramalingam, N., Kremer, L., Alonso, M. A. and Gundersen, G. G.** (2016). An mDia1-INC2 formin activation cascade facilitated by IQGAP1 regulates stable microtubules in migrating cells. *Mol. Biol. Cell* **27**, 1797–808.
- Bearce, E. A., Erdogan, B. and Lowery, L. A.** (2015). TIPsy tour guides: how microtubule plus-end tracking proteins (+TIPs) facilitate axon guidance. *Front. Cell. Neurosci.* **9**, 241.
- Bender, M., Stritt, S., Nurden, P., van Eeuwijk, J. M. M., Zieger, B., Kentouche, K., Schulze, H., Morbach, H., Stegner, D., Heinze, K. G., et al.** (2014). Megakaryocyte-

- specific Profilin1-deficiency alters microtubule stability and causes a Wiskott-Aldrich syndrome-like platelet defect. *Nat. Commun.* **5**, 4746.
- Birkenfeld, J., Nalbant, P., Yoon, S. H. and Bokoch, G. M.** (2008). Cellular functions of GEF-H1, a microtubule-regulated Rho-GEF: is altered GEF-H1 activity a crucial determinant of disease pathogenesis? *Trends Cell Biol.* **18**, 210–219.
- Bouameur, J. E., Favre, B. and Borradori, L.** (2014). Plakins, a versatile family of cytolinkers: Roles in skin integrity and in human diseases. *J. Invest. Dermatol.* **134**, 885–894.
- Braun, A., Dang, K., Buslig, F., Baird, M. A., Davidson, M. W., Waterman, C. M. and Myers, K. A.** (2014). Rac1 and Aurora A regulate MCAK to polarize microtubule growth in migrating endothelial cells. *J. Cell Biol.* **206**, 97–112.
- Breckenridge, M. T., Dulyaninova, N. G. and Egelhoff, T. T.** (2009). Multiple regulatory steps control mammalian nonmuscle myosin II assembly in live cells. *Mol. Biol. Cell* **20**, 338–47.
- Brouhard, G. J.** (2015). Dynamic instability 30 years later: complexities in microtubule growth and catastrophe. *Mol. Biol. Cell* **26**, 1207–10.
- Burridge, K. and Wittchen, E. S.** (2013). The tension mounts: stress fibers as force-generating mechanotransducers. *J. Cell Biol.* **200**, 9–19.
- Cabrales Fontela, Y., Kadavath, H., Biernat, J., Riedel, D., Mandelkow, E. and Zweckstetter, M.** (2017). Multivalent cross-linking of actin filaments and microtubules through the microtubule-associated protein Tau. *Nat. Commun.* **8**, 1–12.
- Carlier, M. F. and Shekhar, S.** (2017). Global treadmilling coordinates actin turnover and controls the size of actin networks. *Nat. Rev. Mol. Cell Biol.* **18**, 389–401.
- Chang, Y.-C., Nalbant, P., Birkenfeld, J., Chang, Z.-F. and Bokoch, G. M.** (2008). GEF-H1 couples nocodazole-induced microtubule disassembly to cell contractility via RhoA. *Mol. Biol. Cell* **19**, 2147–53.
- Cheng, L., Zhang, J., Ahmad, S., Rozier, L., Yu, H., Deng, H. and Mao, Y.** (2011). Aurora B Regulates Formin mDia3 in Achieving Metaphase Chromosome Alignment. *Dev. Cell* **20**, 342–352.
- Chesarone, M. A., Dupage, A. G. and Goode, B. L.** (2010). Unleashing formins to remodel the actin and microtubule cytoskeletons. *Nat. Rev. Mol. Cell Biol.* **11**, 62–74.
- Chugh, P. and Paluch, E. K.** (2018). The actin cortex at a glance. *J. Cell Sci.* **131**, jcs186254.
- Conti, M. A., Even-Ram, S., Liu, C., Yamada, K. M. and Adelstein, R. S.** (2004). Defects in cell adhesion and the visceral endoderm following ablation of nonmuscle myosin heavy chain II-A in mice. *J. Biol. Chem.* **279**, 41263–41266.
- D'Angelo, L., Myer, N. M. and Myers, K. A.** (2017). MCAK-mediated regulation of endothelial cell microtubule dynamics is mechanosensitive to myosin-II contractility. *Mol.*

- Biol. Cell* **28**, 1223–1237.
- Dahan, I., Petrov, D., Cohen-Kfir, E. and Ravid, S.** (2014). The tumor suppressor Lgl1 forms discrete complexes with NMII-A and Par6 $\alpha$ -aPKC $\zeta$  that are affected by Lgl1 phosphorylation. *J. Cell Sci.* **127**, 295–304.
- Daou, P., Hasan, S., Breitsprecher, D., Baudalet, E., Camoin, L., Audebert, S., Goode, B. L. and Badache, A.** (2014). Essential and nonredundant roles for Diaphanous formins in cortical microtubule capture and directed cell migration. *Mol. Biol. Cell* **25**, 658–668.
- De Forges, H., Bouissou, A. and Perez, F.** (2012). Interplay between microtubule dynamics and intracellular organization. *Int. J. Biochem. Cell Biol.* **44**, 266–274.
- Dent, E. W. and Gertler, F. B.** (2003). Cytoskeletal Dynamics and Transport in Growth Cone Motility and Axon Guidance. **40**, 209–227.
- Enomoto, T.** (1996). Microtubule Disruption Induces the Formation of Actin Stress Fibers and Focal Adhesions in Cultured Cells: Possible Involvement of the Rho Signal Cascade. *Cell Struct. Funct.* **21**, 317–326.
- Etienne-Manneville, S.** (2013). Microtubules in cell migration. *Annu. Rev. Cell Dev. Biol.* **29**, 471–99.
- Even-Ram, S., Doyle, A. D., Conti, M. A., Matsumoto, K., Adelstein, R. S. and Yamada, K. M.** (2007). Myosin IIA regulates cell motility and actomyosin-microtubule crosstalk. *Nat. Cell Biol.* **9**, 299–309.
- Fernández, J. and Miguel, B.** (2018). Coordination of microtubule acetylation and the actin cytoskeleton by formins. *Cell. Mol. Life Sci.*
- Fischer, R. S., Gardel, M., Ma, X., Adelstein, R. S. and Waterman, C. M.** (2009). Local Cortical Tension by Myosin II Guides 3D Endothelial Cell Branching. *Curr. Biol.* **19**, 260–265.
- Folker, E. S., Baker, B. M. and Goodson, H. V.** (2005). Interactions between CLIP-170, tubulin, and microtubules: implications for the mechanism of Clip-170 plus-end tracking behavior. *Mol. Biol. Cell* **16**, 5373–84.
- Galjart, N.** (2010). Plus-end-tracking proteins and their interactions at microtubule ends. *Curr. Biol.* **20**, R528–R537.
- Golomb, E., Ma, X., Jana, S. S., Preston, Y. A., Kawamoto, S., Shoham, N. G., Goldin, E., Conti, M. A., Sellers, J. R. and Adelstein, R. S.** (2004). Identification and Characterization of Nonmuscle Myosin II-C, a New Member of the Myosin II Family. *J. Biol. Chem.* **279**, 2800–2808.
- Gorbsky, G. J.** (2004). Mitosis: MCAK under the Aura of Aurora B. *Curr. Biol.* **14**, 346–348.
- Grenklo, S., Johansson, T., Bertilson, L. and Karlsson, R.** (2004). Anti-actin antibodies generated against profilin: Actin distinguish between non-filamentous and filamentous actin, and label cultured cells in a dotted pattern. *Eur. J. Cell Biol.* **83**, 413–423.

- Gupton, S. L., Eisenmann, K., Alberts, a. S. and Waterman-Storer, C. M.** (2007). mDia2 regulates actin and focal adhesion dynamics and organization in the lamella for efficient epithelial cell migration. *J. Cell Sci.* **120**, 3475–3487.
- Heissler, S. M. and Manstein, D. J.** (2011). Comparative kinetic and functional characterization of the motor domains of human nonmuscle myosin-2C isoforms. *J. Biol. Chem.* **286**, 21191–21202.
- Heissler, S. M. and Manstein, D. J.** (2013). Nonmuscle myosin-2: mix and match. *Cell. Mol. Life Sci.* **70**, 1–21.
- Helenius, J., Brouhard, G., Kalaidzidis, Y., Diez, S. and Howard, J.** (2006). The depolymerizing kinesin MCAK uses lattice diffusion to rapidly target microtubule ends. *Nature* **441**, 115–119.
- Henty-Ridilla, J. L., Rankova, A., Eskin, J. A., Kenny, K. and Goode, B. L.** (2016). Accelerated actin filament polymerization from microtubule plus ends. *Science* **352**, 1004–9.
- Henty-Ridilla, J. L., Juanes, M. A. and Goode, B. L.** (2017). Profilin Directly Promotes Microtubule Growth through Residues Mutated in Amyotrophic Lateral Sclerosis. *Curr. Biol.* **27**, 3535–3543.e4.
- Higashida, C., Miyoshi, T., Fujita, A., Ocegüera-Yanez, F., Monypenny, J., Andou, Y., Narumiya, S. and Watanabe, N.** (2004). Actin polymerization-driven molecular movement of mDia1 in living cells. *Science* **303**, 2007–10.
- Higashida, C., Suetsugu, S., Tsuji, T., Monypenny, J., Narumiya, S. and Watanabe, N.** (2008). G-actin regulates rapid induction of actin nucleation by mDia1 to restore cellular actin polymers. *J. Cell Sci.* **121**, 3403–3412.
- Higashida, C., Kiuchi, T., Akiba, Y., Mizuno, H., Maruoka, M., Narumiya, S., Mizuno, K. and Watanabe, N.** (2013). F- and G-actin homeostasis regulates mechanosensitive actin nucleation by formins. *Nat. Cell Biol.* **15**, 395–405.
- Hirata, N., Takahashi, M. and Yazawa, M.** (2009). Diphosphorylation of regulatory light chain of myosin IIA is responsible for proper cell spreading. *Biochem. Biophys. Res. Commun.* **381**, 682–687.
- Hu, C., Coughlin, M., Field, C. M. and Mitchison, T. J.** (2011). Article KIF4 Regulates Midzone Length during Cytokinesis. *Curr. Biol.* **21**, 815–824.
- Huang, J. D., Brady, S. T., Richards, B. W., Stenolen, D., Resau, J. H., Copeland, N. G. and Jenkins, N. a** (1999). Direct interaction of microtubule- and actin-based transport motors. *Nature* **397**, 267–270.
- Huber, F., Boire, A., López, M. P. and Koenderink, G. H.** (2015). Cytoskeletal crosstalk: When three different personalities team up. *Curr. Opin. Cell Biol.* **32**, 39–47.
- Infante, A., S, Stein, M. S., Zhai, Y., Borisy, G. G. and Gundersen, G. G.** (2000).

- Detyrosinated (Glu) microtubules are stabilized by an ATP-sensitive plus-end cap. *J. Cell Sci.* **113** ( Pt 2, 3907–3919).
- Jana, S. S., Kawamoto, S. and Adelstein, R. S.** (2006). A specific isoform of nonmuscle myosin II-C is required for cytokinesis in a tumor cell line. *J. Biol. Chem.* **281**, 24662–24670.
- Janke, C. and Bulinski, J. C.** (2011). Post-translational regulation of the microtubule cytoskeleton: mechanisms and functions. *Nat. Rev. Mol. Cell Biol.* **12**, 773–86.
- Joo, E. E. and Yamada, K. M.** (2014). MYPT1 regulates contractility and microtubule acetylation to modulate integrin adhesions and matrix assembly. *Nat. Commun.* **5**, 3510.
- Joo, E. E. and Yamada, K. M.** (2016). Post-polymerization crosstalk between the actin cytoskeleton and microtubule network. *Bioarchitecture* **6**, 53–59.
- Jorrich, M. H., Shih, W. and Yamada, S.** (2013). Myosin IIA deficient cells migrate efficiently despite reduced traction forces at cell periphery. *Biol. Open* **2**, 368–72.
- Jurewicz, E., Wyroba, E. and Filipek, A.** (2018). Tubulin-dependent secretion of S100A6 and cellular signaling pathways activated by S100A6-integrin  $\beta$ 1 interaction. *Cell. Signal.* **42**, 21–29.
- Kaverina, I. and Straube, A.** (2011). Regulation of cell migration by dynamic microtubules. *Semin. Cell Dev. Biol.* **22**, 968–74.
- Kiboku, T., Katoh, T., Nakamura, A., Kitamura, A., Kinjo, M., Murakami, Y. and Takahashi, M.** (2013). Nonmuscle myosin II folds into a 10S form via two portions of tail for dynamic subcellular localization. *Genes Cells* **18**, 90–109.
- Kim, K. Y., Kovács, M., Kawamoto, S., Sellers, J. R. and Adelstein, R. S.** (2005). Disease-associated mutations and alternative splicing alter the enzymatic and motile activity of nonmuscle myosins II-B and II-C. *J. Biol. Chem.* **280**, 22769–22775.
- Kolega, J.** (1997). Asymmetry in the distribution of free versus cytoskeletal myosin II in locomoting microcapillary endothelial cells. *Exp Cell Res* **231**, 66–82.
- Kollins, K. M., Hy, J., Bridgman, P. C., Hyang, Y. Q. and Gallo, G.** (2009). Myosin-II negatively regulates minor process extension and the temporal development of neuronal polarity. *Dev. Neurobiol.* **69**, 279–298.
- Kovács, M., Wang, F., Hu, A., Zhang, Y. and Sellers, J. R.** (2003). Functional divergence of human cytoplasmic myosin II. Kinetic characterization of the non-muscle IIA isoform. *J. Biol. Chem.* **278**, 38132–38140.
- Krendel, M., Zenke, F. T. and Bokoch, G. M.** (2002). Nucleotide exchange factor GEF-H1 mediates cross-talk between microtubules and the actin cytoskeleton. *Nat. Cell Biol.* **4**, 294–301.
- Kumar, P. and Wittmann, T.** (2012). +TIPs: SxIPping along microtubule ends. *Trends Cell Biol.* **22**, 418–428.

- Kuragano, M.** (2018). Studies on Roles of Nonmuscle Myosin II Isoforms in Stress Fiber Organization and Directionally Persistent Migration of Fibroblasts. *PhD thesis*, Hokkaido University, Hokkaido, Japan.
- Kuragano, M., Murakami, Y. and Takahashi, M.** (2018a). Nonmuscle myosin IIA and IIB differentially contribute to intrinsic and directed migration of human embryonic lung fibroblasts. *Biochem. Biophys. Res. Commun.* **498**, 25–31.
- Kuragano, M., Uyeda, T. Q., Kamijo, K., Murakami, Y. and Takahashi, M.** (2018b). Different contributions of nonmuscle myosin IIA and IIB to the organization of stress fiber subtypes in fibroblasts. *Mol. Biol. Cell* **29**, mbc.E17-04-0215.
- Landino, J. and Ohi, R.** (2016). The Timing of Midzone Stabilization during Cytokinesis Depends on Myosin II Activity and an Interaction between INCENP and Actin. *Curr. Biol.* **26**, 698–706.
- Lowery, L. A. and Vactor, D. Van** (2009). The trip of the tip: Understanding the growth cone machinery. *Nat. Rev. Mol. Cell Biol.* **10**, 332–343.
- Ma, X., Jana, S. S., Conti, M. A., Kawamoto, S., Claycomb, W. C. and Adelstein, R. S.** (2010). Ablation of nonmuscle myosin II-B and II-C reveals a role for nonmuscle myosin II in cardiac myocyte karyokinesis. *Mol. Biol. Cell* **21**, 3952–62.
- Matov, A., Applegate, K., Kumar, P., Thoma, C., Krek, W., Danuser, G. and Wittmann, T.** (2010). Analysis of microtubule dynamic instability using a plus-end growth marker. *Nat. Methods* **7**, 761–8.
- Matsushima, K., Tokuraku, K., Hasan, M. R. and Kotani, S.** (2012). Microtubule-associated protein 4 binds to actin filaments and modulates their properties. *J. Biochem.* **151**, 99–108.
- Maupin, P., Phillips, C. L., Adelstein, R. S. and Pollard, T. D.** (1994). Differential localization of myosin-II isozymes in human cultured cells and blood cells. *J. Cell Sci.* **107** ( Pt 1, 3077–3090.
- Miki, M., Wahl, P. and Auchet, J.** (1982). Fluorescence Anisotropy of Labeled F-Actin : Influence of Divalent Cations on the Interaction between F-Actin and Myosin Heads1 ". *Biochemistry* **21**, 3661–3665.
- Mimori-Kiyosue, Y., Shiina, N. and Tsukita, S.** (2000). The dynamic behavior of the APC-binding protein EB1 on the distal ends of microtubules. *Curr. Biol.* **10**, 865–8.
- Mohan, R. and John, A.** (2015). Microtubule-associated proteins as direct crosslinkers of actin filaments and microtubules. *IUBMB Life* **67**, 395–403.
- Murakami, N., Singh, S. S., Chauhan, V. P. S. and Elzinga, M.** (1995). Phospholipid Binding, Phosphorylation by Protein Kinase C, and Filament Assembly of the COOH Terminal Heavy Chain Fragments of Nonmuscle Myosin II Isoforms Mil A and MIIB. *Biochemistry* **34**, 16046–16055.
- Myers, K. A., Applegate, K. T., Danuser, G., Fischer, R. S. and Waterman, C. M.** (2011).

- Distinct ECM mechanosensing pathways regulate microtubule dynamics to control endothelial cell branching morphogenesis. *J. Cell Biol.* **192**, 321–334.
- Na, G. C. and Timasheff, S. N.** (1981). Interaction of calf brain tubulin with glycerol. *J. Mol. Biol.* **151**, 165–178.
- Nagae, S., Meng, W. and Takeichi, M.** (2013). Non-centrosomal microtubules regulate F-actin organization through the suppression of GEF-H1 activity. *Genes to Cells* **18**, 387–396.
- Nakamura, F., Stossel, T. P. and Hartwig, J. H.** (2011). The filamins: Organizers of cell structure and function. *Cell Adhes. Migr.* **5**, 160–169.
- Nakasawa, T., Takahashi, M., Matsuzawa, F., Aikawa, S., Togashi, Y., Saitoh, T., Yamagishi, A. and Yazawa, M.** (2005). Critical regions for assembly of vertebrate nonmuscle myosin II. *Biochemistry* **44**, 174–183.
- Nehlig, A., Molina, A., Rodrigues-Ferreira, S., Honoré, S. and Nahmias, C.** (2017). Regulation of end-binding protein EB1 in the control of microtubule dynamics. *Cell. Mol. Life Sci.* **0**, 0.
- Nejedla, M., Sadi, S., Sulimenko, V., de Almeida, F. N., Blom, H., Draber, P., Aspenstrom, P. and Karlsson, R.** (2016). Profilin connects actin assembly with microtubule dynamics. *Mol. Biol. Cell* **27**, 2381–2393.
- Ngo, K. X., Umeki, N., Kijima, S. T., Kodera, N., Ueno, H., Furutani-Umezu, N., Nakajima, J., Noguchi, T. Q. P., Nagasaki, A., Tokuraku, K., et al.** (2016). Allosteric regulation by cooperative conformational changes of actin filaments drives mutually exclusive binding with cofilin and myosin. *Sci. Rep.* **6**, 35449.
- Nishimura, Y., Applegate, K., Davidson, M. W., Danuser, G. and Waterman, C. M.** (2012). Automated screening of microtubule growth dynamics identifies MARK2 as a regulator of leading edge microtubules downstream of Rac1 in migrating cells. *PLoS One* **7**, e41413.
- Olmsted, J. B. and Borisy, G. G.** (1975). Ionic and nucleotide requirements for microtubule polymerization in vitro. *Biochemistry* **14**, 2996–3005.
- Pawlak, G. and Helfman, D. M.** (2001). Cytoskeletal changes in cell transformation and tumorigenesis. *Curr. Opin. Genet. Dev.* **11**, 41–47.
- Plastino, J. and Blanchoin, L.** (2019). Dynamic stability of the actin ecosystem. *J. Cell Sci.* **132**, jcs219832.
- Pollard, T. D. and Borisy, G. G.** (2003). Cellular motility driven by assembly and disassembly of actin filaments. *Cell* **112**, 453–465.
- Ponti, A., Machacek, M., Gupton, S. L., Waterman-Storer, C. M. and Danuser, G.** (2004). Two distinct actin networks drive the protrusion of migrating cells. *Science* **305**, 1782–6.
- Posern, G., Sotiropoulos, A. and Treisman, R.** (2002). Mutant actins demonstrate a role for unpolymerized actin in control of transcription by serum response factor. *Mol. Biol. Cell* **13**, 4167–78.

- Raftopoulou, M. and Hall, A.** (2004). Cell migration: Rho GTPases lead the way. *Dev. Biol.* **265**, 23–32.
- Rodriguez, O. C., Schaefer, A. W., Mandato, C. a, Forscher, P., Bement, W. M. and Waterman-Storer, C. M.** (2003). Conserved microtubule-actin interactions in cell movement and morphogenesis. *Nat. Cell Biol.* **5**, 599–609.
- Ronen, D. and Ravid, S.** (2009). Myosin II tailpiece determines its paracrystal structure, filament assembly properties, and cellular localization. *J. Biol. Chem.* **284**, 24948–24957.
- Rosenfeld, S. S., Xing, J., Chen, L. Q. and Sweeney, H. L.** (2003). Myosin IIB is unconventionally conventional. *J. Biol. Chem.* **278**, 27449–27455.
- Rösner, H., Möller, W., Wassermann, T., Mihatsch, J. and Blum, M.** (2007). Attenuation of actinomyosinII contractile activity in growth cones accelerates filopodia-guided and microtubule-based neurite elongation. *Brain Reserch* **1176**, 1–10.
- Rottner, K. and Schaks, M.** (2018). Assembling actin filaments for protrusion. *Curr. Opin. Cell Biol.* **56**, 53–63.
- Saitoh, T., Takemura, S., Ueda, K., Hosoya, H., Nagayama, M., Haga, H., Kawabata, K., Yamagishi, A. and Takahashi, M.** (2001). Differential localization of non-muscle myosin II isoforms and phosphorylated regulatory light chains in human MRC-5 fibroblasts. *FEBS Lett.* **509**, 365–369.
- Sandquist, J. C. and Means, A. R.** (2008). The C-terminal tail region of nonmuscle myosin II directs isoform-specific distribution in migrating cells. *Mol. Biol. Cell* **19**, 5156–67.
- Sato, M. K., Takahashi, M. and Yazawa, M.** (2007). Two regions of the tail are necessary for the isoform-specific functions of nonmuscle myosin IIB. *Mol. Biol. Cell* **18**, 1009–17.
- Sato, Y., Murakami, Y. and Takahashi, M.** (2017). Semi-retentive cytoskeletal fractionation (SERCYF): A novel method for the biochemical analysis of the organization of microtubule and actin cytoskeleton networks. *Biochem. Biophys. Res. Commun.* **488**, 614–620.
- Sellers, J. R.** (2000). Myosins: a diverse superfamily. *Biochim. Biophys. Acta* **1496**, 3–22.
- Shutova, M. S. and Svitkina, T. M.** (2018). Mammalian nonmuscle myosin II comes in three flavors. *Biochem. Biophys. Res. Commun.* 1–9.
- Shutova, M. S., Alexandrova, A. Y. and Vasiliev, J. M.** (2008). Regulation of polarity in cells devoid of actin bundle system after treatment with inhibitors of myosin II activity. *Cell Motil. Cytoskeleton* **65**, 734–46.
- Shutova, M. S., Asokan, S. B., Talwar, S., Assoian, R. K., Bear, J. E. and Svitkina, T. M.** (2017). Self-sorting of nonmuscle myosins IIA and IIB polarizes the cytoskeleton and modulates cell motility. *J. Cell Biol.* **216**, 2877–2889.
- Skruber, K., Read, T.-A. and Vitriol, E. A.** (2018). Reconsidering an active role for G-actin in cytoskeletal regulation. *J. Cell Sci.* **131**, jcs203760.

- Skube, S. B., Chaverri, J. M. and Goodson, H. V.** (2010). Effect of GFP tags on the localization of EB1 and EB1 fragments in vivo. *Cytoskeleton* **67**, 1–12.
- Söderberg, O., Gullberg, M., Jarvius, M., Ridderstråle, K., Leuchowius, K.-J., Jarvius, J., Wester, K., Hydbring, P., Bahram, F., Larsson, L.-G., et al.** (2006). Direct observation of individual endogenous protein complexes in situ by proximity ligation. *Nat. Methods* **3**, 995–1000.
- Song, Y. and Brady, S. T.** (2015). Post-translational modifications of tubulin: Pathways to functional diversity of microtubules. *Trends Cell Biol.* **25**, 125–136.
- Takashi, R. and Putnam, S.** (1979). A fluorimetric method for continuously assaying ATPase: Application to small specimens of glycerol-extracted muscle fibers. *Anal. Biochem.* **92**, 375–382.
- Thomas, D. G., Yenepalli, A., Denais, C. M., Rape, A., Beach, J. R., Wang, Y. li, Schiemann, W. P., Baskaran, H., Lammerding, J. and Egelhoff, T. T.** (2015). Non-muscle myosin IIB is critical for nuclear translocation during 3D invasion. *J. Cell Biol.* **210**, 583–594.
- Thurston, S. F., Kulacz, W. A., Shaikh, S., Lee, J. M. and Copeland, J. W.** (2012). The Ability to Induce Microtubule Acetylation Is a General Feature of Formin Proteins. *PLoS One* **7**,.
- Tian, Y., Tian, X., Gawlak, G., O'Donnell, J. J., Sacks, D. B. and Birukova, A. a** (2014). IQGAP1 regulates endothelial barrier function via EB1-cortactin cross talk. *Mol. Cell Biol.* **34**, 3546–58.
- Tian, X., Ohmura, T., Shah, A. S., Son, S., Tian, Y. and Birukova, A. A.** (2017). Role of End Binding Protein-1 in endothelial permeability response to barrier-disruptive and barrier-enhancing agonists. *Cell. Signal.* **29**, 1–11.
- Tokuraku, K., Kurogi, R., Toya, R. and Uyeda, T. Q. P.** (2009). Novel Mode of Cooperative Binding between Myosin and Mg<sup>2+</sup>-actin Filaments in the Presence of Low Concentrations of ATP. *J. Mol. Biol.* **386**, 149–162.
- Tsutsumi, M., Muto, H., Myoba, S., Kimoto, M., Kitamura, A., Kamiya, M., Kikukawa, T., Takiya, S., Demura, M., Kawano, K., et al.** (2016). In vivo fluorescence correlation spectroscopy analyses of FMBP-1, a silkworm transcription factor. *FEBS Open Bio* **6**, 106–125.
- Tullio, A. N., Accili, D., Ferrans, V. J., Yu, Z. X., Takeda, K., Grinberg, A., Westphal, H., Preston, Y. A. and Adelstein, R. S.** (1997). Nonmuscle myosin II-B is required for normal development of the mouse heart. *Proc. Natl. Acad. Sci. U. S. A.* **94**, 12407–12.
- Valencia, R. G., Walko, G., Janda, L., Novacek, J., Mihailovska, E., Reipert, S., Andrä-Marobela, K. and Wiche, G.** (2013). Intermediate filament-associated cytolinker plectin 1c destabilizes microtubules in keratinocytes. *Mol. Biol. Cell* **24**, 768–84.

- Verderame, M., Alcorta, D., Egnor, M., Smith, K. and Pollack, R.** (1980). Cytoskeletal F-actin patterns quantitated with fluorescein isothiocyanate-phalloidin in normal and transformed cells. *Proc. Natl. Acad. Sci.* **77**, 6624–6628.
- Vicente-Manzanares, M., Koach, M. A., Whitmore, L., Lamers, M. L. and Horwitz, A. F.** (2008). Segregation and activation of myosin IIB creates a rear in migrating cells. *J. Cell Biol.* **183**, 543–554.
- Vicente-Manzanares, M., Ma, X., Adelstein, R. S. and Horwitz, A. R.** (2009). Non-muscle myosin II takes centre stage in cell adhesion and migration. *Nat. Rev. Mol. Cell Biol.* **10**, 778–90.
- Vitriol, E. A., McMillen, L. M., Kapustina, M., Gomez, S. M., Vavylonis, D. and Zheng, J. Q.** (2015). Two functionally distinct sources of actin monomers supply the leading edge of lamellipodia. *Cell Rep.* **11**, 433–445.
- Walczak, C. E. and Shaw, S. L.** (2010). A MAP for bundling microtubules. *Cell* **142**, 364–367.
- Wang, F., Kovács, M., Hu, A., Limouze, J., Harvey, E. V. and Sellers, J. R.** (2003). Kinetic mechanism of non-muscle myosin IIB. Functional adaptations for tension generation and maintenance. *J. Biol. Chem.* **278**, 27439–27448.
- Wang, A., Ma, X., Conti, M. A., Liu, C., Kawamoto, S. and Adelstein, R. S.** (2010). Nonmuscle myosin II isoform and domain specificity during early mouse development. *Proc. Natl. Acad. Sci.* **107**, 14645–14650.
- Watanabe, S., Ando, Y., Yasuda, S., Hosoya, H., Watanabe, N., Ishizaki, T. and Narumiya, S.** (2008). mDia2 induces the actin scaffold for the contractile ring and stabilizes its position during cytokinesis in NIH 3T3 cells. *Mol. Biol. Cell* **19**, 2328–38.
- Waterman-Storer, C. M. and Salmon, E.** (1999). Positive feedback interactions between microtubule and actin dynamics during cell motility. *Curr. Opin. Cell Biol.* **11**, 61–67.
- Waterman-Storer, C. M., Worthylake, R. a, Liu, B. P., Burrridge, K. and Salmon, E. D.** (1999). Microtubule growth activates Rac1 to promote lamellipodial protrusion in fibroblasts. *Nat. Cell Biol.* **1**, 45–50.
- Wen, Y., Eng, C. H., Schmoranzler, J., Cabrera-Poch, N., Morris, E. J. S., Chen, M., Wallar, B. J., Alberts, A. S. and Gundersen, G. G.** (2004). EB1 and APC bind to mDia to stabilize microtubules downstream of Rho and promote cell migration. *Nat. Cell Biol.* **6**, 820–830.
- Wittmann, T., Bokoch, G. M. and Waterman-Storer, C. M.** (2003). Regulation of leading edge microtubule and actin dynamics downstream of Rac1. *J. Cell Biol.* **161**, 845–851.
- Wittmann, T., Bokoch, G. M. and Waterman-Storer, C. M.** (2004). Regulation of Microtubule Destabilizing Activity of Op18/Stathmin Downstream of Rac1. *J. Biol. Chem.* **279**, 6196–6203.

- Wu, X., Kodama, A. and Fuchs, E.** (2008). ACF7 Regulates Cytoskeletal-Focal Adhesion Dynamics and Migration and Has ATPase Activity. *Cell* **135**, 137–148.
- Yamada, K. M., Ohanian, S. H. and Pastan, I.** (1976). Cell surface protein decreases microvilli and ruffles on transformed mouse and chick cells. *Cell* **9**, 241–5.
- Yamashiro, S., Mizuno, H., Smith, M. B., Ryan, G. L., Kiuchi, T. and Blanchoin, L.** (2014). New single-molecule speckle microscopy reveals modification of the retrograde actin flow by focal adhesions at nanometer scales. *Mol. Biol. Cell* **7**, 1010–1024.
- Yamashiro, S., Tanaka, S., McMillen, L. M., Taniguchi, D., Vavylonis, D. and Watanabe, N.** (2018). Myosin-dependent actin stabilization as revealed by single-molecule imaging of actin turnover. *Mol. Biol. Cell* **29**, 1941–1947.
- Yamazaki, M., Furuike, S. and Ito, T.** (2002). Mechanical response of single filamin A (ABP-280) molecules and its role in the actin cytoskeleton. *J. Muscle Res. Cell Motil.* **23**, 525–34.
- Zuidsherwoude, M., Green, H. L. H., Thomas, S. G., Zuidsherwoude, M., Green, H. L. H., Thomas, S. G., Zuidsherwoude, M. and Thomas, S. G.** (2018). Formin proteins in megakaryocytes and platelets : regulation of actin and microtubule dynamics Formin proteins in megakaryocytes and platelets : regulation of actin and microtubule dynamics. *Platelets* **00**, 1–8.

## **Acknowledgement**

I express my gratitude to Professor Yota Murakami of Hokkaido University for his helpful advice, encouragement, suggestion and discussion.

I would like to express my deepest appreciation to Associate professor Masayuki Takahashi of Hokkaido University for his helpful advice, encouragement, suggestion and discussion.

I would like to thank Assistant professor Shinya Takahata of Hokkaido University for his enormous support and insightful comment.

I would like to express my gratitude to Adjunct associate professor Akiko Nakatomi of Hokkaido University for her enormous supports, insightful comment and strong encouragement.

I would like to express my gratitude to Professor Kazuyasu Sakaguchi of Hokkaido University for accepting the chairman of my doctoral dissertation.

I would like to express my gratitude to Professor Yasuyuki Fujita and Professor Mutsumi Takagi of Hokkaido University for accepting the vice-chairman of my doctoral dissertation.

I am very grateful to Professor Keiju Kamijo of Tohoku Medical and Pharmaceutical University for his helpful advice, suggestion, discussion, and for providing me a lot of experimental tools.

I am grateful to the Dr. Kentaro Kobayashi and Dr. Motosuke Tsutsumi of Hokkaido University Nikon Imaging Center for their assistance with microscopy, image acquisition, and analysis.

I would like to thank Dr. Masahiro Kuragano of Muroran Institute of Technology for his helpful discussion and technical guidance in some experiments.

I am thankful to all the members of Bioorganic Laboratory of Hokkaido University.

I would like to extend my indebtedness to my parents, my sister and my cats for their endless love, understanding, support and sacrifice throughout my study.

And, I would like to give my deepest thanks to my steady, Aoi Ohnuma, with superlative love, for her psychological support of my daily life and helpful discussion of my study. Please get closer to me in the future too.